Research on Responsivity Improvement of Single Crystal Diamond UV Photodetector

A dissertation submitted to
Tokushima University
in partial fulfillment of the requirements
for the degree of
Doctor of Philosophy

By
刘璋成
Supervisor: Prof. Jin-PingAo
Electrical and Electronic Engineering
September 2019

ABSTRACT

Ultraviolet detection technology is a high-tech technology, which has great application prospects in environmental monitoring, information technology, medical treatment, astronomical observation and satellite communication. As a wide band gap semiconductor, diamond has excellent properties such as high carrier mobility, high saturated carrier drift rate, high thermal conductivity, low dielectric constant, high chemical stability and radiation resistance. It is an ideal material for fabricating ultraviolet detectors. In this dissertation, a series of studies have been carried out to improve the responsivity of single crystal diamond ultraviolet detectors.

Ultraviolet detectors with photocurrent gain were fabricated by the single crystal diamond intrinsic epitaxial layer with NV color center defect. The origin for the photoelectric gain is the electron injection, whose opening voltage decreases with the increase of the number of photo-generated electrons. When the bias voltage is greater than the open voltage, the photocurrent increases rapidly, and the responsivity of the detector increases rapidly from 4.29 mA/W at 3 V to 51 mA/W at 12 V. In the deep ultraviolet band, avalanche effect was observed as the voltage increased further. The photocurrent increased 10 times rapidly, and the responsivity at 50 V was as high as 1.18 A/W.

The diamond groove three-dimensional structure detector was fabricated by bottom-up method. Firstly, the selective epitaxial process is optimized. The metal mask needs high melting point and stability, and the annealing and cooling processes are needed to maintain the integrity of the electrode. On this basis, the diamond groove three-dimensional structure photoconductive detectors and photovoltaic detectors were investigated. Photoconductive detectors have high responsivity, but the dark current is high and the response speed is slow. Photovoltaic detectors have low responsivity, but their dark current is five orders lower than that of photoconductive detectors, and the response speed is fast.

Diamond strip arrays were etched on the surface by optimized ICP etching process, and quasi-one-dimensional diamond ultraviolet detectors were obtained with the interdigitated electrodes set perpendicular to the direction of the diamond strip. Because of the etching defects, the as-fabricated detectors have better performance than planar detectors only when the electrode spacing is large, and the photocurrent of the detectors is increased by 14.6%. After a second growth process, the surface defects were recovered, then the performance of quasi-one-dimensional structure detectors is better than that of planar structure detectors at any electrode space. The photocurrent and responsivity of quasi-one-dimensional structure detectors are increased by 106%, and the UV/visible light rejection ratio and transient response performance are improved.

The spectrum response range of diamond detector is extended by using TiO_2. TiO_2 thin film was deposited directly on diamond epitaxial layer by magnetron sputtering technology, and interdigitated structure detector was fabricated. The spectral response curves of the

detector show response peaks at 290 and 225 nm, which are derived from the ultraviolet response of TiO_2 and diamond respectively. By combining the two materials, the responsivity of the detector in the whole ultraviolet band is improved.

In the investigation of diamond p-i-n photodiode, the n-type doping process of diamond was studied firstly. The results show that the phosphorus doping concentration increases with the increase of growth temperature and the decrease of methane concentration. The growth rate of phosphorus-doped diamond films is over 20 m/h and the doping concentration is 1018 cm-3 by high temperature and high methane concentration process. Diamond p-i-n photodiodes have been fabricated based on this process, which have obvious photoelectric response. At 5 V, the responsivity at 215 nm is 730 A/W, and the UV/visible light suppression ratio of 215 nm/400 nm is 1.4×10^3. However, the acceptor concentration is high, which leads to a large dark current and a slow response speed.

CONTENTS

1 Introduction

1.1 Mechanism of UV photodetector

In the spectral range, ultraviolet (UV) light can be divided into four regions [1-3]: UV-A (wavelength 400-320 nm), UV-B (wavelength 320-280 nm), UV-C (wavelength 280-200 nm) and far-ultraviolet (wavelength 200-10 nm). UV photodetectors are devices that respond to these wavelengths, and their applications are very wide, attracting more and more research interest. The working mechanism of UV photodetectors are mainly based on photoelectric effect, which can be divided into external photoelectric effect and internal photoelectric effect [2]. The so-called external photoelectric effect, i.e. photoelectric emission effect, refers to that when photons irradiate metal or semiconductor, they can make the electrons escape from the material surface. This requires that the energy of photons is greater than the surface barrier. Internal photoelectric effect can be divided into photoconductive effect and photovoltaic effect. Photoconductive effect is related to conductivity change after light signal introduced. When the incident photon energy is larger than the bandgap of the material, the electrons in the valence band can be excited to the conduction band. As a result, the holes in the valence band and electrons in the conduction band lead to a conductivity enhancement. Photovoltaic effect is related to built-in potential change after light signal introduced. For inhomogeneous semiconductor or metal-semiconductor contact, the built-in potential will be formed at the interface, resulting a depletion layer. When light illuminates this area, an electron-hole pair will be generated in the depletion layer, swept to both sides by the built-in electric field, which reduces the built-in potential. The reduction is the photovoltaic potential difference, which is called photovoltaic effect.

The performance of a photodetector is characterized by various parameters, mainly including quantum efficiency, responsivity, sensitivity, spectral response, noise equivalent power, detectivity and transient response. The responsivity and sensitivity represent the relationship between the output of the detector and the light power. The responsivity is the ratio of the output voltage to the light power, while the sensitivity is the ratio of the output current to the light power. Light power is related to photon energy, that is, to the wavelength of light. As a detector, the responsivity and sensitivity are determined for the determined wavelength of light. When the response and sensitivity of the detector are plotted as a curve

with the change of wavelength, it is the spectral response. The performance of the detector can be clearly seen from the curve. Generally speaking, the detector has a cut-off wavelength. When the incident wavelength is longer than the cut-off wavelength, the photodetector shows little photo response, and the spectral response curve will be very low. When the incident wavelength is shorter than the cut-off wavelength,the photodetector shows large photo response, and the spectral response curve will rise rapidly. The spectral response curve also shows the rejection ratio, that is, the ratio of the responsivity of the effective detection range to that of the invalid detection range. Detectability is the reciprocal of the noise equivalent power NEP. Normalized Detectability D* is generally used to characterize the performance of the detector. D* is a function of wavelength and is also related to the modulation frequency.

In addition to the above parameter evaluation, ultraviolet detectors also need their unique performance, often including dark current, working temperature, response time and so on. An excellent ultraviolet detector needs to meet five requirements: high signal-to-noise ratio, high stability, high sensitivity, high response speed and high spectral selectivity. This is what is often called 5S requirement [4].

1.2 UV photodetector based on wide bandgap semiconductors

At present, most of the UV detectors are silicon materials. Even if they are insensitive in the UV region, they can be enhanced by special treatment to meet the needs. However, compared with UV-enhanced silicon photodetectors, in order to achieve better UV detection, in recent years, many detectors with wide bandgap semiconductor materials have been studied. The reason for choosing wide bandgap is that semiconductor with wide bandgap can be insensitive to visible light and act as a natural filter without using expensive filters. Moreover, these semiconductor materials have many excellent properties. This includes SiC, GaN, ZnO, Ga_2O_3, diamond and so on.

(1) Group III Nitride Semiconductor Photodetector

Group III nitrides [1] include AlN, GaN, InN and their ternary and quaternary compounds. These semiconductor materials have wide band gap, ideal spectral selectivity, good thermal stability, strong breakdown field, radiation resistance, and are expected to make devices with high responsivity. In the 1990s, Khan *et al.* [5] prepared epitaxial GaN thin films by metal organic chemical vapor deposition and fabricated the first GaN ultraviolet photodetector. This is a great breakthrough. Subsequently, various research groups have developed a variety

of photodetector structures, such as photoconductor, MSM, Schottky junction, MIS, p-n junction and p-i-n structure [6-11]. The band gap of GaN [1] is 3.42 eV, corresponding to the cut-off wavelength of 360 nm. The band gap of InN is 0.65 eV, corresponding to the cut-off wavelength of 1770 nm. The band gap of AlN is 6.2 eV, corresponding to the cut-off wavelength of 210 nm [12]. Thus, adjusting the composition of In in $In_xGa_{1-x}N$ and Al in AlGaN can adjust the spectral range of coverage. Both light blindness and solar blindness, from visible light to near infrared, are involved.

(2) SiC photodetector

The band gap of SiC [13] can be changed from 2.0 eV to 7.0 eV. It can be used in high temperature, high frequency, high power and radiation environment. The development of SiC ultraviolet detectors came from the advent of commercial 6H-SiC (band gap is 3.0 eV, corresponding to the cut-off wavelength of 414 nm) and 4H-SiC (band gap is 3.23 eV, corresponding to the cut-off wavelength of 385 nm). SiC achieves p-type and n-type by doping Al and N, and realizes different device structures. Anklin *et al.* [14] manufactured n-type SiC Schottky junctions with high quality. Leakage current was less than 100 pA under bias voltage from -100 to -170V, and responsivity was 150 mA/W under 215 nm light. W.F. Yang *et al.* [15] manufactured a MSM-type SiC Photodetector based on 4H-SiC. The photodetector uses interdigital electrodes with the same spacing and electrode width. The dark current at 5V bias is only 0.25 pA, and the responsivity at 20V is 0.103A/W. At the same time, the UV/visible light rejection ratio is higher than 10^3. The p-i-n photodetector manufactured by SiC can achieve low noise and high response speed. The p-i-n [16] ultraviolet detector of 6H-SiC has very low dark current under bias, and its responsivity under 270 nm illumination is 150-175 mA/W. The responsivity of 4H-SiC p-n [17] junction ultraviolet detector under 280 nm light is 0.03A/W, and the photocurrent is four orders of magnitude higher than the dark current. X. Bai *et al.* [18] fabricated a p-i-n avalanche photodiode based on 4H-SiC with dark current density of 63 nA/cm^2 and quantum efficiency of about 40%. It can reduce the dark current to 90 pA and the optical gain to 1000 through reasonable design and optimization. After that, many people tried to improve the performance of SiC avalanche photodiode devices, and achieved good results.

(3) One-dimensional nanostructured ultraviolet detectors

In recent years, many ultraviolet detectors with one-dimensional or quasi-one-dimensional nanostructures [19-21] have been developed. Because they are one-dimensional nanostructures, many of their physical and chemical properties are different from those of

μm detectors. Its surface volume ratio is very large, its dimension is small, and it has high sensitivity to light. It is very suitable for making photoconductors. One-dimensional materials include ZnO, GaN and other metal oxides. H. Kind [22] and others have fabricated one-dimensional nanowire ultraviolet detectors based on zinc oxide. The diameter of these detectors ranges from 50 to 300 nm, and the resistivity is 3.5 MΩ·cm in dark. Under 380 nm ultraviolet irradiation, the resistivity decreases by 4 to 6 orders of magnitude, and the response time is less than 1 s. Some people also annealed the device so that the responsivity can reach 1.55 A/W at 10V. Son *et al*. [23] fabricated a single GaN nano-p-n junction, which can rectify in dark conditions. Under 365 nm UV irradiation and -0.03 V bias, the light response switch ratio is 14. GaN-based p-i-n nanowire photoblind detectors have also been developed, with a responsivity of 0.14 A/W at -1V and a UV/visible light rejection ratio of more than 100. Some metal oxide nanowire photodetectors also have considerable potential, including nanostructured ultraviolet photodetectors such as Ga_2O_3, SnO_2, In_2O_3, ZnGeO and $In_2Ge_2O_7$ [24-28]. They are special in nature and widely used.

1.3 State of art of diamond UV photodetector

Among many wide bandgap materials, diamond is a kind of material with many excellent properties: large band gap, the highest thermal conductivity, low dielectric constant, minimal atomic number, large resistivity, high radiation resistance and thermal stability, as shown in Table 1-1. These excellent qualities enable the devices to work safely and steadily in high temperature, high frequency, high power, strong radiation and other environments. Diamond detectors can be used in sewage treatment, smoke monitoring, micro-lithography, excimer laser beam monitoring, astronomical observation, biomedical analysis, high-energy particle detection and so on. Therefore, it is of great significance to study diamond UV detectors.

Table 1-1 Comparison of Properties of Natural Diamond and CVD Diamond Films

Properties	Natural diamond	CVD diamond
Thermal conductivity/$W\cdot cm^{-1}\cdot K^{-1}$	20	4-17 (10-200 μm)
Bandgap/eV	5.5	5.5
Resistivity/Ω·cm	$>10^{16}$	$>10^{10}$
Breakdown field/V/cm	10^7	10^5-10^6

Electron mobility/$cm^2/V·s$	1800	—
Hole mobility /$cm^2/V·s$	2200	—
Dielectric constant	5.6	5.6
Thermal stability/Celsius	1600	>1300

The rapid development of diamond UV photodetectors benefits from the development of CVD diamond film growth technology. So far, many researchers have been working hard to get high performance diamond photodetectors. The research of diamond photodetectors is focused on the growth condition modification, film quality, surface treatment, and electrode configuration optimization. In order to grow high quality diamond film materials, many methods have been developed. At present, there are seven growth methods for CVD diamond films, namely HFCVD, MW-PCVD, RF-PCVD, DC-PCVD, ECR-MWCVD, CFA-CVD and LA-CVD. The most common are HFCVD and MW-PCVD. Generally speaking, the diamond films grown by MPCVD method are of good quality and can be well adjusted. The performance of the detector is largely determined by the quality of the material. Impurities and defects exist in CVD diamond films, which affect the grain boundary, grain size and grain orientation of polycrystalline CVD diamond films. The quality of single crystal diamond is better than that of polycrystalline diamond. After CVD diamond growth is completed, there will be non-diamond phase or some other defects and impurities on the surface, and there will also be hydrogen terminals. Different surface treatment processes and methods will also affect the performance of devices.

Most of the diamond detectors do not need p-n junction structure, so the collection of photogenerated electron hole pairs is mainly accomplished by electrodes. According to different metal contacts, the structure of the device is different, and the performance parameters will also change. The influence of hydrogen and oxygen terminals on the electrode mode is also crucial. Since the study of diamond detectors, a variety of structures have been developed. Traditionally, there are interdigital structure, interdigital offset structure, PN junction structure, Schottky diode structure and MDV structure, etc. [29-33]. Generally, these structures use two kinds of effects: photoconductivity and photovoltaic effect. With the deepening of research, some new detection structures have been proposed, such as coplanar grid structure, graphene-diamond-metal sandwich structure, graphite

columnar electrode structure and stack electrode structure.

(1) Planar MSM structure

S. Salvatori *et al*. [34] used a planar MSM structure to study the effect of electrode spacing on device performance, as shown in Fig. 1-1. The results show that the dark current is less than 1 nA when the electrode spacing is 100 μm, and the external quantum output is more than 10% when the electrode spacing is 300 μm and the selectivity is close to 10^4 at 220 nm. At the same time, they pointed out that the use of interdigital electrodes can increase the detection area, because in this structure, the effective light detection area is limited to the gap between the electrodes, which is very small compared with the electrodes, and is also a waste for diamond sheets.

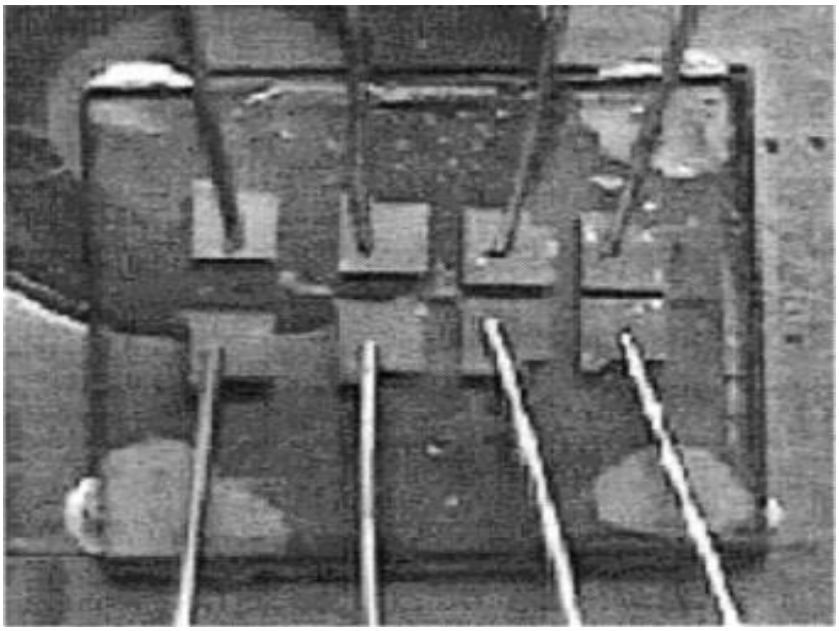

Figure 1-1 Planar MSM Electrode detectors [34].

(2) Interdigital structure

Robert D. McKeag *et al*. [35] used interdigital electrodes to fabricate photodetectors, whose structure is shown in Figure 1-2. The diamond film has a grain size of 20-30 μm, and the electrode spacing and width are both 20 μm. The space between electrodes is equal to the grain size, and the number of grain boundaries crossed by electron-hole pairs can be reduced as much as possible. The use of interdigital structure can increase the detection area and reduce the transport time of electron-hole pairs, which is conducive to the improvement of detection efficiency. The dark current they measured was less than 0.1 nA, and the responsivity at 200 nm was 10^6 times higher than that at visible wavelength.

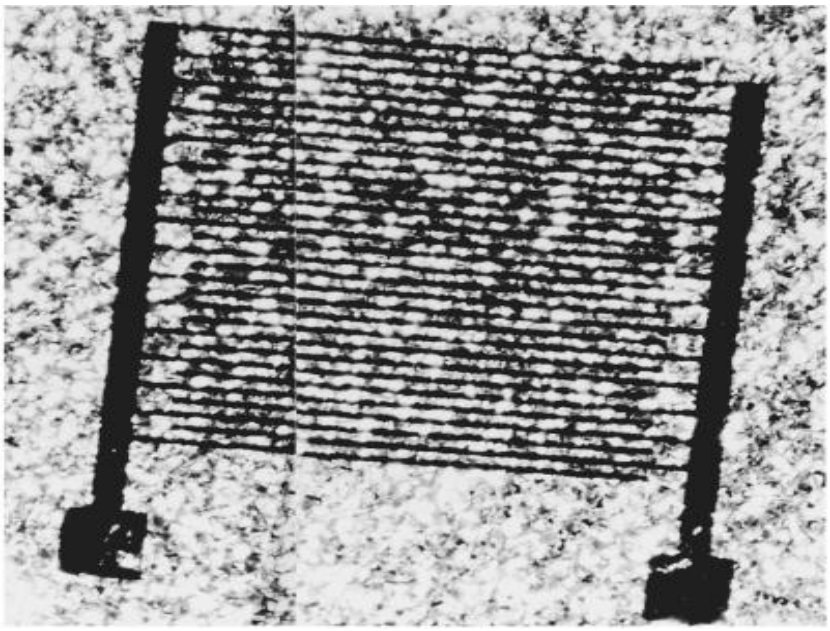

Figure 1-2 Interdigitated electrode detector [35].

(3) Graphene-diamond-metal sandwich structure

Kaiyuan Yao *et al*. [36] studied the sandwich structure with graphene performing as top electrode, as shown in Figure 1-3. Graphene electrode has its unique advantages because it can transmit 98% UV light. Additionally, it can form a sandwich structure, which can form a uniform electric field. Under 5 V bias and 220 nm wavelength, the response is 0.13A/W and the quantum efficiency is 72%.

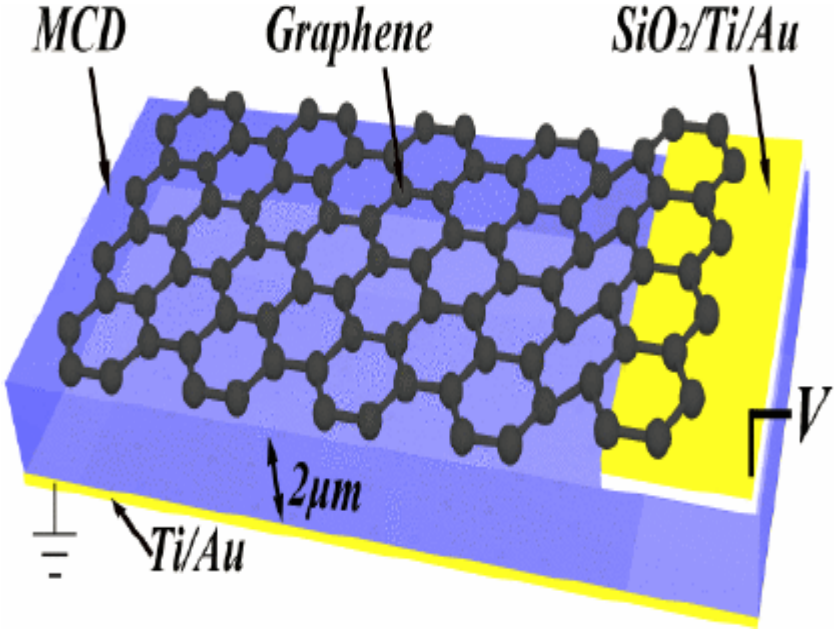

Figure 1-3 Graphene-Diamond-Metal Structural Diagram [36].

(4) Stack electrode detector

Y. lwakaji *et al*. [37] used stack electrodes structure to fabricate high quality single crystal diamond UV photodetectors. The substrate is HPHT method synthesized Ib-type diamond. Then buffer layer, boron-doped layer, and undoped layer are sequentially grown on the substrate through MPCVD method. Next, the stack structure is etched by electron cyclotron resonance oxygen plasma etching method. The width of diamond strip is 10 μm and the spacing is 5 μm. TiN electrodes are fabricated by lift-off method and DC magnetron sputtering method to form ohmic contact. When the voltage is close to 100V, the dark current is still less than 10pA. The ratio of responsivity at 210 nm to that at 240 nm is higher than 10^4, and the response time is 1.2 ms.

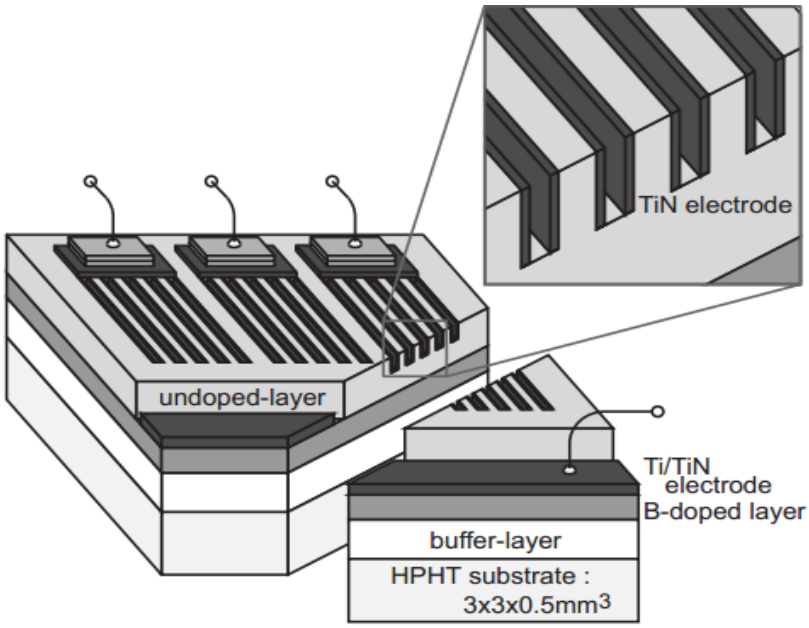

Figure 1-6 Stack electrode detector [37].

1.4 Facing challenges

Since the research of CVD diamond film UV photodetector, great progress has been made, but its real application is still far. If a thing has no use value, it will disappear soon. In order to make the diamond UV photodetector practical, it is necessary to make the device process as mature as the silicon detector, make the device performance more stable, practical and effective, and most importantly, reduce the cost. This is not only related to the quality of materials, but also to the rapid growth of materials. How to rapidly grow high quality diamond film, how to determine the most effective detector structure and how to find the best application conditions of the detector are all important challenges for the development of diamond detectors.

2 Diamond UV Photodetector with Photocurrent Gain

2.1 Introduction

As a good UV photodetector, it should have high ultraviolet/visible selectivity, high signal-to-noise ratio, high response speed, high stability and high sensitivity of 5S performance. Among many broadband gap semiconductors, diamond is a promising material for deep ultraviolet photoelectric detection due to its wide band gap (5.5 eV), high carrier mobility (3800 cm^2/Vs), high thermal conductivity (22 W/cmK), low dielectric constant (about 5.7), high chemical stability and high radiation resistance. The research of diamond ultraviolet photodetectors mainly focuses on film quality and device design [38]. So far, several device structures have been proposed, such as p-i-n detector [39], Schottky photodiode and metal-semiconductor-metal (MSM) detector. In these devices, MSM structure has been widely used because of its simple manufacturing process. MSM structure can be divided into two types: MSM photoconductive detector and MSM photodiode [40]. Compared with MSM photoconductive detectors, MSM photodiodes do not need annealing. The Schottky barrier formed at the metal/diamond interface can reduce the dark current and noise level [35]. Teraji *et al*. used Ti/Au interdigital electrodes to fabricate back-to-back Schottky photodetectors on undoped single crystal diamond epitaxial layers. Although Ti in undoped diamond is Schottky contact [41], in his work, the photocurrent increases linearly with bias voltage. Liao *et al*. also fabricated metal-diamond-metal photodetectors on undoped diamond epitaxy layer, whose electrode material is tungsten carbide. Although his structure is back-to-back Schottky structure, its photocurrent curve is non-linear, and shows different IV characteristics in multiple voltage ranges [42]. At low bias, IV curve shows sublinear behavior, while at high bias, I-V curve shows superlinear behavior. The reason for producing superlinear behavior IV curve lies in photocurrent gain. Liao *et al*. attributed the source of photocurrent gain to the formation of interface traps between WC and diamond. However, another back-to-back Schottky detector prepared by Liao *et al*. did not show such photocurrent gain [40] with the same electrode configuration. Therefore, the mechanism of photocurrent gain should be further explored.

In this chapter, we try to fabricate Ti/Au electrodes on the surface of undoped

oxygen-terminated diamond to form back-to-back Schottky structure photodetectors, and study the photocurrent gain. The results show that the device has photocurrent gain, and the photocurrent gain is related to the photoelectron density. The avalanche effect was observed for the first time at high voltage.

2.2 Experimental

(1) Substrate preparation

The substrate was high temperature and high pressure (HPHT) IIa-type (100)-orineted diamond, which was heated at 250 ℃ for 2 hours in a mixture of sulfuric acid and nitric acid solution to remove inorganic impurities and graphite phase on the surface. Then it was ultrasonic cleaned in deionized water, alcohol, acetone, alcohol and deionized water for 5 minutes in turn to remove surface acid pickling residues and organic impurities.

(2) Epitaxy growth

A high quality single crystal diamond epitaxial layer was grown on the substrate through MPCVD method. Figure 2-1 shows the picture of the AX5200 MPCVD system used for diamond growth. The parameters of epitaxy growth are: CH_4/H_2=1%, gas flow rate 500 sccm, substrate temperature 900 ℃, pressure 13 kPa, power 1 kW, and epitaxy thickness 200 nm. After growth, the diamond sample was heated for 1 hour in a 1:1 volume ratio mixture of sulfuric acid and nitric acid at 250 ℃ to change hydrogen termination into oxygen termination.

Figure 2-1 Picture of the AX5200 MPCVD system used for diamond growth.

(3) Electrode fabrication

The interdigitated electrode pattern was formed on the epitaxial layer surface by

photolithography, and then the sample was placed into the magnetron sputtering cavity. Ti/Au thin films with thickness of 30 nm/120 nm were sputtered on the surface of the sample. The parameters of magnetron sputtering are: argon flow rate 40 sccm, pressure 0.3 Pa, radio frequency power 75 W. Finally, the photoresist and the metal on it were removed by lift-off process, and the planar interdigitated electrode structure detector was obtained. Its interdigitated electrode has a width of 10 μm, a space of 10 μm and a photosensitive area of 0.36 mm^2. Figure 2-2 shows the picture of photolithography machine.

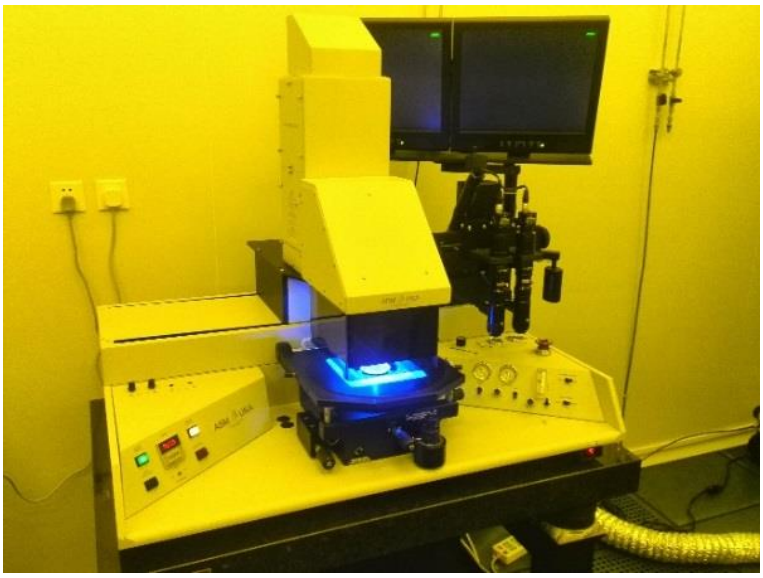

Figure 2-2 Picture of photolithography machine.

(4) Characterization of properties

The quality of the diamond substrate was evaluated by a Raman spectrometer with a 50× objective lens and 532-nm wavelength laser. The electrical and photoresponse properties of the photodetector were evaluated by an Agilent B1505A power device analyzer, 1000-W Xe lamp source, and monochromator. The incident light power was measured by a commercial UV-enhanced Si detector. Time response behaviors were measured by repeatedly switching the UV light on and off with a metal shutter.

2.3 Results and discussion

Raman spectrum is a conventional method to characterize the diamond phase. Figure 2-3(a) shows the picture of Raman machine used in our lab. When a light beam interacts with a molecule as the scattering center, the vibration of the molecule will change the propagation direction and frequency of a small number of photons. This phenomenon is called Raman scattering. The interaction between photons and sample molecules can be

analyzed from the transition between energy levels, as shown in Figure 2-3(b). E_0 is the ground state of electrons, E_1 is the vibrational excited state, $E_0+h\nu_0$ and $E_1+h\nu_0$ are the excited states.

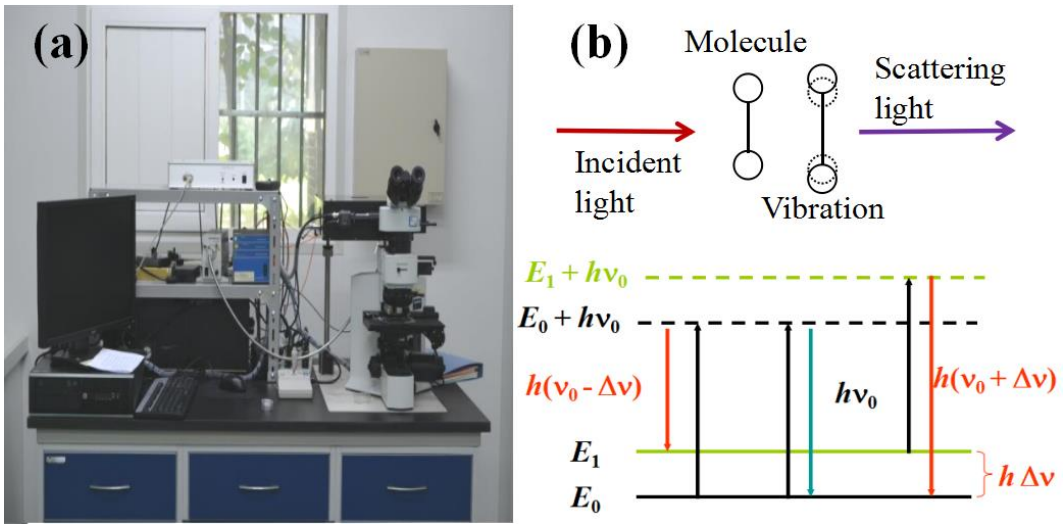

Figure 2-3 (a) Picture of Raman machine; (b) Schematic of Raman principle.

When the sample molecule is in the ground state, and the energy of incident photons is much larger than the energy required for the transition of vibration level but not enough to excite the molecule to the excited state of electron level, the sample molecule absorbs photons and reaches a quasi-excited state, also known as virtual energy state, namely $E_0+h\nu_0$ and $E_1+h\nu_0$. The sample molecule is unstable in the quasi-excited state, and it will return to the ground state of the electron level. If the molecule returns to the vibrational level ground state E_0 in the electron level ground state, the energy of photons does not change and Rayleigh scattering occurs. If the sample molecule returns to the higher vibrational level in the ground state of the electron level, i.e. some vibrational excited states such as E_1, the scattered photon energy is $h(\nu_0-\Delta\nu)$, less than the incident photon energy $h\nu_0$, and its wavelength is larger than the incident light. At this time, a Raman scattering line, called Stokes line, will appear on the lower frequency side of the Rayleigh scattering line of the scattering spectrum. If the sample molecule is not in the lowest vibrational level of the ground state of the electron energy level at the moment before the interaction with the incident photon, but in the excited state of some vibrational level in the ground state of the electron energy level, such as E_1, then the incident photon makes it transit to the quasi-excited state $E_1+h\nu_0$, and the molecule falls back to the ground state E_0 of the ground state of the electron energy level, so that the scattered light energy $h(\nu_0+\Delta\nu)$ is larger than that of the ground state E_0. The radiation photon energy h0, whose spectral line is located at

the high frequency side of Rayleigh spectral line, is called anti-Stokes line. In Raman test, the data obtained are Raman displacement. Raman displacement is the difference between the frequency of Raman scattering light and incident light, reflecting the specific sample information. For diamond, its characteristic Raman displacement is 1332 cm^{-1}. Therefore, the presence of diamond characteristic peaks can be observed by Raman spectroscopy to determine whether the films contain diamond phase.

Figure 2-4 shows the Raman spectrum of diamond epitaxial layer. It can be observed that there is a sharp Raman peak at about 1333 cm^{-1} with a half-peak width of 3.96 cm^{-1}. The Raman characteristic peak of diamond indicates that the sample is diamond, and its smaller half-peak width indicates that the quality of single crystal diamond is acceptable [37]. In addition, another peak can be observed at about 1428 cm^{-1}. The peak value is weak and the range is wide. It corresponds to the wavelength of 575 nm in the photoluminescence spectrum. The laser emission spectra of diamond epitaxy layer are given in the illustration. The peak at 572 nm is diamond peak, and the peak at 575 nm is NV^0 color center fluorescence peak. Both peaks correspond to Raman spectra. There is also a peak at 637 nm in the illustration, which comes from the NV-center [43]. Therefore, the results show that there are some nitrogen impurities in the diamond epitaxial layer.

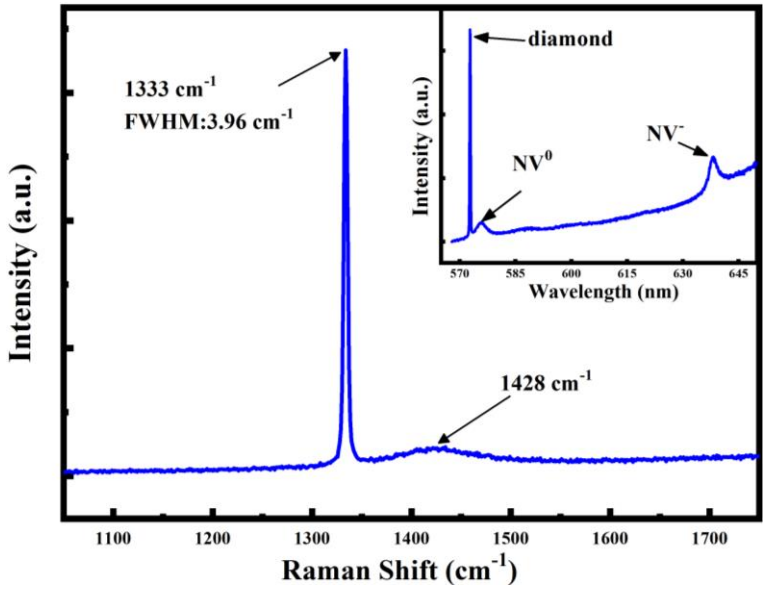

Figure 2-4 Raman spectrum of diamond epitaxial layer.

XPS technology can be used to directly measure the barrier height of metal/diamond contact. By measuring the C1s peak of diamond covered by titanium/diamond interdigital electrodes and comparing with the standard C1s spectrum of diamond, the energy band offset can be obtained. In addition, reference samples need to be prepared to calibrate the

results. Generally speaking, reference samples select gold. The barrier height (Φ_{bh}) of Ti/diamond contact can be calculated by the following equation [44]:

$$\phi_{BH} = E_{C1s} - \Delta E_{diamond} - (E_{metal\_core}^{Au\_diamond} - E_{metal\_core}^{Au\_reference}) \quad (2\text{-}1)$$

where E_{C1s} is the binding energy of C 1s peak of diamond in the area covered by Ti/Au interdigitated electrodes, $\Delta E_{diamond}$ is the energy difference between C1s and the maximum value of valence band for undoped oxygen-terminated diamond, $E_{metal\_core}^{Au\_diamond}$ is $Au4f_{7/2}$ binding energy on diamond and $E_{metal\_core}^{Au\_reference}$ is $Au4f_{7/2}$ binding energy of reference sample. Generally, $\Delta E_{diamond}$ is about 283.9 eV [45].

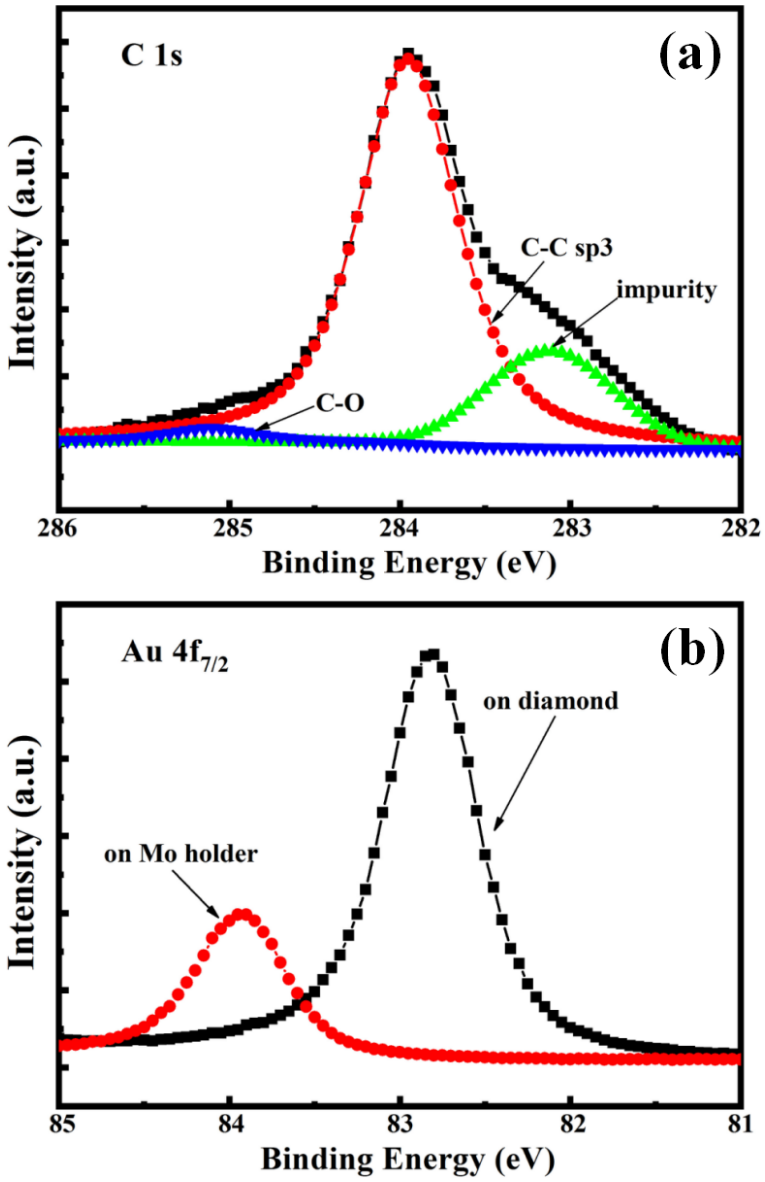

Figure 2-5 XPS spectra of (a) C1s and (b) Au4f7/2.

Figure 2-5 (a) shows the XPS spectrum of C1s obtained from the diamond surface covered

by Ti/Au interdigitated electrodes. Among them, the peak of binding energy 283.95 eV is the characteristic peak of SP^3 C-C bond, the peak of binding energy 283.1 eV is related to carbide impurities, and the peak of binding energy 285.1 eV is the characteristic peak of C-O bond for oxygen-terminated diamond. Figure 2-5 (b) shows the Au4f7/2 XPS spectra of Ti/Au electrodes and reference sample with binding energies of 82.8 eV and 83.9 eV, respectively. Therefore, the barrier height of Ti/diamond contact can be calculated to be Φ_{bh}=283.95 eV-283.9 eV-(82.8-83.9) eV=1.15 eV. This value is larger than the typical ohmic contact value of 0.63 eV between Ti and p-type diamond [9]. Therefore, the Ti/diamond contact prepared in this experiment is Schottky contact.

Figure 2-6 shows IV characteristics of the UV photodetector under dark and 210 nm illumination conditions. Due to the existence of double Schottky junction, the dark current of the detector is very low with a value less than 300 fA at 30 V. Under the irradiation of 210 nm, the current of the device increases much. It should be noted that the photoelectric current of the detector can be divided into three parts. When the bias voltage is less than 5V, the photocurrent curve increases sublinearly. In the range of 5-9 V, the photocurrent increases exponentially. In the range of voltage greater than 9V, the current increases sublinearly again. Due to the exponential increase process, the photocurrent in the high voltage region is 10 times higher than that in the low voltage region. This phenomenon means that the UV photodetector produces photocurrent gain. The source of photocurrent gain can be attributed to the interface electron injection [46].

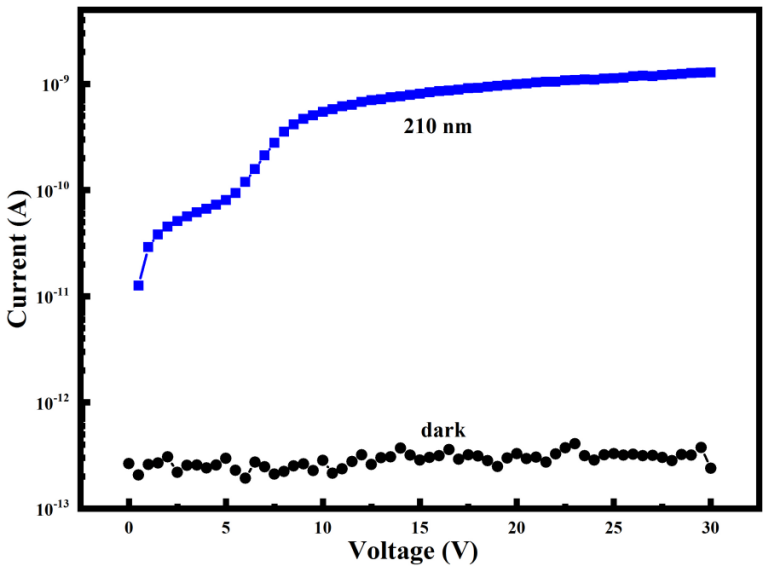

Figure 2-6 IV characteristics of the photodetector under dark and 210 nm illumination conditions

The injection process can be explained through band diagram. Figure 2-7 shows the energy band diagram of the back-to-back Schottky structure detector. Because the electrode structure is symmetrical, the energy band diagram in equilibrium state is symmetrical (V = 0). When a positive bias is applied, the band will bend upward from the positive to the negative. For the hole, there is only one barrier in the valence band, that is, the interface between the positive electrode and the diamond, so it is easy to be collected by the negative electrode. However, for electrons, there are two barriers in the conduction band, one at the positive/diamond interface and the other at the negative/diamond interface, which inhibit the transmission of electrons. Under the illumination below the cut-off wavelength of diamond, the electrons in the valence band will be stimulated to the conduction band, leaving a hole in the valence band. The holes generated by these light will be quickly collected by negative electrodes and generate primary photocurrent at low bias voltage, while the electrons stimulated by light will accumulate near the positive electrode/diamond interface. When the bias voltage increases, the large electric field will make these electrons pass through the barrier and be collected by the positive electrode, thus obtaining the photocurrent gain. This mechanism is different from Liao's gain mechanism [69], so IV characteristics are different.

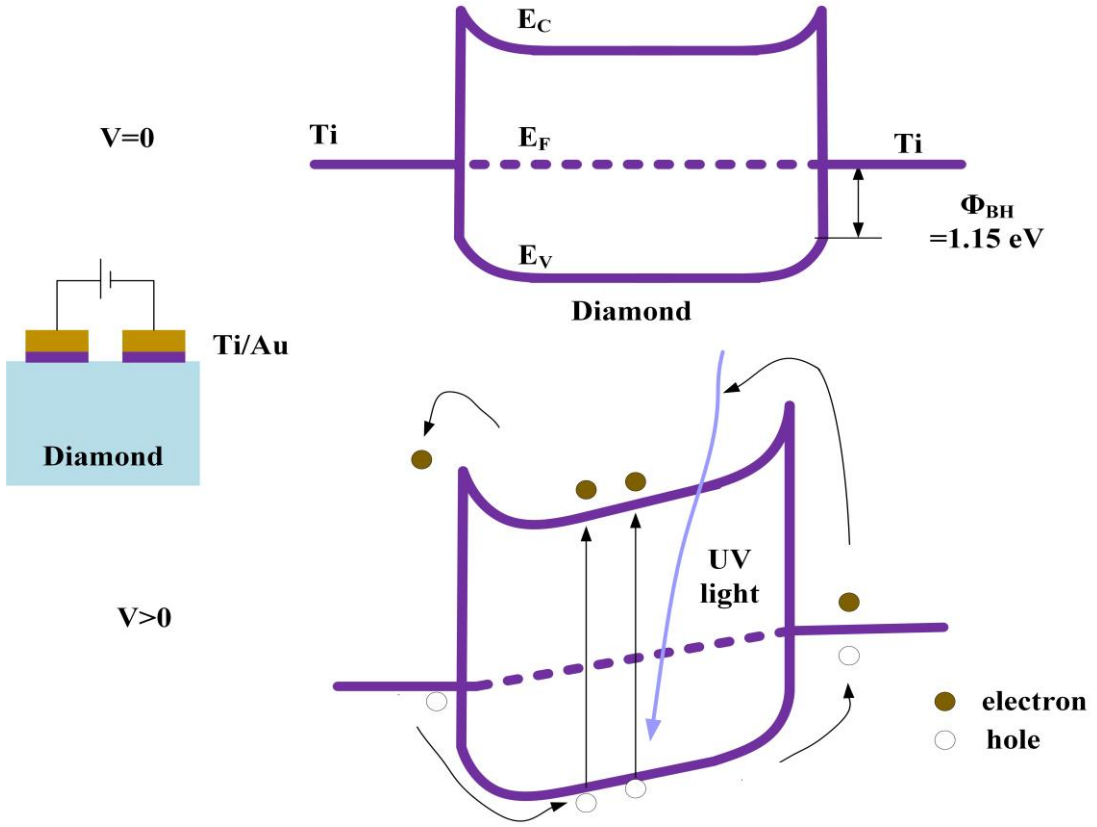

Figure 2-7 Energy band diagram of the back-to-back Schottky structure photoetector.

Figure 2-8 shows the IV characteristics of the photodetector at different light wavelengths. When the light wavelength is less than 240 nm, the current exponential gain region can be clearly observed. In addition, a slight exponential gain region can be observed at 400 and 450 nm. However, there are differences in the voltage at which they start to generate current exponential gains (denoted as the open voltage). It can be observed that the open voltage is smaller when illuminated with shorter-wavelength light.

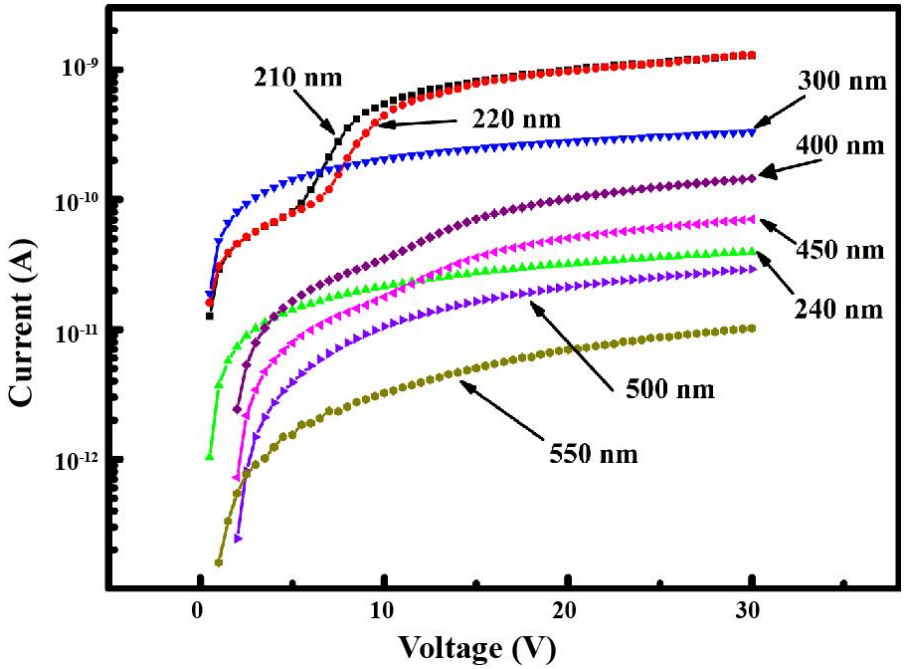

Figure 2-8 IV characteristics of the photodetector at different light wavelengths.

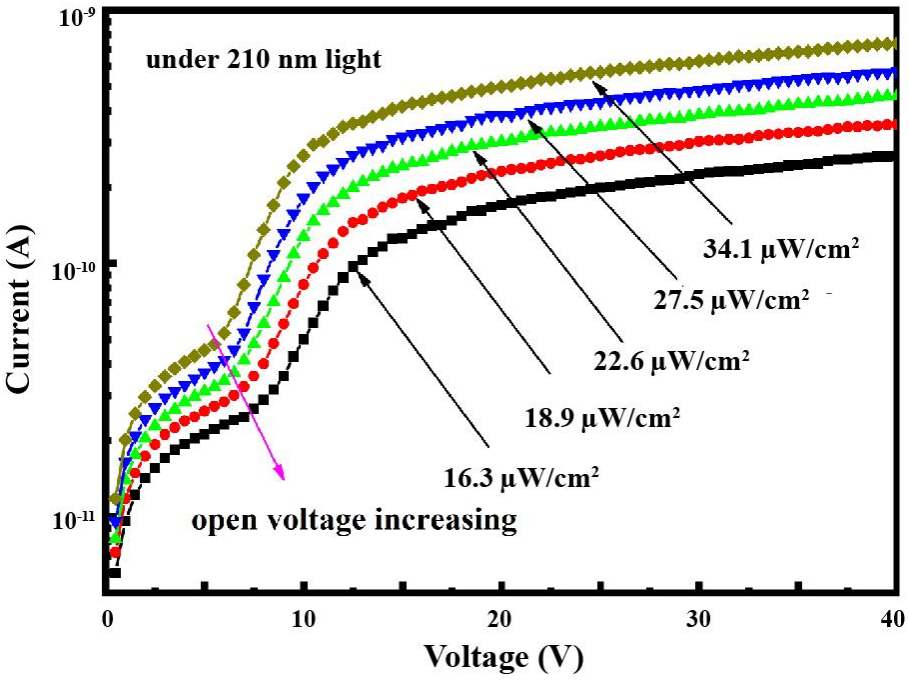

Figure 2-9 IV characteristics of the photodetector at different light power densities.

The difference in open voltage may be ascribed to the different number of electrons. Under 400 and 450 nm illumination, photogenerated electrons mainly come from nitrogen defects. Because the defect density is low, relatively fewer electrons are generated, resulting in a higher turn-on voltage. To validate this view, we tested IV characteristics under different light power densities, and the results are shown in Figure 2-9. It can be observed that with the decrease of light power density, the open voltage increases gradually. Since the number of photogenerated electrons is proportional to the optical power density, it can be concluded that the increase of the number of electrons will reduce the open voltage. Therefore, the photocurrent gain is related to the concentration of electrons.

Figure 2-4 (a) shows the responsivity and UV/visible rejection ratio at 210 nm and 400 nm of the detector. At 210 nm wavelength, the responsivity could be improved due to the existence of photocurrent gain. When the bias voltage is 3V, the responsivity is only 4.29 mA/W, while when the bias voltage is 12 V, the responsivity increases rapidly to 51 mA/W. On the contrary, at 400 nm, because there is no current gain, its responsivity is low and increases slowly with the increase of voltage. The rejection ratio of 210 nm/400 nm UV/visible light is also given. At low bias voltage, the rejection ratio is relatively small, and its value does not exceed 200. At high bias, the rejection ratio increases to more than 10^3 due to the rapid increase of responsivity at 210 nm.

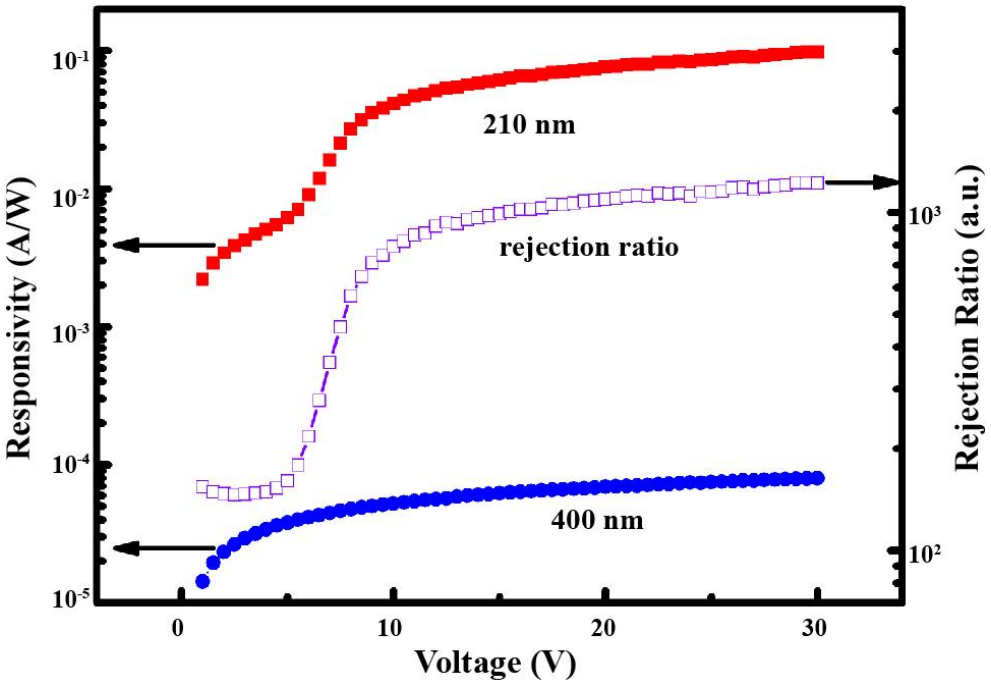

Figure 2-10 Responsivity and UV/Visible rejection varying with voltage.

Figure 2-10 shows the dependence of responsivity on optical power at 210 nm wavelength

with different bias voltage. When the bias voltage is 3 V, the responsivity almost remains unchanged with the increase of optical power. When the bias voltage is 7 V, the voltage is located in the current exponential gain voltage region, and its responsivity increases slowly with the increase of optical power. When the bias voltage is 12 V, the responsivity increases rapidly at low light power and slowly at high light power. These results show that the photocurrent gain can improve the responsivity of the detector.

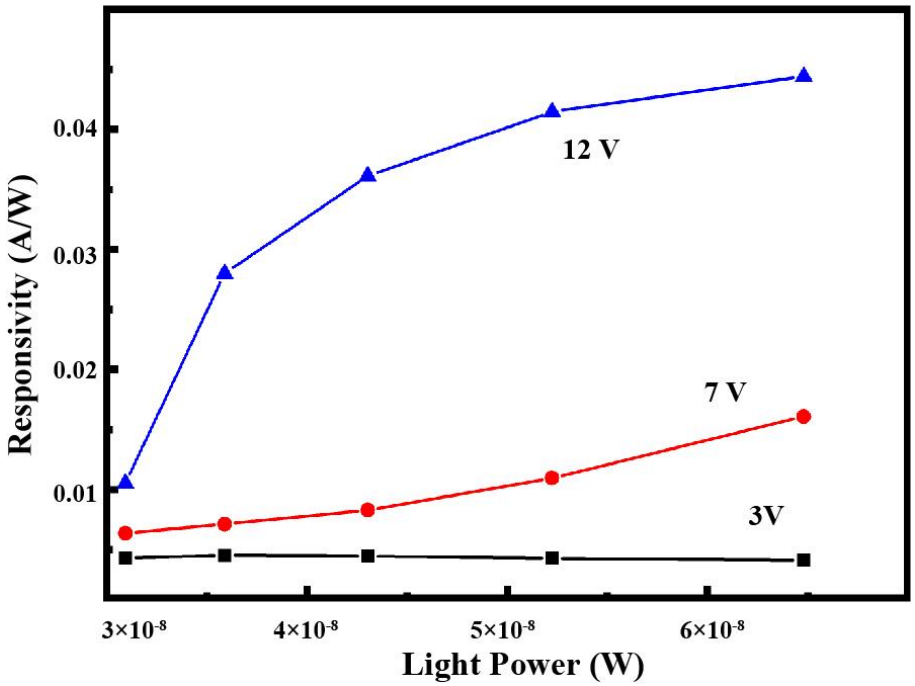

Figure 2-11 Responsivity of the diamond UV detector under 210-nm illumination depending on light power.

Figure 2-12 shows the time response characteristics of the photodetector. The bias voltage is 20 V, and the wavelength of incident light is 210 nm. The discontinuity of optical signal is realized by a metal shutter. It can be seen that the device has a good repeatability. Its rise time is 640 ms, and its falling time is 34 ms. In Liao *et al.*'s work [7], the transient response will slow down after the current gain is generated. This difference shows that the mechanism producing photocurrent gain is different. In their work, the photocurrent gain is caused by charge capture at metal/diamond interface, which leads to hole tunneling under a certain bias voltage. In our work, the photocurrent gain comes from the injection of electrons across the barrier. Therefore, the IV characteristics and transient response behavior are different. According to the time response measurement, the noise equivalent power is calculated to be 1.87×10^{-9} W at 210 nm, which indicates that the detector has a good performance.

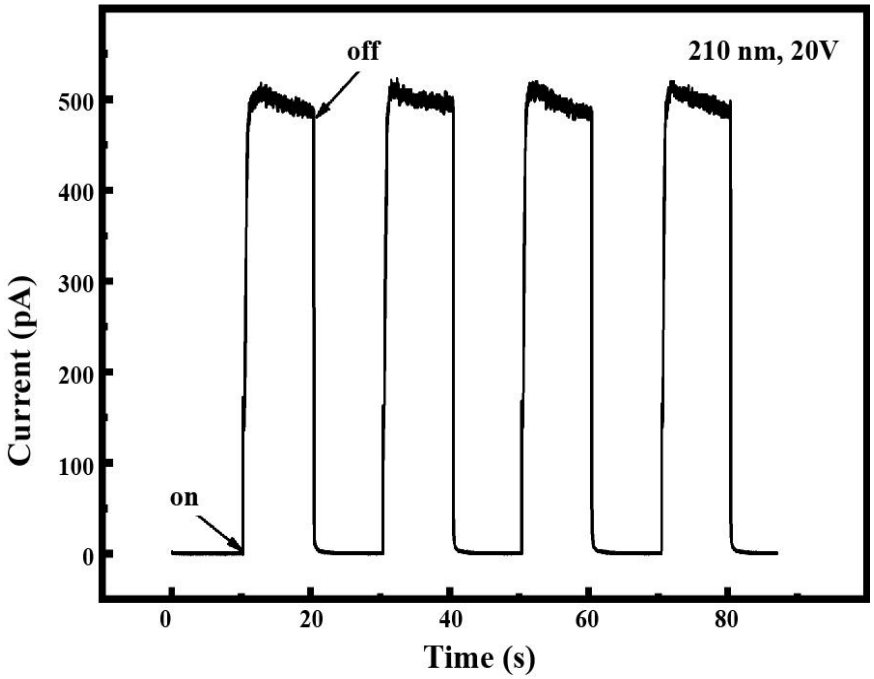

Figure 2-12 Transient response of the photodetector under illumination of 210nm and 20 V.

In addition to the current gain, the avalanche effect of the back-to-back Schottky barrier structure diamond ultraviolet detector at high voltage is realized. With the further increase of applied bias voltage, the photocurrent will undergo a second rapid rising process, as shown in Figure 2-13. It can be observed that the photocurrent increases rapidly after a certain voltage when the light wavelength is 205, 210 and 215 nm. At 210 nm, when the voltage is greater than 43.5 V, the current increases rapidly from 1 nA to 10 nA. The reason for this phenomenon is avalanche effect. Under the action of electric field, the photogenerated electrons in diamond will move to the positive electrode. When the applied bias is high, photogenerated electrons will gain enough energy to collide with the lattice to produce additional electron-hole pairs, which will produce avalanche effect. Because of the avalanche effect, the response at 210 nm at 50 V is 1.18 A/W. In Bin Zhao *et al.*'s work, avalanche effect can improve the responsivity and detectivity of ultraviolet detectors [47]. Therefore, the avalanche effect observed in diamond ultraviolet detectors is expected to improve device performance by optimizing the structure. It is noteworthy that the critical voltage of avalanche effect at 210 nm wavelength is the smallest, which is consistent with the lowest open voltage. It further confirms that the concentration of photoelectrons is the key factor to generate the photocurrent gain.

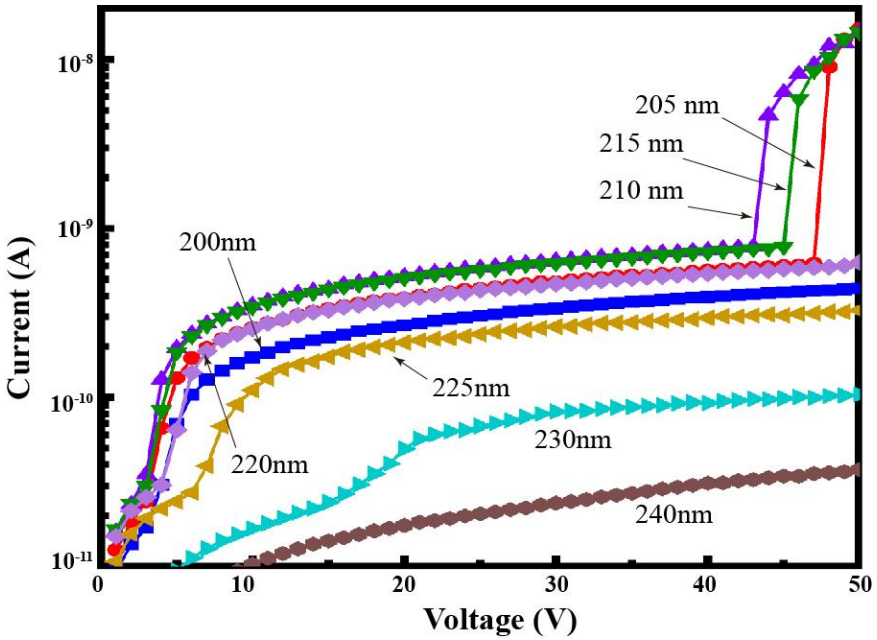

Figure 2-13 IV characteristics of the UV photodetector at different light wavelengths.

2.3 Summary

In this chapter, diamond UV photodetector with photocurrent gain were prepared, and the mechanism of the photocurrent gain was investigated. When the bias voltage is larger than the open voltage, the photogenerated electrons accumulated near the positive electrode/diamond interface can tunnel through the barrier and inject into the electrode, thus generating photocurrent gain. The turn-on voltage is related to the concentration of photoelectrons. The higher the concentration, the lower the turn-on voltage. Due to the existence of photocurrent gain in diamond ultraviolet photodetectors, the responsivity can be enhanced. When the bias voltage is less than the open voltage, the wavelength responsivity of 210 nm is only 4.29 mA/W; when the bias voltage is larger than the open voltage, the responsivity increases rapidly to 51 mA/W. When the voltage is further increased, the avalanche effect occurs, then the photocurrent increases 10 times rapidly, and the responsivity reaches 1.18 A/W at 50 V.

3 Groove-shaped three-dimensional single crystal diamond UV detector by bottom-up method

3.1 Introduction

UV photodetectors often work in extreme environments. Diamond is an excellent candidate for ultraviolet photodetectors because of its wide bandgap, high carrier mobility, radiation resistance, good thermal stability and chemical stability. In the early research, diamond UV photodetectors were mostly based on polycrystalline CVD diamond films. However, polycrystalline diamond films have a large number of grain boundaries and rough surface, which affect the fabrication and performance of devices. In 2004, the rapid growth technology of CVD single crystal diamond achieved a breakthrough [48,49]. As a result, the research of diamond UV photodetectors based on CVD single crystal diamond epitaxial layer was carried out rapidly, showing excellent device performance and obtaining the most sensitive diamond ultraviolet photodetectors. Therefore, single crystal diamond ultraviolet detectors have been widely studied in recent years. After the improvement of the film quality, the researchers optimized the device structure, including stack structure and three-dimensional graphite electrode structure. In the diamond radiation detector, the three-dimensional structure occupies an important position. B. Caylar *et al.* uses femtosecond laser processing technology to fabricate columnar electrode arrays in single crystal diamond. The top of the columnar electrode is connected by the interdigital electrode on the surface to obtain the detector. These graphite electrodes have electrode activity, which can effectively collect the charges generated in diamond and improve the collection efficiency [50] compared with the planar structure. However, femtosecond laser processing can produce surface stress, even cracks, which will affect the performance of devices. Another three-dimensional electrode fabrication method is to use reactive ion (RIE) etching technology to fabricate grooves on the surface of diamond, and then cover the grooves with metal electrodes to obtain three-dimensional electrode structure to improve the charge collection efficiency [51]. However, this electrode structure has not been applied to diamond ultraviolet photodetectors. In this chapter, grooved three-dimensional electrode structure are applied to single crystal diamond photodetectors, and their properties are characterized.

3.2 Investigation of selective growth of diamond

Up to now, the preparation of three-dimensional diamond ultraviolet detectors is mainly from the top to the bottom, that is, etching technology and laser processing technology are used to prepare a structured surface, then the electrode is fabricated to collect these structures. In this method, the etching process will introduce defects, and the alignment problem will also exist in multiple lithography process. In order to solve this problem, we propose a new fabrication method which is called bottom-up method. First, the electrode pattern is prepared on the diamond surface, then it is put into the MPCVD chamber for a second epitaxial growth on the uncovered diamond, so that the photodetector can be obtained directly. This growth method with a metal mask is also called selective growth method. Because the key of bottom-up method is selective growth, it should be investigated to obtain a good-performance detector.

(1) Selection of mask metal

In the selection of mask metals, two aspects need to be considered. On one hand, the substrate temperature may reach 1000 ℃ or even higher during the diamond epitaxial process, thus the first requirement is that the mask metal should have a higher melting point. On the other hand, some metals may cause other products in the selective growth process. Therefore, the metal should be stable during growth.

Two groups of comparative experiments were designed. One is for melting point investigation and another is for stability investigation. The used metal and growth parameters were shown in Table 3.3. Sample A and B were used to study the effect of melting point on morphology. High melting point tungsten was used in sample A and low melting point nickel was used in sample B. The thickness of the metal mask is 150 nm, and the temperature is maintained at 1000 ℃ during the growth process.

Table 3-1 Selective growth conditions used in this experiment.

Sample	Metal	Thickness (nm)	CH_4 (sccm)	H_2 (sccm)	Temperatur (℃)	Pressure (kPa)	Time (min)
A	W	150	20	480	1000	13	10
B	Ni	150	20	480	1000	13	10
C	W	100	20	480	900	13	10
D	Pd	100	20	480	900	13	10

Figure 3-1 shows the optical morphology of sample A and sample B before and after growth. It can be seen that the tungsten mask is relatively intact after growth, while the nickel mask becomes nanoparticles after growth. For tungsten metal, its melting point is as high as 3422 ℃, so it will not melt at growth temperature of 1000 ℃. Hence the metal retains relatively well and the diamond film only grows on the uncovered area, as shown in Figure 3-1(b). For nickel metal, although its melting point is 1455 ℃, higher than the substrate temperature, its thickness is 150 nm, the melting point will be reduced compared with larger size material. Therefore, in the growth process, the melting shrinkage of nickel film occurs, which makes the growth area appear in the metal-covered area, as shown in Figure 3-1(d).

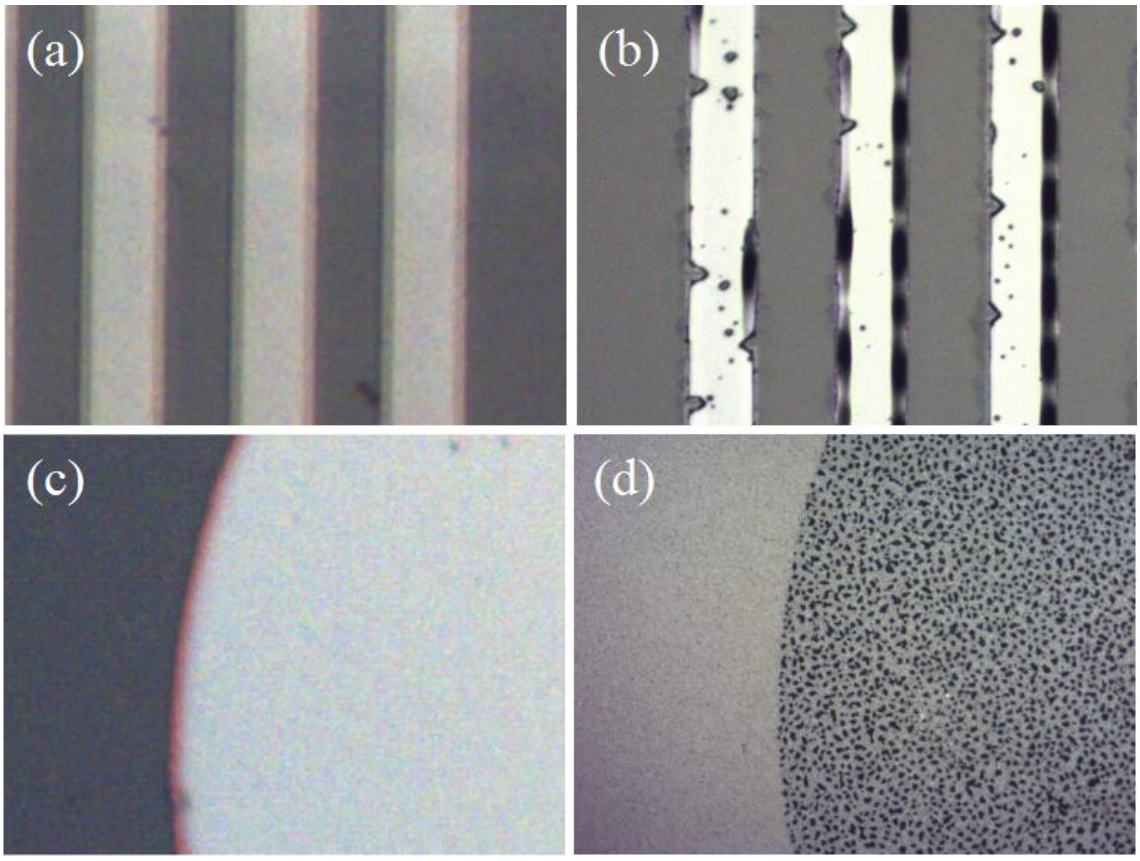

Figure 3-1 Optical images of sample A (a) before and (b) after growth and sample B (c) before and (d) after growth .

Sample C and D were used to study the effect of metal stability on morphology. Because the melting point of Pd is 1554.9 ℃, the substrate temperature was set to 900 ℃ in order to avoid melting during the growth process. Figure 3-2 shows the surface morphology of sample C and sample D before and after growth. It can be seen that after the growth, although tungsten mask exists metal shedding phenomenon, the metal area is smooth and

clean, and no other carbon materials are formed, as shown in Figure 3-2(b). For the palladium mask, the metal region becomes black after growing in the MPCVD chamber, as shown in Figure 3-2 (d). This indicates the formation of other carbon materials.

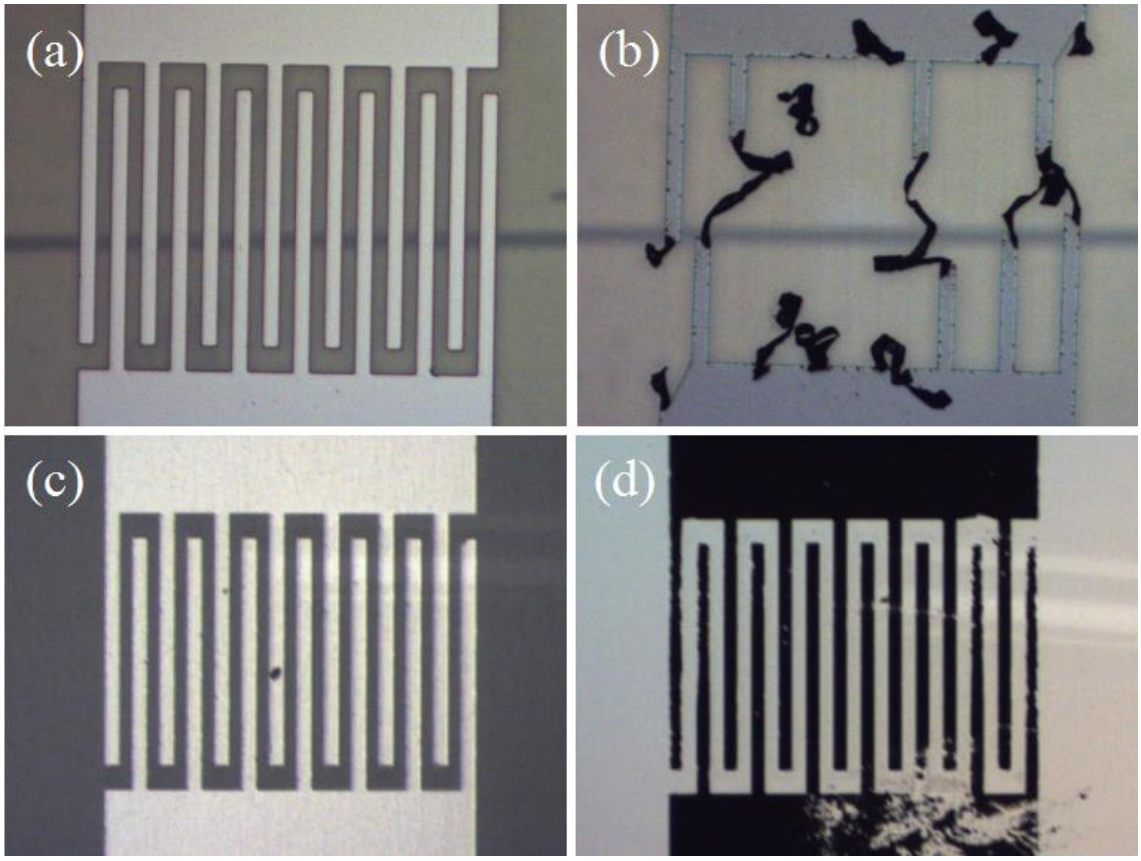

Figure 3-2 Optical images of sample C (a) before and (b) after growth and sample D (c) before and (d) after growth.

In order to further prove whether other material was formed during growth, Raman characterization was taken for sample D and the results are displayed in Figure 3-3(a). There is only a single peak at 1331.9 cm^{-1} which is the characteristic peak of diamond in the uncovered area, indicating that the uncovered area is diamond. On the contrary, there are two peaks in Raman spectrum for metal region, one located at 1344.2 cm^{-1} and the other at 1582.5 cm^{-1}. For carbon materials, there are two characteristic peaks in the range of 1100 cm^{-1}-1800 cm^{-1}, namely G peak (graphite) near 1580 cm^{-1} and D peak (defect) near 1360 cm^{-1}. G peak is the symmetrical vibration of optical mode, corresponding to the characteristic peak of SP^2 C-C bond vibration. D peak is the vibration caused by defects. The Raman peaks of the ferrous materials in the metal region correspond to the D and G peaks, indicating that the composition of the ferrous materials is SP^2 carbon. Figure 3-3(b) shows the SEM image of the metal region. It can be seen that there exists a large number of

nanowires. By combining Raman characteristic peaks and the morphology, we can confirm that these nanowires are carbon nanotubes [52-55]. This indicates that palladium can act as a catalyst and cause the growth of carbon nanotubes during the MPCVD growth process. These carbon nanotubes are easy to fall off, thus affecting the stability of the device.

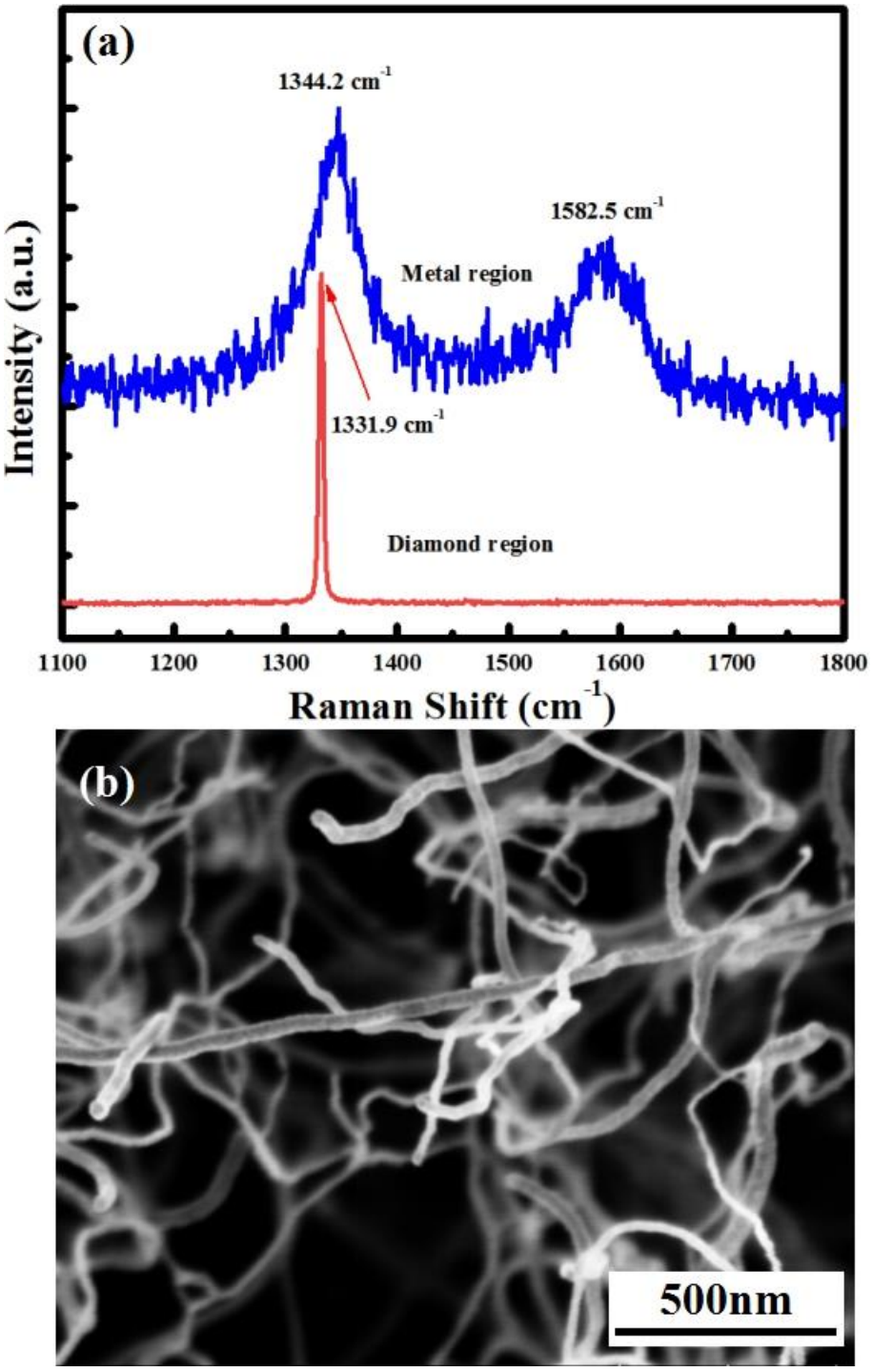

Figure 3-3 (a) Raman spectra of metal area and diamond area. (b) SEM image of metal area.

In summary, when choosing the mask metal, the melting point should be high and no other

carbon material products are catalyzed in the CVD process. Tungsten metal is a suitable metal with high melting point and good stability.

(2) Optimizing the Selective Growth Process

After tungsten is identified as the mask metal, the growth process needs to be optimized, because it will be stripped from diamond, as can be seen in Figure 3-2 (b). This makes the electrodes incomplete, further affecting the usage of the photodetector. Because the process of growing high quality diamond epitaxial layer is relatively mature, the optimization of the process is mainly focused on the change of metal thickness and process order.

Firstly, the metal thickness effect on selective growth morphology is studied. Two diamond substrates are prepared, one is to fabricate 150 nm thick tungsten electrode pattern on the surface, the other is to fabricate 30 nm thick tungsten electrode pattern on the surface. The two samples were put into MPCVD chamber for selective growth. The epitaxial growth parameters were CH_4/H_2=4%, gas flow rate of 500 sccm, substrate temperature of 900 ℃, pressure of 13 kPa, microwave power of 1 kW and growth time of 5 min. Figure 3-4 shows the morphology of the selectively grown samples with tungsten film thickness of 150 nm and 30 nm. It can be found that when the film is thicker, the metal is easy to fall off from the diamond surface, which makes the electrode incomplete. When the film is thin, the metal is not easy to fall off from the diamond surface, so the electrode pattern is very complete. We think that the main reason for the stripping of metal from diamond is due to the thermal expansion difference. The thermal expansion coefficient of diamond is 1.2 μm/K, while that of tungsten is 4.6 μm/K. In the heating process, tungsten expands rapidly and easily produces stress at the interface, which leads to metal fracture and warping. The reason that the thicker the film is, the easier it will fall off is mainly related to the plasma during the growth process. Microwave is an electromagnetic field. Under the action of microwave, plasma spheres can be produced in the chamber. When the metal is thicker, the metal is a protuberance relative to the diamond surface, which has the effect of gathering electric field. Thus, the plasma sphere mainly concentrates on the metal surface. Under the action of hydrogen plasma, the metal is heated rapidly, while the surface of diamond is heated relatively slowly, resulting in a large difference in thermal expansion, which makes the metal fall off from diamond. When the metal is thinner, the effect of the electric field on the metal surface is weakened, the difference between the electric field on the metal surface and that on the diamond surface is small, and the heating speed of the metal becomes slower, which can make the interface release stress in a short time. Therefore the metal is not easy to fall

off.

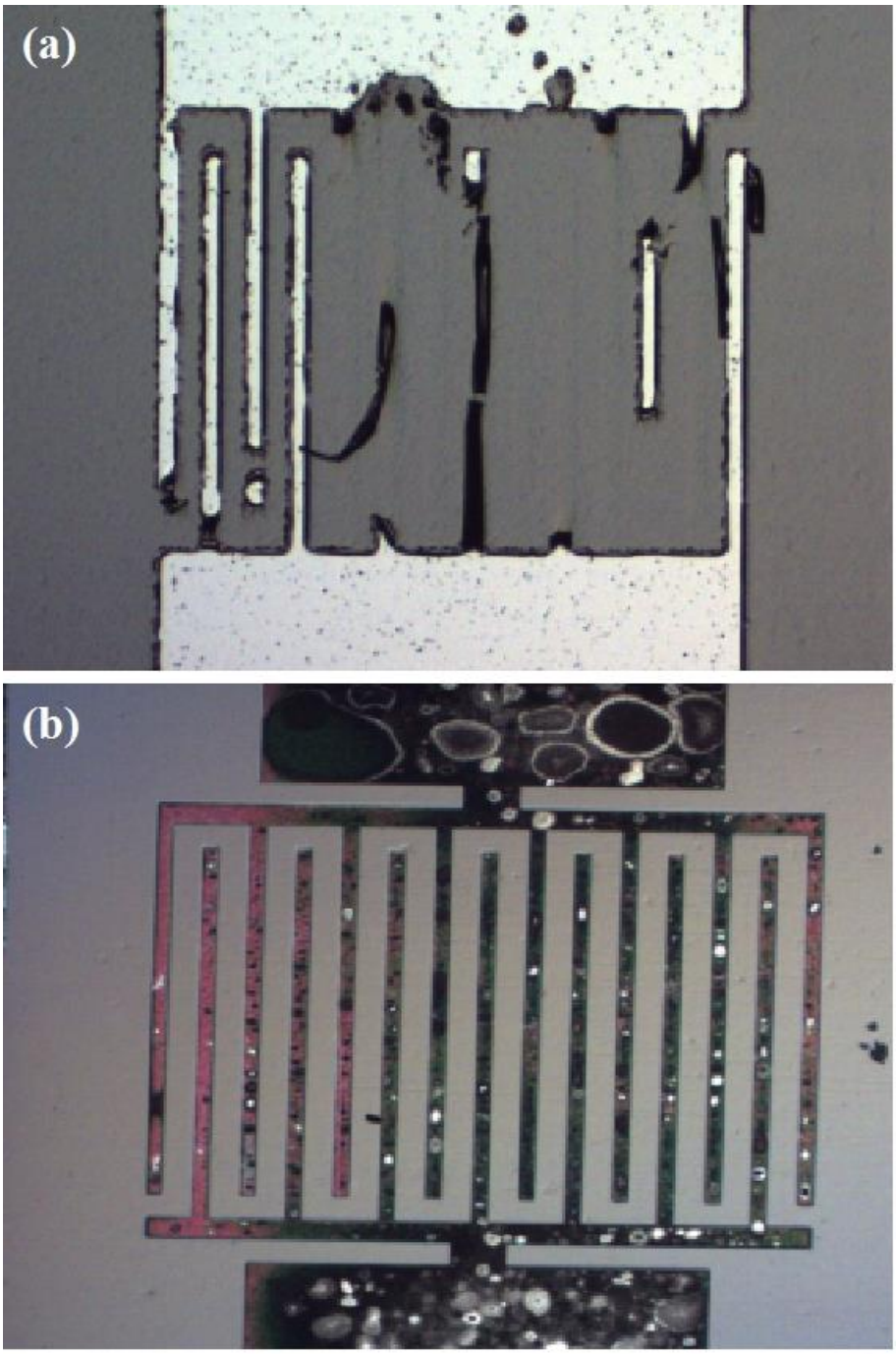

Figure 3-4 Optical images of samples with (a) 150 nm and (b) 30 nm thick tungsten after selective growth.

Since metal shedding is related to expansion, we can optimize it from two aspects so that thick metal masks do not fall off during selective growth process. On the one hand, the heating rate in the chamber should be slow. In general, hydrogen is first used to glow at low chamber pressure, then hydrogen flow rate and chamber pressure are increased to the growth conditions, and finally methane is introduced for growth. In this condition, the temperature

increases rapidly. Therefore, we introduce methane into the chamber after the starting of glowing, so that the heating rate of the substrate will be slower. On the other hand, to reduce metal/diamond interface hanging bonds and improve adhesion, the sample was annealed at 500 ℃ annealing before growth process [56]. Figure 3-5 shows the optical image of the selectively grown sample under an optimized growth process. The tungsten film was 300 nm thick, and the sample was annealed at 500 ℃ for 10 minutes before placed into the MPCVD chamber. After hydrogen glow, methane is directly introduced into the chamber, and then the chamber pressure and hydrogen flow rate are increased to the growth conditions. The growth parameters are CH_4/H_2=4%, gas flow rate of 500 sccm, substrate temperature of 1000 ℃, chamber pressure of 13 kPa, and growth time of 10 min. It can be seen that the metal strip is very complete and the diamond surface is smooth. This shows that the heating rate of metals can be effectively reduced by immediately adding methane after glowing, so that the stress can release at the metal/diamond interface and the integrity of the electrode pattern can be better maintained. It is noteworthy that bulging still exists on metal bars. This is because the stress can not be completely released, so the metal will still expand.

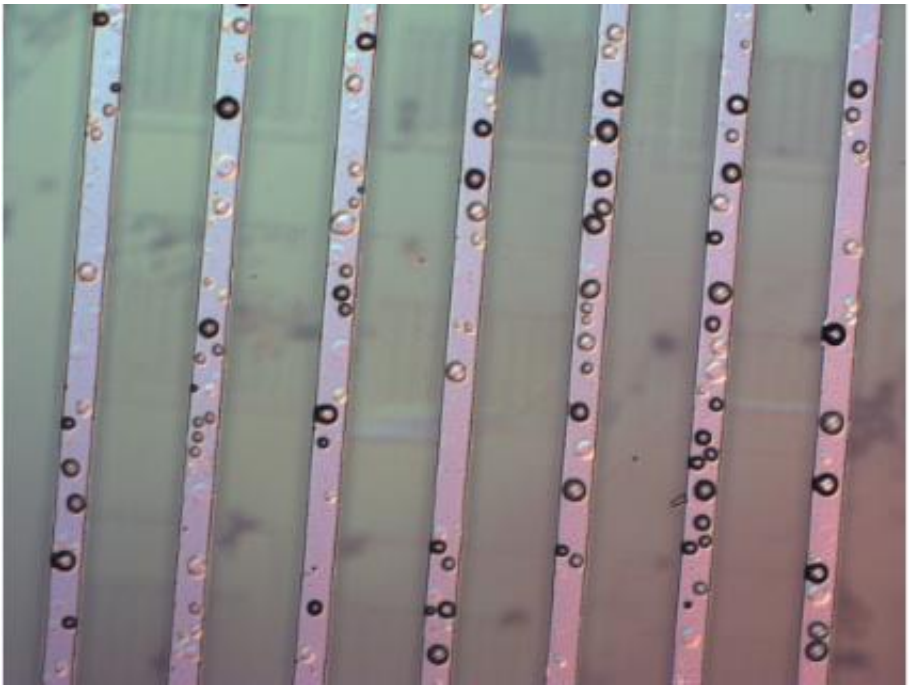

Figure 3-5 Optical image of selective grown diamond sample at a optimized growth process.

3.3 Groove-shaped photoconductive three-dimensional diamond UV detector

Using the selective growth process, we can fabricate a three-dimensional diamond

structure photoconductive UV detector. 3 mm×3 mm×0.3 mm HPHT IIa-type single crystal diamond was used as the substrates. After acid, alkali and organic cleaning, 300 nm thick single crystal diamond epitaxial layer was grown through MPCVD method, as shown in Figure 3-6(a) and (b). The epitaxial growth condition is as follows: the total flow rate of reaction gas is 500 sccm, the ratio of CH_4 to H_2 is 1%, the process pressure, growth temperature and microwave power are 13 kPa, 900 ℃ and 1 kW, respectively. After growth, the diamond sample was heated for 1 hour at 250 ℃ in sulfuric acid and nitric acid mixture to remove hydrogen termination. Next, tungsten interdigitated electrodes were fabricated on the epitaxial layer surface by photolithography, magnetron sputtering and lift-off process, as shown in Figure 3-6(c). The width of the interdigitated electrode is 30 μm, the distance between the two electrodes is 50 μm, the total active area is about 0.65 mm^2, and the thickness of the electrode is 30 nm. After preparing the electrode pattern, the sample was put into the MPCVD chamber again for the second epitaxial growth, as shown in Figure 3-6(d). The growth condition was: CH_4/H_2=4%, total flow rate of reaction gas 500 sccm, substrate temperature 1000 ℃, pressure 13 kPa, thickness of epitaxial layer 500 nm. In order to increase the growth rate, N_2 was added to the secondary epitaxial process. After growth, a 3D UV detector with alternating metal and diamond arrays is obtained.

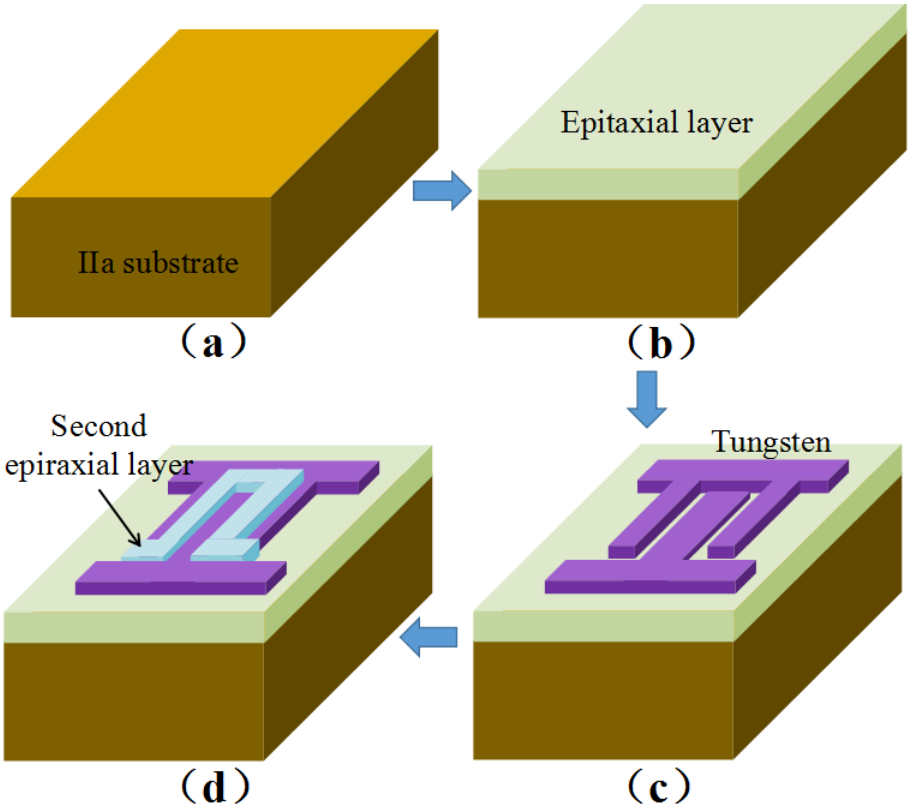

Figure 3-6 Fabrication process of the groove-shaped photoconductive 3D diamond UV

detector. (a) Substrate preparation; (b) Epitaxial growth; (c) Tungsten electrode deposition; (d) Second epitaxial growth.

Figure 3-7(a) shows the optical image of the three-dimensional structure detector fabricated by bottom-up method. It can be seen that the surface morphology of the samples is similar to that of the samples in Figure 3-4(b), because the growth conditions of the two samples are basically the same. The black stripe area in the figure is the metal electrode area, while the white area between the black stripes is the selectively grown diamond area. The surface of the diamond area is very smooth, but the surface of the metal area is rough and does not have metallic luster. On the contrary, black, red and green colors can be seen. These phenomena indicate that chemical reactants are formed on the metal surface.

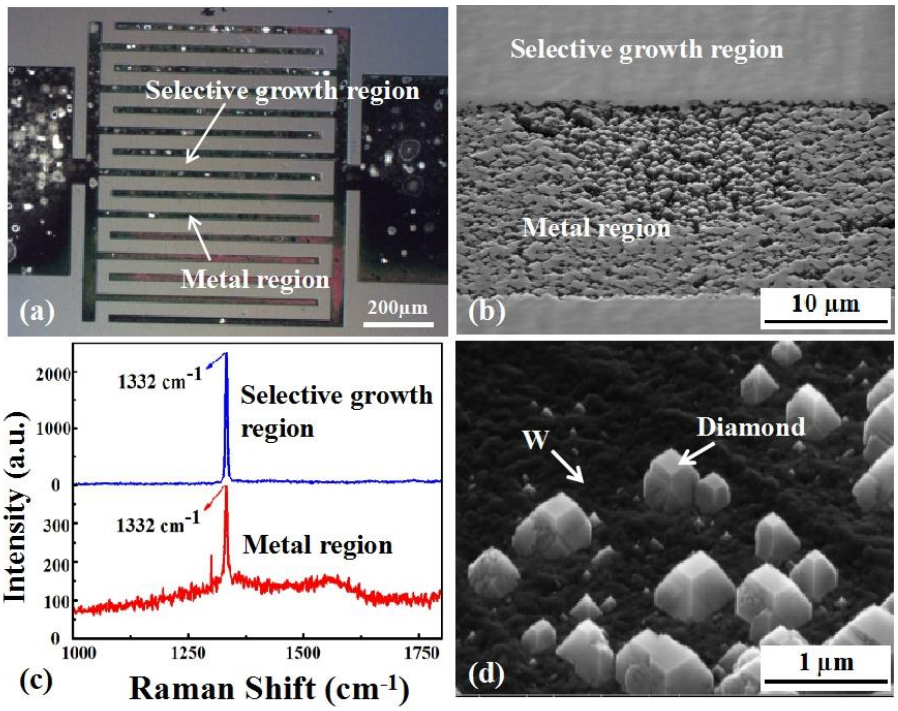

Figure 3-7 (a) Optical image and (b) SEM image of the three-dimensional diamond UV photodetector. (c) Raman spectra of taken from metal region and selective growth region. (d) Magnification of the diamond particles.

Figure 3-7 (b) gives the SEM image of the metal region, from which it can be seen that a layer of film has also grown in the metal region. The surface morphology of the film is similar to that of diamond film, so it is preliminarily judged to be diamond. In order to accurately determine the composition of the film formed in the metal region, Raman spectroscopy was used to characterize the film. Figure 3-7 (c) gives the Raman spectra of the metal region and selective growth region. For the selective growth region, only the

characteristic peaks of diamond exist at 1332 cm^{-1}, which indicates that the quality of the selective grown diamond layer is high. For the metal region, there is a diamond characteristic peak at 1332 cm^{-1}, which indicates that the film is diamond. Because of the existence of diamond film, it can reflect and scatter light, exhibiting many kinds of colors. In addition to black and color, there are white bright spots in the metal area. Further enlargement of the bright spot area is shown in Figure 3-7 (d). It can be seen that only a small amount of diamond nanoparticles exist, while the black pleated material under the diamond nanoparticles is tungsten metal. Tungsten metals show metallic luster under a microscope, and its surroundings are dark covered by diamond particles, thus producing bright spots.

After selective growth, hydrogen termination exists on the diamond surface, which will affect the IV characteristics. Figure 3-8 shows the IV characteristics of the as-fabricated three-dimensional diamond UV photodetector under dark and 210 nm illumination conditions. The IV curve is linear, indicating that the contact between metal electrode and diamond is ohmic. Therefore the photodetector is photoconductive detector. The dark current of the detector is very high, reaching 4.33 mA at 5 V, which indicates that the hydrogen-terminated surface of is very conductive. It is noteworthy that the photocurrent is lower than the dark current. This means that the device has a poor photoresponse performance which is caused by the hydrogen termination.

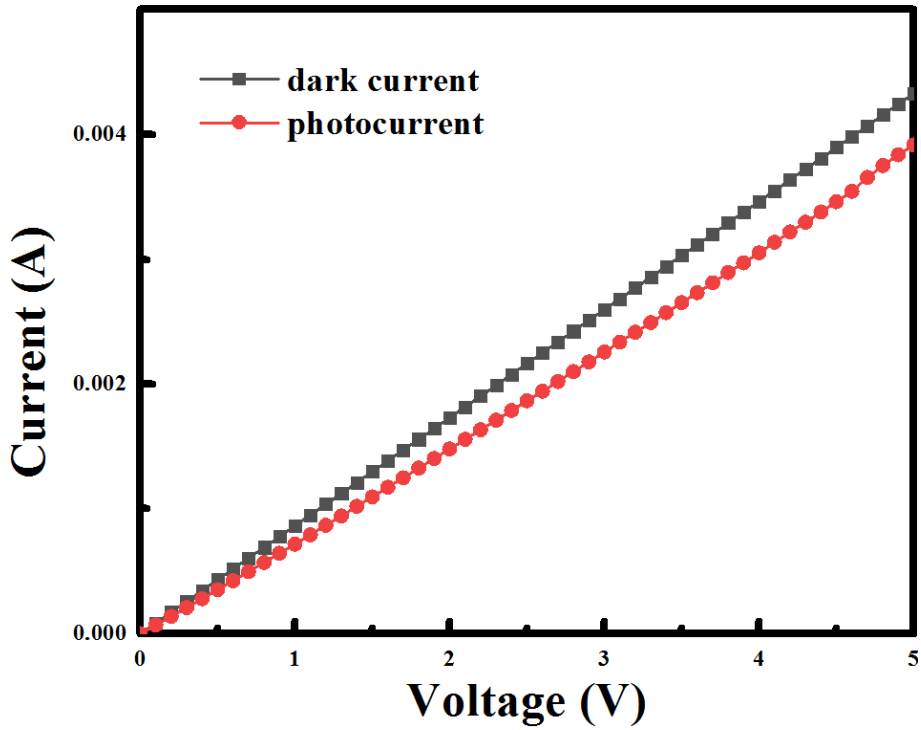

Figure 3-8 IV characteristics of the as-fabricated three-dimensional UV photodetector under dark and 210 nm illumination conditions.

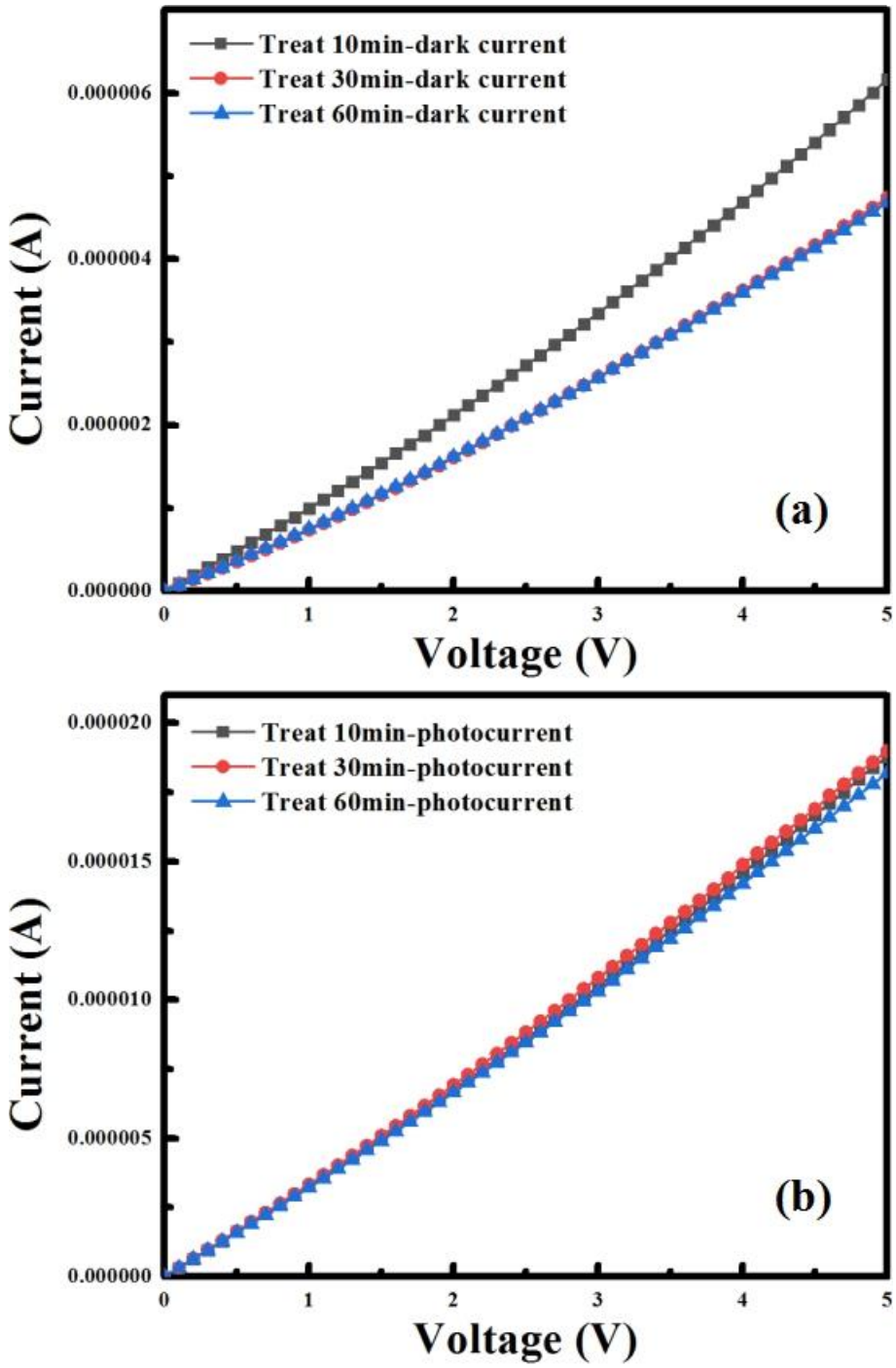

Figure 3-9 IV characteristics of the three-dimensional UV photodetector under (a) dark and (b) 210 nm illumination conditions after UV-ozone treatment of 10 min, 30 min and 60 min.

To improve the device performance, UV-ozone treatment was used to change the hydrogen termination into oxygen termination. Figure 3-9 (a) and (b) show the dark current and photocurrent characteristics of the detector after 10 min, 30 min and 60 min UV-ozone treatment, respectively. After 10 minutes of treatment, the dark current of the sample decreases rapidly compared with as-fabricated detector. With treating time increases, the

dark current further decreases and reach a stable value. This indicates that most surface hydrogen termination has been removed after 30 minutes UV-ozone treatment. The photocurrent characteristics of the detector are different from those of the as-fabricated detector. At 5 V, the photocurrent of the detector treated for 10 min, 30 min and 60 min is 18.8 μA, 19 μA and 18.2 μA, respectively, which is larger than the dark current of the device. This indicates that the removal of hydrogen termination is beneficial to improve the photoresponse of the detector. The IV curve under illumination is also linear, indicating that the detector is a photoconductive detector.

Figure 3-10 shows the spectral responsivity of the detector at different voltages, displaying similar behaviors except for the value. Under 220 nm illumination, the responsivity at 5 V bias is 9.36A/W, and at 10 V bias is 19.88 A/W, which is almost twice as much as that of 5 V bias. This is accordance with the characteristics of photoconductive detector. At different voltages, the responsivity under visible light is very small, showing a typical spectral selectivity. The 220 nm/600 nm UV/visible light rejection ratio at 5V can reach 10^3. It is noteworthy that the detector has a weak responsivity peak in the range of 370-460 nm, which is caused by the N3 centers in the diamond [35]. The presence of N3 centers indicates that there is a small amount of nitrogen in diamond, which comes from the small amount of nitrogen added during the second growth process.

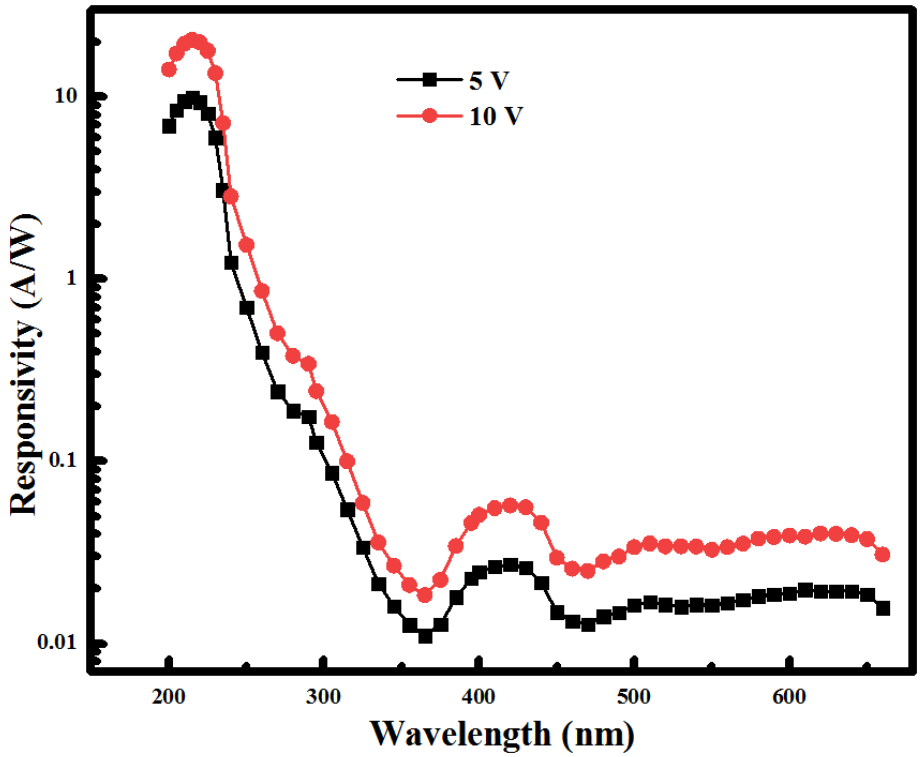

Figure 3-10 Spectral responsivity of the detector at 5 V and 10 V.

In order to study the time response of the detector, the detector was irradiated with discontinuous light for 60 minutes. The wavelength of the detector was 220 nm and the bias voltage was 3 V. Figure 3-11 shows the current-time curve of the detector. In the absence of light, the current of the device is low. When illumination is applied, the current increases rapidly at first, then increases slowly after reaching a certain value, and tends to be saturated with time. After removing the optical signal, the current decreases rapidly first, and then slowly with time. In the 200 s test time range, the current can not return to the current level before the optical signal is applied. The transient response curve is a typical persistent photoconductivity phenomenon, which may be caused by some defects in diamond, such as N3 center. These defects can capture carriers and slow down the rising and falling time. Nevertheless, the detector still has good time response repeatability, as shown in the illustration in Figure 3-4.

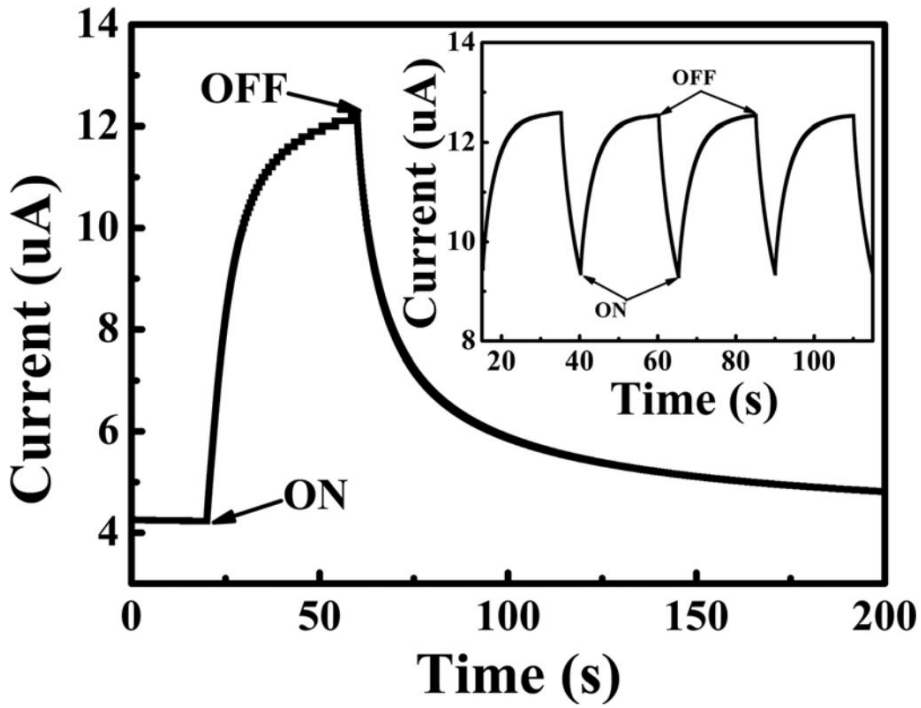

Figure 3-11 Time response of the detector under 220 nm illumination. The light power density is 222 μW/cm^2, and the applied bias is 3 V.

In the process of ultraviolet ozone, the dark current of the detector decreases by default due to the removal of surface hydrogen terminals. But another possible reason is the oxidation of electrode materials. In order to determine whether the oxidation of the electrode material leads to the decrease of conductivity, we tested another detector with defective electrode pattern. The optical morphology of the detector is shown in Figure 3-4(a). The detector was treated by 10 min, 20 min and 30 min UV-ozone, 40s and 60s induction ion

coupled oxygen plasma etching, and 1 h sulfuric acid/nitric acid mixture boiling at 250 ℃, sequentially. After each step, the resistance of the same electrode pad and the current between the two electrode pads were measured. The results are shown in Figure 3-12. As can be seen from the figure, the resistance between the same electrode pad is very small. Before acid treatment, the resistance value is around 53 Ω, which indicates that the electrode material can maintain good conductivity under ultraviolet ozone and oxygen plasma environment, thus eliminating the reason for the reduction of conductivity caused by oxidation of the electrode material. After acid treatment, the resistance of the electrode increases slightly to 66 Ω, and the good conductivity is maintained. The results show that the electrode has a good stability after selective growth.

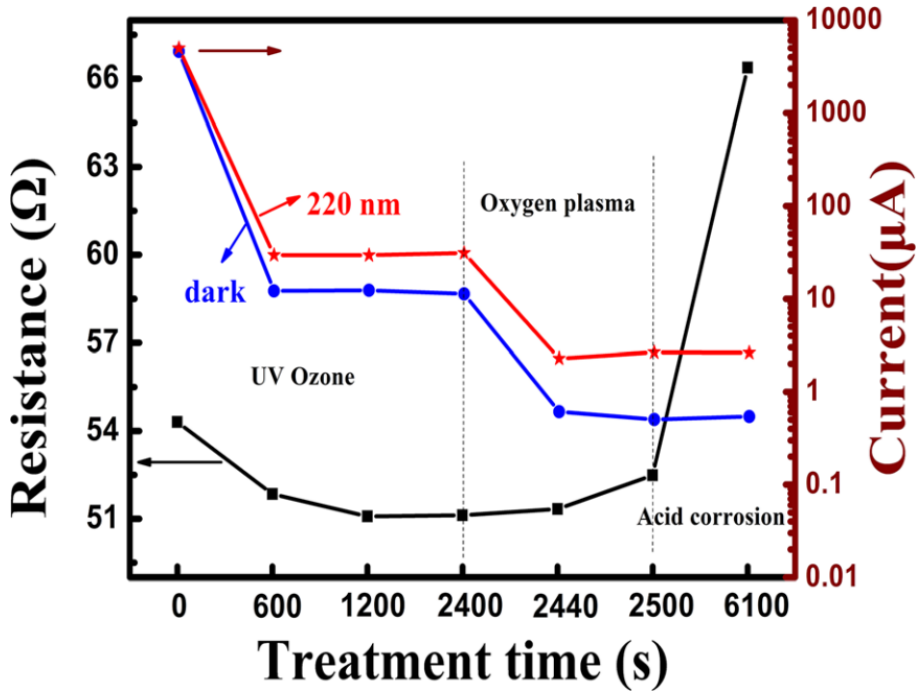

Figure 3-12 The electrode resistance, dark current and photocurrent under 220 nm light at 5 V versus different treatment time. UV-ozone treatment, oxygen plasma treatment and acid corrosion treatment were sequentially applied.

Figure 3-12 also shows the dark current and 220 nm photocurrent of the detector at 5V. As can be seen from the figure, the changing trend of dark current and photocurrent is the same, and there are two decreasing steps. The first decrease step occurs after 10 minutes of UV-ozone treatment, which is due to the removal of surface hydrogen termination, thus reducing the conductivity of the device. Because the oxygen-terminated surface will not change after the removal of hydrogen termination, the current value will not change significantly with the prolongation of UV-ozone treatment time. The second decrease step

occurs after the 40 s oxygen plasma treatment, which is caused by the change of oxidation mode. Some work has shown that when the hydrogen-terminated diamond surface is treated by UV-ozone, the hydroxyl (-OH) group is produced by the combination of oxygen and hydrogen to oxidize the diamond surface [57,58]. However, in the process of oxygen plasma treatment, the diamond surface will be etched, and then the -OH group can be completely removed. In this way, under the condition of oxygen-rich ions, the carbon hanging bond on the surface will combine with oxygen to form the C-O bond, so that the oxygen-terminated surface of diamond is mainly C-O group [59]. No matter which oxidation method is used, there is a clear contrast between the photocurrent and the dark current of the device.

In addition to the good stability of the electrode, the bottom-up method has another advantage that the device can automatically form ohmic contact during the growth process. The IV curve of the detector is linear whether the electrode pattern is complete or not, indicating that the tungsten/oxygen-terminated diamond forms ohmic contact. The results show that some changes have taken place in the interface at tungsten/oxygen-terminated diamond interface during the growth process. Figure 3-13 (a) shows the surface morphology of the detector after boiled in acid mixture for 1 hour. Compared with 3-4 (a), the metal region loses the white metallic luster and becomes gray. This is because the tungsten/diamond interface is exposed after the tungsten is dissolved by acid. However, some other substances exists at the interface and dissolve slowly in acid, so they can remain after 1 h corrosion. Raman spectroscopy was used to measure the metal region before and after acid treatment. The results are shown in Fig. 3-13 (b). There is no Raman peak in the pad area before acid treatment because the presence of tungsten prevents the laser from reaching the tungsten/diamond interface. After acid etching for 1 hour, tungsten metal dissolves in large quantities and exposes tungsten/diamond interface. At this time, two Raman peaks appeared in the Raman spectrum, located at 1353 cm^{-1} and 1595 cm^{-1}, respectively. These two peaks are produced by graphite. 1353 cm^{-1} is caused by the size effect of graphite. Its small or large grain boundaries activate the A1g mode of the lattice to produce Raman peaks [60]. The peak of 1595 cm^{-1} displaces 15 cm^{-1} shift compared with G peak of 1580 cm^{-1} for graphite, which may be caused by the insertion of tungsten atoms into graphite layer [61,62]. The results show that tungsten induces graphitization of the interface during the growth process, which changes the contact between tungsten and oxygen-terminated diamond from Schottky contact to ohmic contact. Therefore, bottom-up method can effectively fabricate three-dimensional UV photodetectors with high

responsivity and good electrode stability, and metal-diamond contact can also form ohmic contact, eliminating annealing process.

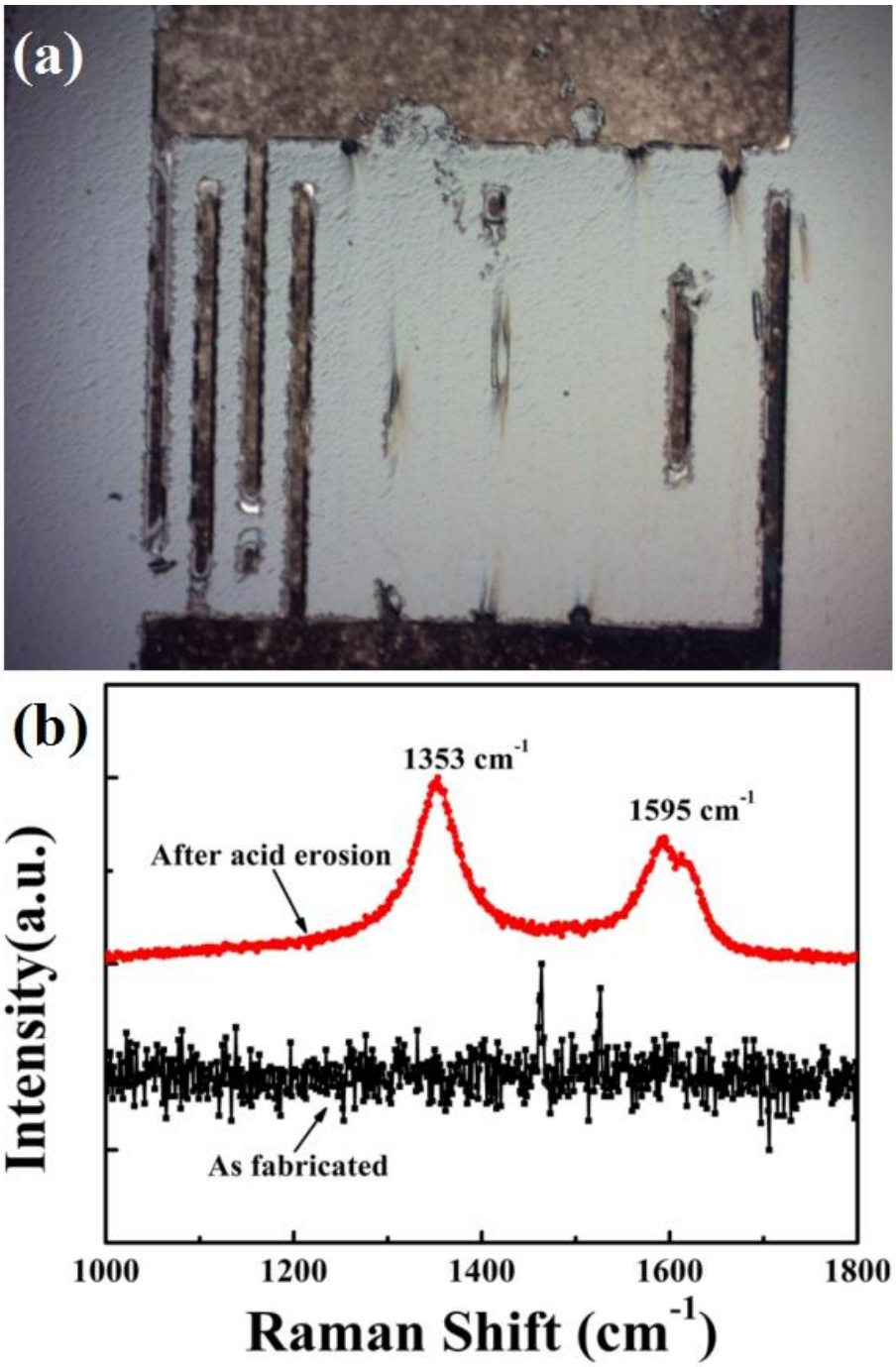

Figure 3-13 (a) Optical image of the detector after boiled in acid mixture for 1 hour. (b) Raman spectra of the metal region before and after acid dissolving.

3.4 Groove-shaped photoconductive three-dimensional diamond UV detector

In the study of photoconductive detectors, we find that bottom-up growth method can introduce impurities and defects in selective epitaxial diamond films. Although these defects can increase the responsivity of detectors, they also cause persistent photoconductivity and large dark current. In order to suppress the dark current and improve the time response characteristics, we have developed a three-dimensional photovoltaic structure detectors based on bottom-up method.

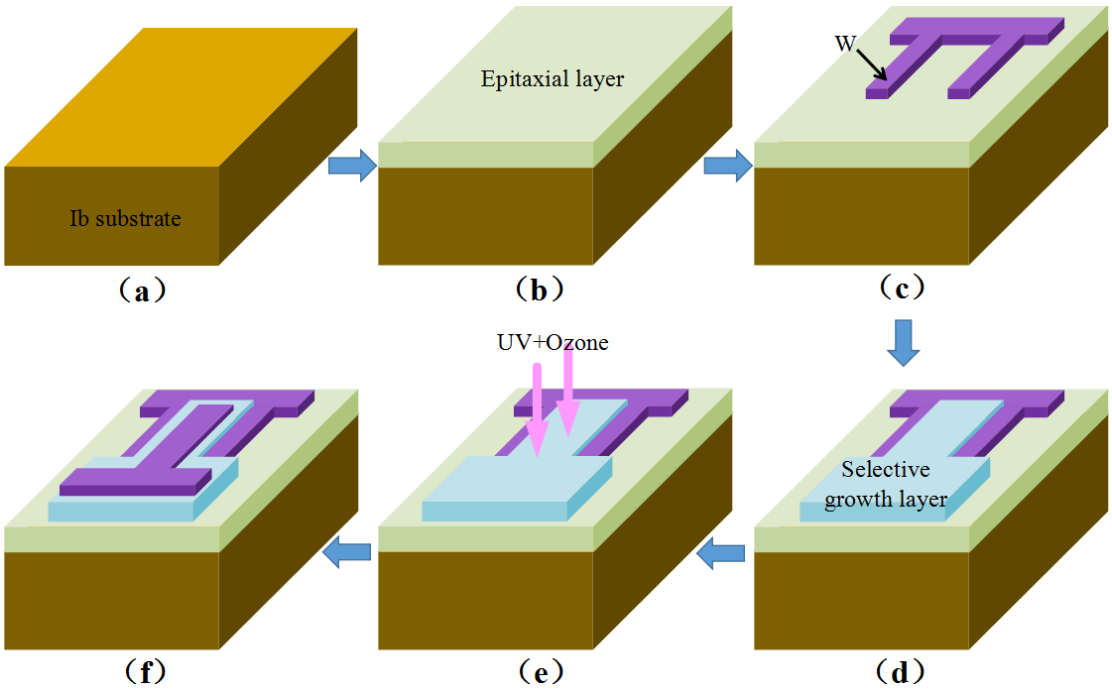

Figure 3-14 Fabrication process of the groove-shaped photovoltaic 3D diamond UV detector. (a) Substrate preparation; (b) Epitaxial growth; (c) Half tungsten electrode deposition; (d) Second epitaxial growth; (e) UV-Ozone treatment; (f) Another Half tungsten electrode deposition.

Figure 3-14 is the fabrication process of the photovoltaic three-dimensional diamond UV photodetector. The substrate is 3 mm×3 mm×0.3 mm HPHT Ib-type (100) oriented single crystal diamond. After acid, alkali and organic cleaning, a thin diamond epitaxial layer was grown on the substrate, as shown in Figure 3-14(a) and (b). The total flow rate of reaction gas is 500 sccm, the ratio of CH_4 to H_2 is 1%, the process pressure, growth temperature and microwave power are 13 kPa, 900 ℃ and 1 kW, respectively, and the thickness of epitaxial layer is 300 nm. After growth, the diamond sample was heated for 1 hour at 250 ℃ in the sulfuric acid/nitric acid mixture to remove the hydrogen termination. Next, half interdigitated W electrodes pattern was prepared on the epitaxial layer surface by using photolithography, magnetron sputtering deposition and lift-off technology, as shown in

Figure 3-14(c). After the electrode pattern was prepared, the sample was put into MPCVD chamber again for the second epitaxial growth, as shown in Figure 3-14(d). The secondary epitaxial growth condition is: CH_4/H_2=4%, total flow rate of reaction gas 500 sccm, substrate temperature 1000 ℃, pressure 13 kPa, thickness of epitaxial layer 500 nm. After the second growth, the surface was treated by UV-ozone for 30 minutes, and the hydrogen termination on the surface was transformed into oxygen termination, as shown in Figure 3-14(e). Finally, the other half of the interdigitated electrodes was fabricated on the secondary epitaxial layer using photolithography, magnetron sputtering and lift-off process, as shown in Figure 3-14(f). Then, a groove-shaped photovoltaic three-dimensional diamond UV photodetector was obtained, as shown in Figure 3-15. For comparison, we also fabricated photoconductive detectors on the same diamond.

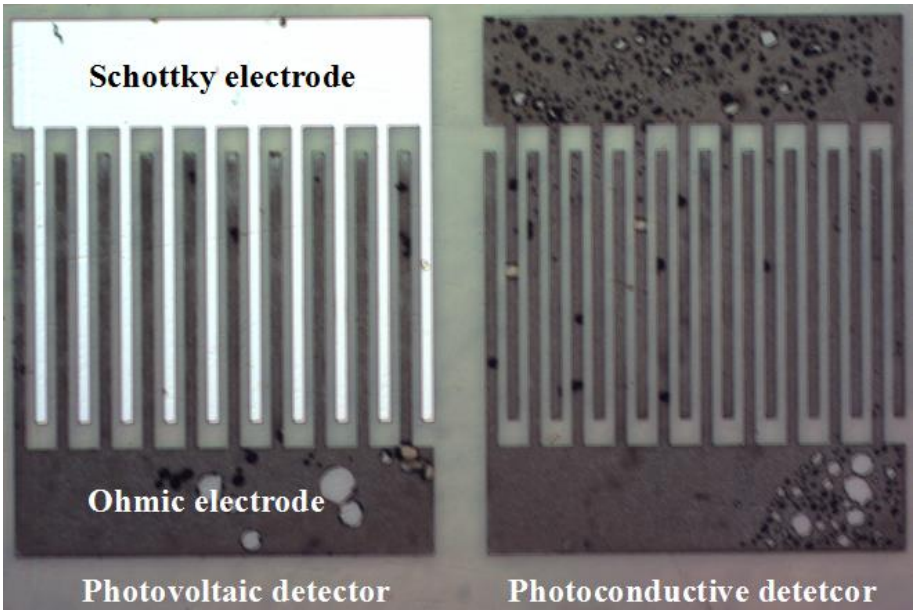

Figure 3-15 Optical image of photovoltaic detector and photoconductive detector.

Figure 3-16(a) gives the SEM image of the electrode structure of photovoltaic three-dimensional structure detector, in which the black area is secondary epitaxial diamond film, the white electrode is ohmic electrode, and the gray electrode is Schottky electrode. It can be seen that the electrode pattern is complete, which shows that the photovoltaic detector has been fabricated well. Figure 3-16(b) shows the interface between the metal region and the selective growth region after secondary epitaxial growth. The surface of secondary epitaxy diamond film is smooth, and the side wall is vertical and also smooth, which indicates that the optimization of selective growth process is successful. Compared with the smooth surface of diamond, the metal surface is rough and there are many particles. These

particles are formed by hydrogen plasma etching of tungsten metal during growth. In this study, tungsten thin films are relatively thick, so there is no diamond film grown on tungsten surface, only a few diamond nanoparticles are formed.

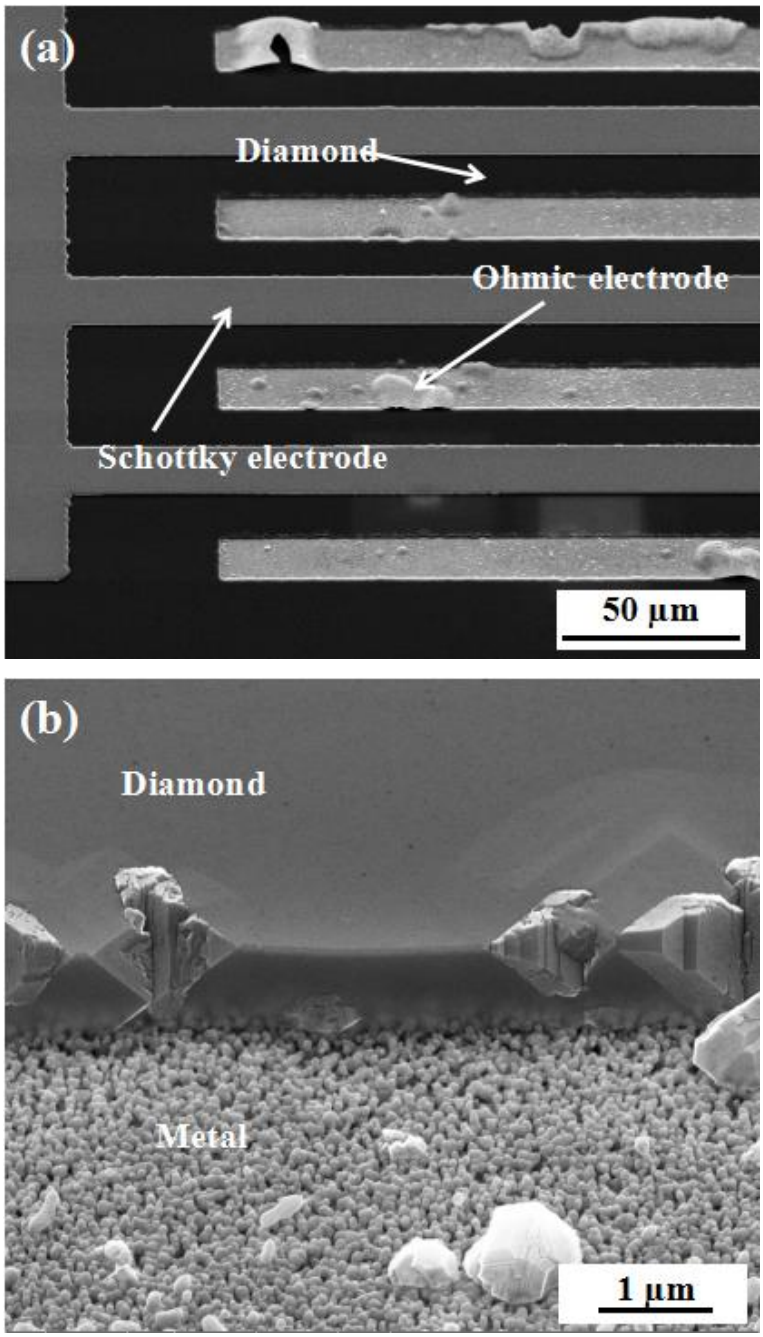

Figure 3-16 (a) SEM image of the three-dimensional photovoltaic detector. (b) A magnification of the interface between the metal region and the selective growth region.

Figure 3-17 shows the IV characteristics of the three-dimensional photovoltaic and photoconductive detectors in dark condition. The IV curve of the photoconductive detector is linear. The IV curve of the photovoltaic detector is different from that of the photoconductive

detector, which shows obvious rectification characteristics. Under positive voltage, the dark current of the device is very low, while under negative voltage, the dark current of the device is relatively small before the start voltage and increases rapidly after the start voltage. The dark current of photovoltaic detector under positive voltage is much smaller than that of photoconductive detector. At 10 V, the dark current of photoconductive detector is 2.37 A, while that of photovoltaic detector is only 14.2 pA, which reduces by five orders of magnitude. Therefore, the dark current can be effectively reduced by using photovoltaic devices. Under negative voltage, the dark current of photovoltaic detectors increases rapidly after opening, and finally approaches the dark current of photoconductive detectors.

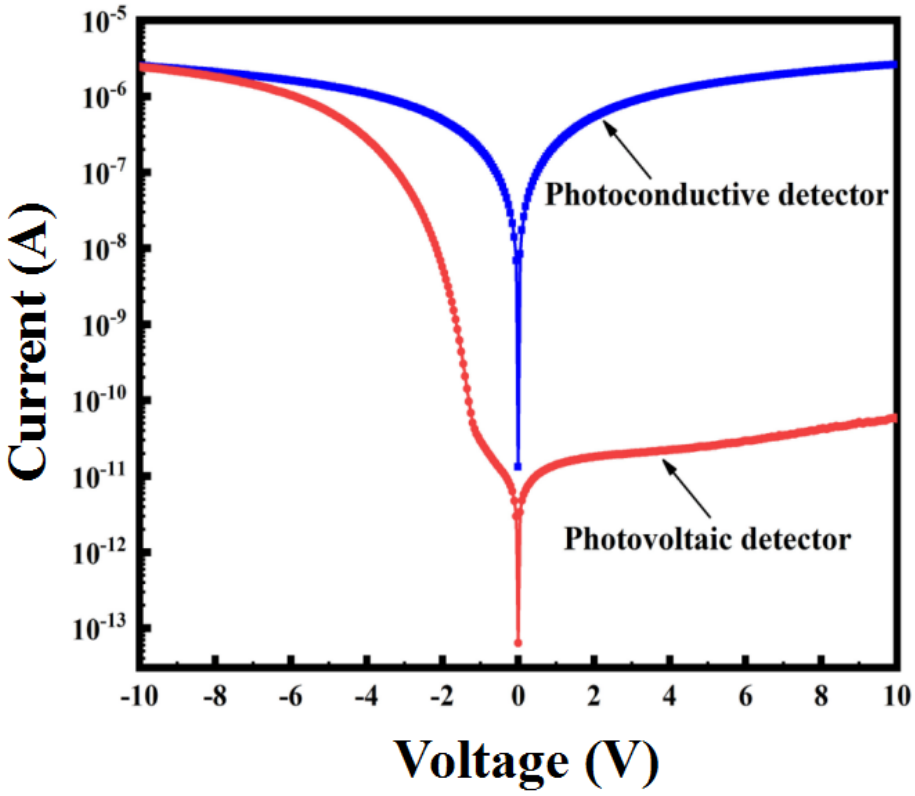

Figure 3-17 Dark IV characteristics of photovoltaic and photoconductive 3D UV detectors.

The photovoltaic detector is actually a Schottky photodiode, and it can be judged to be p-type through the IV curve. This indicates that acceptor doping exists in secondary epitaxial diamond. For Schottky diodes, the thermal electron emission model can be used to fit the IV curve, so as to extract the barrier height and ideal factor. Under the thermal electron emission model, the relationship between current and voltage is [63]:

$$I = AA^{*}T^{2}\, e^{\frac{-q\phi_B}{kT}}\, e^{\frac{q(V-IR_s)}{nkT}} \qquad (3\text{-}1)$$

where A is the effective area of the device (0.0019 cm^2), A* is the Richardson constant (84

$cm^{-2}K^{-2}$), V is the forward bias, T is the absolute temperature (300 K), q is the electron charge quantity (1.6×10^{-19} C), ϕ_B is the Schottky barrier height at 0 V, K is the Boltzmann constant (1.6×10^{-23} J/K), n is the ideal factor, and R_s is the series resistance. According to S.K. Cheung *et al*. [64], formula (3-1) can be rewritten by using current density J (J=I/A):

$$V = R_s AJ + n\phi_B + \frac{n}{\beta}\ln(\frac{J}{A^*T^2}) \quad (3\text{-}2)$$

In the formula, β=q/kT. Formula (3.2) with respect to J differential, then we get:

$$\frac{d(V)}{d(\ln J)} = R_s AJ + \frac{n}{\beta} \quad (3\text{-}3)$$

Therefore, dV/d (lnJ) is a linear function about J. The image of the function is a straight line, the slope is R_sA, and the intercept on the Y axis is n/β. From the value of the intercept, the ideal factor can be calculated. Define a function H (J) and satisfy the following relationship:

$$H(J) = V - \frac{n}{\beta}\ln(\frac{J}{A^*T^2}) = R_s AJ + n\phi_B \quad (3\text{-}4)$$

It can be seen that H (J) is also a linear function about J. Its function image is straight line, and the intercept between H (J) and Y axis is $n\phi_B$. The barrier height of Schottky electrode can be obtained by the intercept value and the calculated ideal factor n. Figure 3-18 (a) gives the function image of dV/d (lnJ) about J. Linear fitting of the data shows that the intercept is 0.128 V, so the value of n is calculated to be 4.95. Figure 3-18 (b) gives the function image of H (J) about J. Fitting the data, the intercept is 5.47 V, so the value of ϕ_B is 1.11 V.

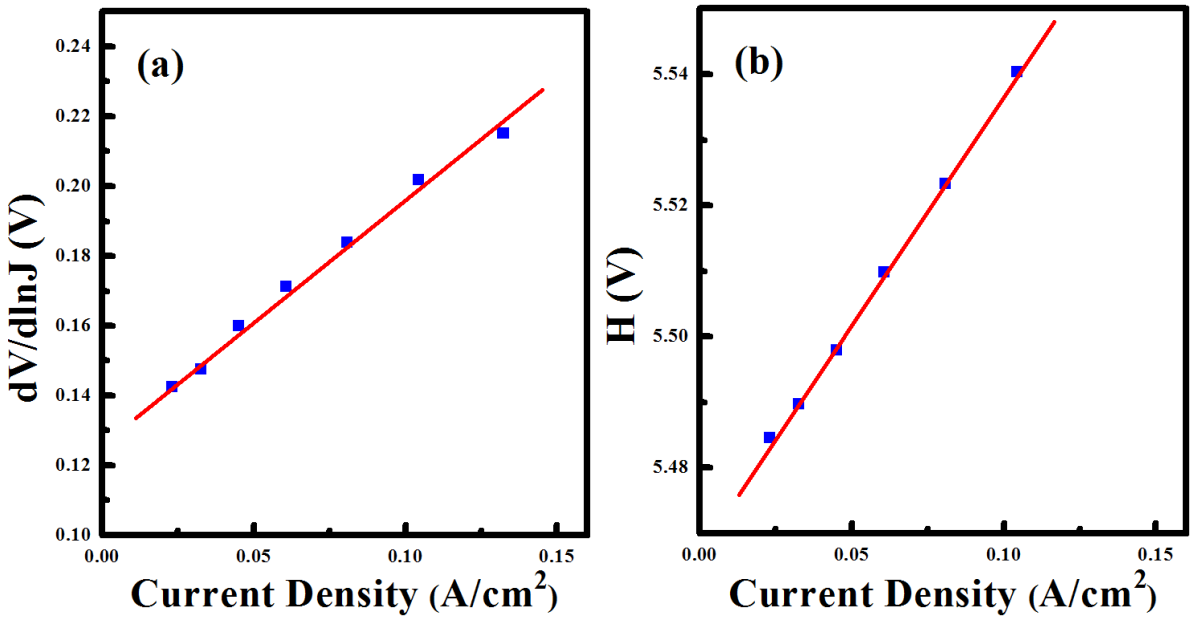

Figure 3-18 Analysis of Iv characteristics: (a) dV/dlnJ and (b) H vs current density.

Figure 3-19 shows the capacitance-voltage (C-V) characteristics of photovoltaic detectors. For Schottky diodes, the formula for calculating capacitance is $C=A\varepsilon_{diamond}\varepsilon_0/W$ [65]. In the formula, $\varepsilon_{diamond}$ is the relative dielectric constant of diamond with a value of 5.7, ε_0 is the vacuum dielectric constant 8.85×10^{-14} F/cm, and W is the width of the depletion zone. When the voltage is smaller than 0 V, the device is in the reverse bias state. With the increase of the reverse bias voltage, the width of the depletion zone will increase, so the capacitance value decreases monotonously. When the voltage is larger than 0 V, the device is in a positive bias state. With the increase of the positive bias voltage, the width of the depletion zone decreases, so the capacitance increases monotonously. When the positive bias voltage is greater than the open voltage, the diffusion capacitance gradually occupies the dominant position, and the capacitance value will decrease. According to the formula, the width of depletion zone at 0 V is calculated to be 4.31 μm.

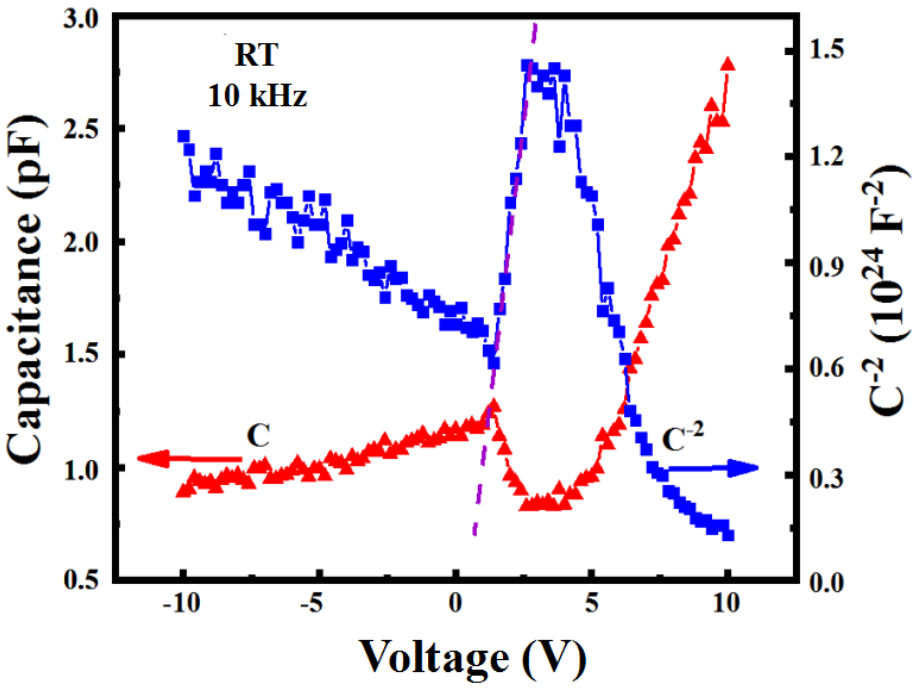

Figure 3-19 C-V characteristics of the photovoltaic detector at RT and 10 kHz.

Figure 3-19 also shows the C^{-2}-V curve. In the range of 1.5 V to 2.5 V, the C^{-2} increases linearly with the increase of voltage, indicating that the capacitance width in the depletion region decreases. The acceptor concentration of N_A in the selective grown diamond layer can be obtained by using the C^{-2}-V characteristics in this region. For Schottky diodes, the expression of capacitance in the depletion region is [66]:

$$\frac{1}{C^2}=\frac{2(V_0-V)}{q\varepsilon_{diamond}\varepsilon_0 N_A A^2} \qquad (3\text{-}5)$$

where V_0 is the intercept between the linear part of the C^{-2}-V curve fitting line (dotted line in Figure 3-19) and the V axis. From the expression (3-5), it can be seen that the slope of the fitting line is related to N_A:

$$\text{Slope} = \frac{2}{q\varepsilon_{diamond}\varepsilon_0 N_A A^2} \qquad (3\text{-}6)$$

Through linear fitting, the slope is 6.68×10^{23} F^{-2}/V, then the N_A is calculated to be 3.71×10^{13} cm^{-3}. The acceptor concentration is also the effective carrier concentration in the diamond film, which is much higher than the intrinsic carrier concentration, so the dark current of the detector is larger. The dark current can be effectively suppressed by using photovoltaic structure to make the device work in the reverse bias state, as shown in Figure 3-17.

Figure 3-20 shows IV characteristics of the photovoltaic detector at reverse bias under dark condition and 210 nm illumination. The reverse bias dark current is non-linear and saturated at a small voltage. When 210 nm light is applied, the photocurrent increases linearly with the increase of voltage. At 10 V, the photocurrent value is 24.1 pA, which is 17 times of the dark current. The light/dark current ratio of photoconductive detectors is only 9 at 10V, so photovoltaic detectors have higher light/dark current ratio.

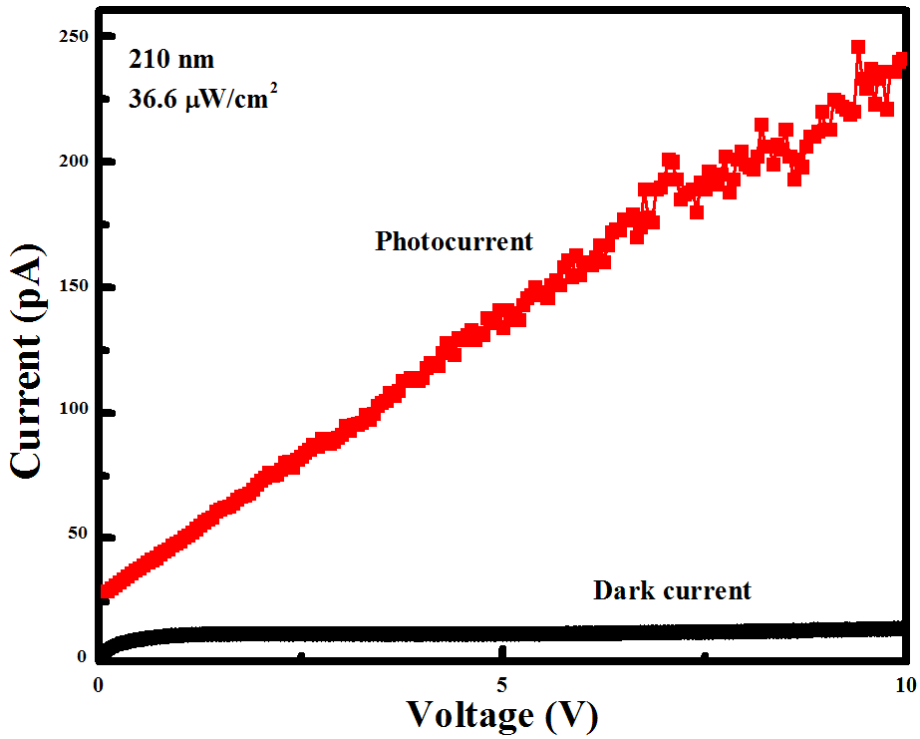

Figure 3-20 IV characteristics of the photovoltaic detector at reverse bias under dark condition and 210 nm illumination.

Figure 3-21 shows the spectral responsivity of the photovoltaic detector. It can be seen

that the device has obvious selectivity between UV and visible light. Under 10 V bias, the responsivity of the device reaches the maximum of 3.71 mA/W at 215 nm, and the 215 nm/400 nm UV/visible rejection ratio is 371. For photoconductive detectors, the 215 nm wavelength responsivity is 276 A/W at 10 V, and the 215-nm/400-nm UV/visible rejection ratio is 276. Thus, although the response of photovoltaic detectors is low, the rejection ratio of photovoltaic detectors is higher than that of photoconductive detectors. This is because the Schottky diode has a depletion region in the reverse bias state, which can inhibit impurity response.

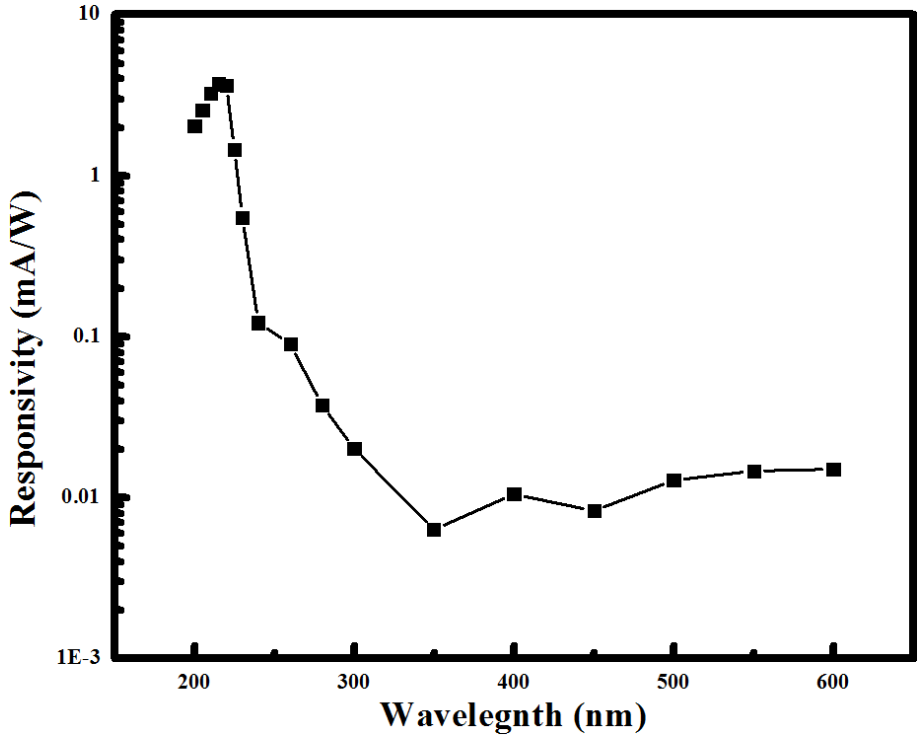

Figure 3-21 Spectral responsivity of the photovoltaic detector at 10 V.

Figure 3-22 shows the transient response of photovoltaic and photoconductive detectors under 5 V and 210 nm illumination. The rising time is the time needed for the detector current to rise from 10% to 90% of the stable value, and the falling time is the time needed for the detector current to decrease from 90% to 10% of the stable value. After removing the optical signal, the current of the photoconductive detector decreases rapidly and then slowly, and can not decrease to 10% of the maximum current within 10 seconds, indicating that the continuous photoconductivity phenomenon is serious. However, photovoltaic detectors are different. After removing the optical signal, the current value decreases rapidly, and the drop time is 590 ms. The results show that the photovoltaic structure is beneficial to suppress the persistent photoconductive effect of the device.

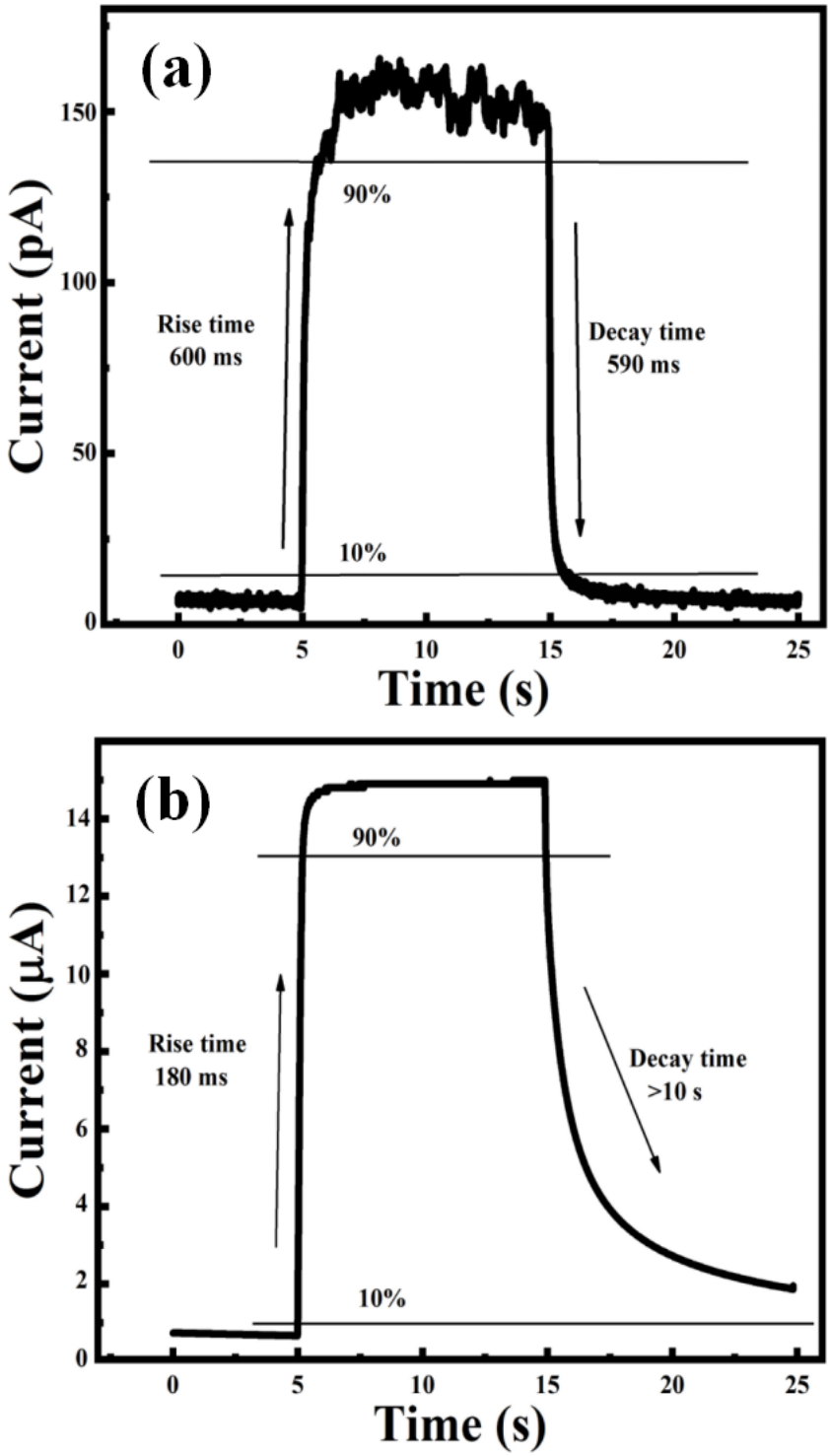

Figure 3-22 Transient response of (a) photovoltaic and (b) photoconductive detectors under 5 V and 210 nm illumination.

In a word, the photovoltaic structure can effectively reduce the dark current, improve the UV/visible light rejection ratio and shorten the decline time of the device in the bias state. Although the responsivity of the device is low, it can make the device work in a positive bias state without requiring fast response and only responsivity, so as to obtain a larger optical

response.

3.5 Summary

In this chapter, a bottom-up method for fabricating three-dimensional diamond grooved ultraviolet detectors is proposed for the first time. In the experiment, the metal interdigital electrode was fabricated on the surface of the diamond epitaxial layer, and then the grooved three-dimensional ultraviolet detector was obtained by selective growth in the diamond area which was not covered by metal. The detector is a photoconductive detector with dark current of 4.74 μA at 5V, responsivity of 9.36 A/W at 220 nm and UV/visible light rejection ratio of 10^3. To solve the problem of large dark current and slow response of the photoconductive detector, we fabricated photovoltaic three-dimensional ultraviolet detectors by bottom-up method. The dark current of the photoconductive detector is five orders of magnitude lower than that of the photoconductive detector, and the decay time is 590 ms, which is much shorter than the response time of the photoconductive detector.

4 Quasi-one-dimensional diamond UV photoetector

4.1 Introduction

The transmission of electrons in semiconductors mainly considers two characteristic lengths: the average free path of electrons (λ_{MFP}) and the diffusion length of electrons (λ_{DL}) [67]. The average free path of electrons is the average length of the free movement of electrons before collision. When the average free path of the electron is larger than the size of the medium through which the electron passes, the ballistic transport can be realized. When an electron changes its motion only when it collides with a medium boundary in a two-dimensional or one-dimensional material, the electron transport is considered to be one-dimensional (1D) or two-dimensional (2D), as shown in Figure 4-1.

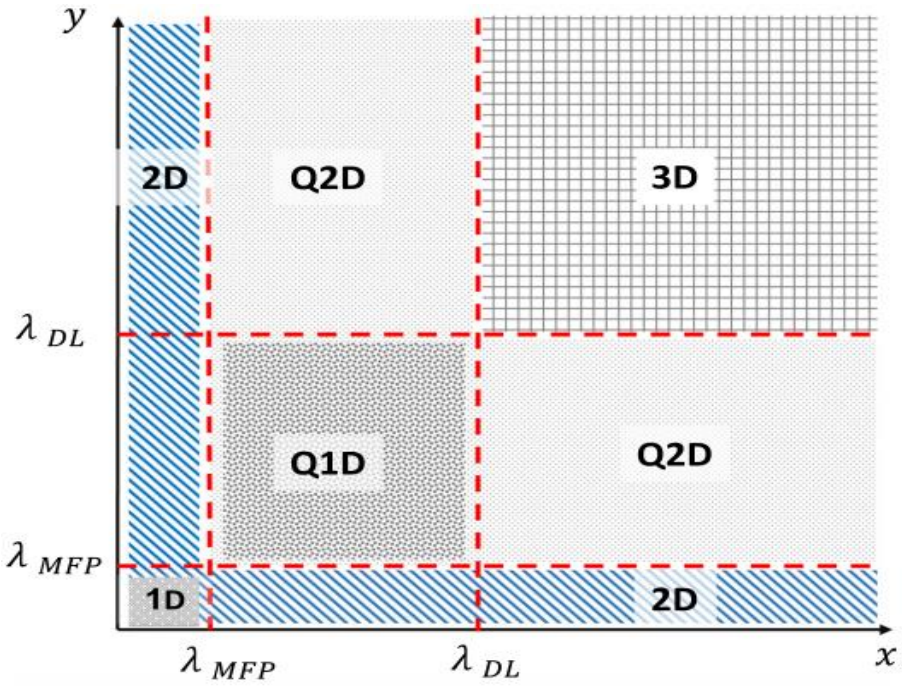

Figure 4-1 Carrier transport modes is related to material size [67].

The second characteristic length is the electron diffusion length, which is the average distance that the electron can move before recombining with the hole. When the electron diffusion length is larger than the size of the transmission medium, the motion of the electron changes when it collides with the boundary of the medium, resulting in anisotropic trajectories. Because of these collisions, electron transmission will be guided to an

unrestricted direction, and electrons can travel a long distance in that direction before recombination. When the size of the medium is smaller than the electron diffusion length in one direction, it is quasi-two-dimensional (Q2D) transport; when the size of the medium is smaller in two directions, it is quasi-one-dimensional (Q1D) transport. If the size of the medium is larger than the electron diffusion length, then the motion of electrons in the medium is not limited by the physical size, and it is a three-dimensional transport mode (3D).

In recent ten years, one-dimensional or quasi-one-dimensional structures have been widely studied in ultraviolet detectors. When the physical size decreases, besides the carrier transport changes, the material also has some unique optical, magnetic and mechanical characteristics. At present, many materials can be fabricated into one-dimensional nanowires, which can be applied to ultraviolet detectors, such as ZnO, Ga_2O_3, and TiO_2, greatly improving the responsivity of devices. However, for diamond, there are no reports of direct synthesis of nanowires, only by etching. Electron beam lithography is needed to fabricate diamond nanowires with high cost. On the contrary, its quasi-one-dimensional structure is relatively easy to realize.

The average electron free path is related to the momentum relaxation time (τ_m) and the average drift velocity (υ) $\lambda_{MFP}=\upsilon\tau_m$. Generally, the momentum relaxation time is about tens of femtoseconds [68,69], and the average drift velocity of CVD diamond is about 10^7 cm/s [70]. Therefore, λ_{MFP} is less than several nanometers. The length of diffused electron lambda λ_{DL} is related to diffusion coefficient (D_n) and electron lifetime (τ_n) [67]:

$$\lambda_{DL} = \sqrt{D_n \tau_n} = \sqrt{\frac{kT}{q} \mu_n \tau_n} \qquad (4\text{-}1)$$

For CVD single crystal diamond, the product of $\mu_n\tau_n$ is about 10^{-3} cm^2/V [71], then the calculated value of lambda λ_{DL} is about 50 μm. This means that the quasi-one-dimensional transmission of diamond materials can be realized on the μm scale.

In the research of three-dimensional structure diamond ultraviolet detectors with grooved electrodes, the size of materials is relatively large, and the X and Y directions are not limited by the size of materials, so the carrier transport belongs to three-dimensional transport. In this study, in order to realize Q1D transport, we changed the way of setting the electrodes to perpendicular to the diamond strip, as shown in Figure 4-2. In this way, the carrier movement in the side wall direction of the diamond strip is limited, and the movement of the upper surface and the lower interface is limited. Under the applied electric

field, the carrier can only travel along the direction of the diamond strip. When the size of diamond strip is very small, Q1D transportation can be realized.

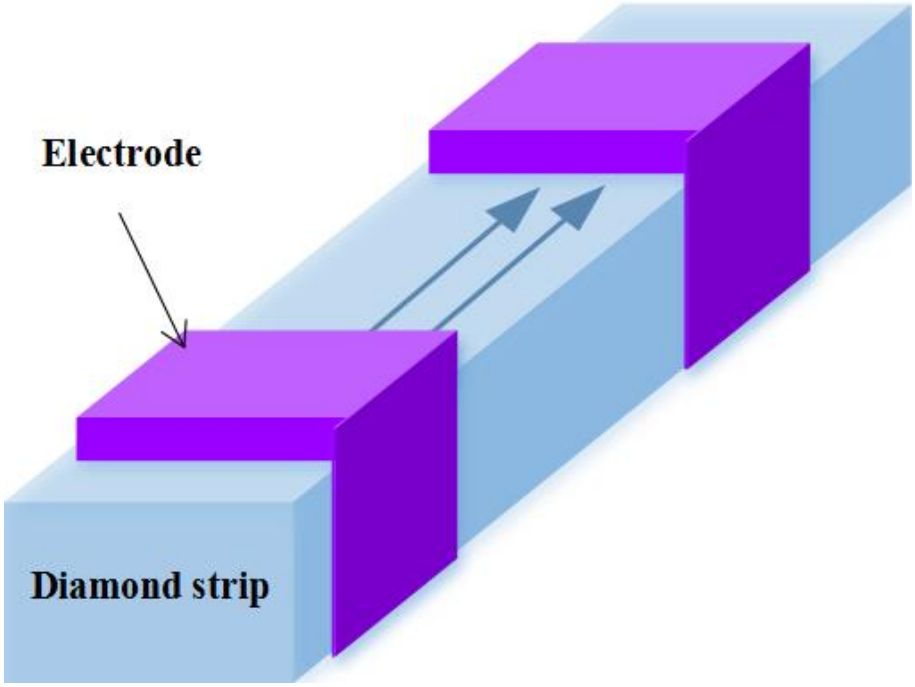

Figure 4-2 Diagram of quasi-one-dimensional design for diamond detector.

4.2 Effect of inductively coupled plasma etching on surface morphology

In the fabrication of Q1D structure detectors, etching technology is needed to fabricate diamond strips. Inductively coupled plasma (ICP) etching is a common used etching technology with many advantages. ICP has two RF sources, the upper RF source is used to excite plasma, and the lower RF source forms negative bias. In this case, the bias of the upper RF source can be increased to produce more plasma. In this way, the lower RF source can achieve a higher rate of etching even if the bias voltage is small. At the same time, due to the low bias of the lower RF source, the bombardment effect on the surface is smaller, and more chemical reactions occur, which makes the surface damage smaller. Therefore, this chapter uses ICP etching method to prepare diamond strips. The equipment used is RIE-200iP etching system of SAMCO Company in Japan, as shown in Figure 4-3.

Figure 4-3 ICP machine used in the experiment.

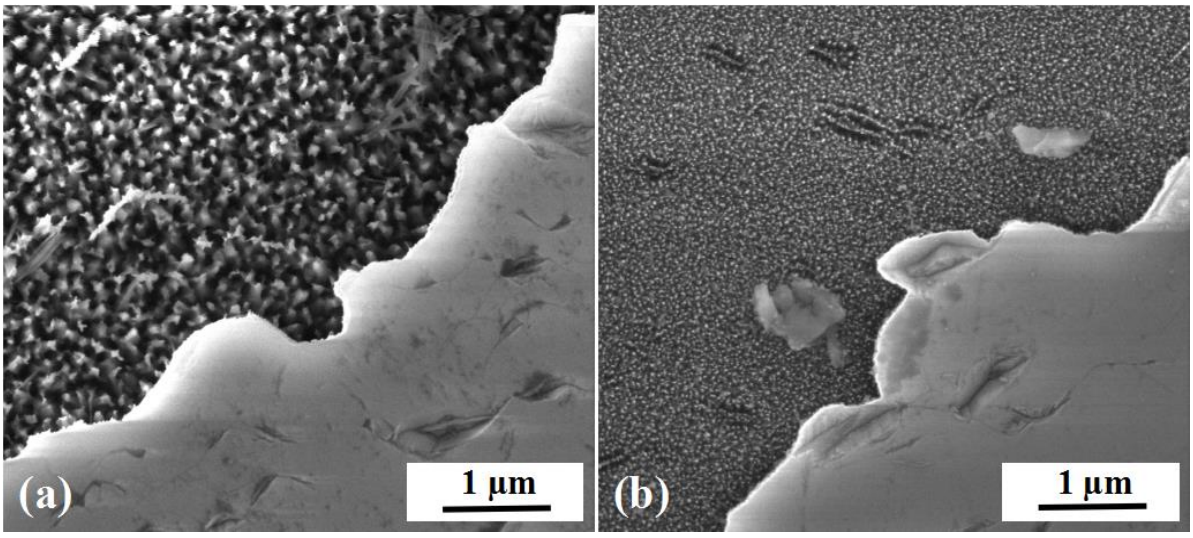

Figure 4-4 Diamond morphology after ICP etching with upper RF power of (a) 100 W and (b) 200W.

In order to obtain better a good etching surface, we optimize the ICP etching process. Firstly, the influence of the upper RF source is studied. In the experiment, the power of the lower RF source is 200 W, the oxygen flow rate is 90 sccm, the working pressure is 10 Pa, the power of the upper RF source is 100 W and 200 W, and the etching time is 30 min. Figure 4-5 shows the diamond morphology after ICP etching. It can be seen that the verticality of etched steps is very good under both conditions. However, the surface roughness of the two surfaces has changed. At 100 W, the diameter of the surface

nano-column after etching is small, but at 200 W, the diameter of the surface nano-column after etching is large. Therefore, 100 W power of upper RF source is suitable.

After selecting the power of the upper RF source, the power of the lower RF source is optimized. The diamond was etched for 30 minutes at 100 W power of the upper RF source, 90 sccm oxygen flow rate, 10 Pa working pressure and 100 W power of the lower RF source. Figure 4-5 shows the diamond morphology after ICP etching. It can be seen that compared with the diamond morphology etched by 200 W power of lower RF source (Figure 4-5a), the verticality of the step is worse, but the surface becomes smoother and the structure of nano-column is much less. Therefore, 100 W power is suitable for the lower RF source.

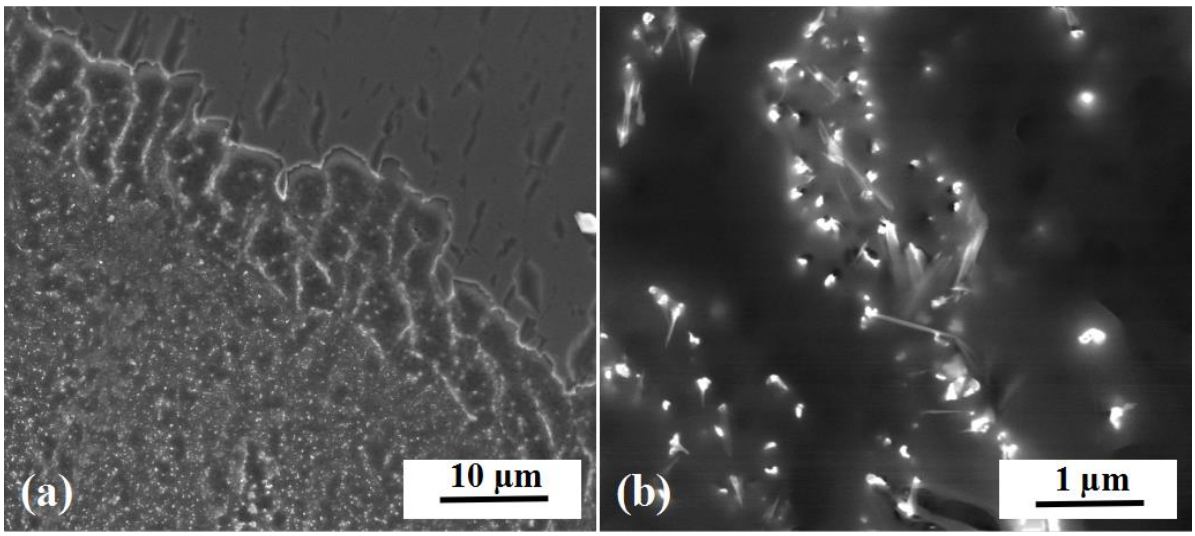

Figure 4-5 Diamond morphology after 100 W lower RF power etching.

In order to obtain good verticality, it is necessary to optimize the working pressure. The diamond was etched at working pressure of 6 Pa, 8 Pa, 10 Pa and 12 Pa for 30 minutes with 100 W power of the upper RF source, 90 sccm oxygen flow rate, and 100 W lower of the lower RF source. It can be seen that at 6 Pa and 10 Pa working pressure, the verticality of etching step is poor, and the step wall is rough. When the working pressure is 8 Pa and 12 Pa, the verticality of the step is better and the wall of the step is smooth. Although the step is smoother at 12 Pa, there are a lot of nanocones on the etched surface, while there are fewer nanocones at 8 Pa, so the working pressure of 8 Pa is more suitable.

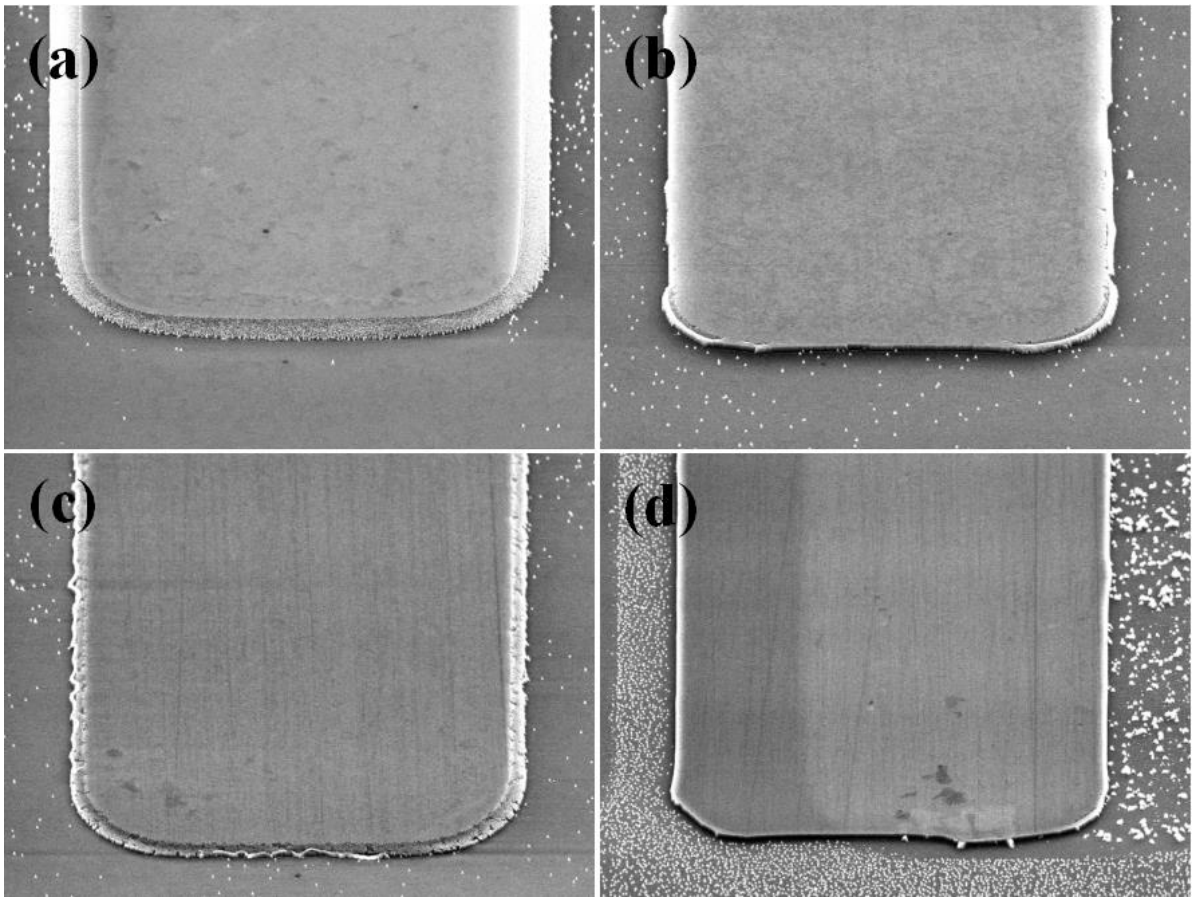

Figure 4-6 Morphology of diamond strip etched at different working pressure: (a) 6 Pa; (b) 8 Pa; (c) 10 Pa; (d) 12 Pa.

4.3 Q1D single crystal diamond UV photodetector without surface recovering

4.3.1 Experiment

With the optimized ICP etching process, Q1D single crystal diamond UV photodetectors can be fabricated and the fabrication process is shown in Figure 4-7. The substrate was 3 mm×3 mm×0.3 mm HPHT IIa-type (100) oriented single crystal diamond. After acid, alkali and organic cleaning, about 210 nm thick high quality single crystal diamond epitaxial layer was grown on the substrate through MPCVD method, as shown in Figure 4-7(b). The parameters of the epitaxial growth were as follows: the total flow rate of reaction gas is 500 sccm, the ratio of CH_4 to H_2 is 1%, the process pressure, growth temperature and microwave power are 13 kPa, 900 ℃ and 1 kW, respectively. After the growth, the diamond samples were heated for 1 hour at 250 ℃ in the sulfuric acid/nitric acid mixture to remove the hydrogen termination on the surface. Next, titanium strip arrays were prepared on the

epitaxial layer surface as masks by using photolithography, magnetron sputtering and lift-off technology, as shown in Figure 4-7(c). The width of titanium strip is 10 μm, the spacing is 5 μm and the thickness is 100 nm.

After the mask pattern is prepared, the surface of diamond epitaxial layer was etched by ICP, as shown in Figure 4-7(d). The process parameters of ICP are as follows: the power of the upper RF source is 100 W, the power of the lower RF source is 100 W, the oxygen flow rate is 90 sccm, the working pressure is 8 Pa, and the etching depth is about 200 nm. After etching, titanium masks were removed by 15% hydrofluoric acid. After removing the mask, the sample is cleaned and the diamond strip array is obtained, as shown in Figure 4-7(e). The diamond strip has a width of 10 μm and a thickness of 200 nm. Its size is between the electron diffusion length and the average electron free path of diamond. In this case, one-dimensional electron transport along diamond strips can be realized. Finally, Q1D UV photodetectors were fabricated by setting electrodes in the direction perpendicular to the diamond strip through photolithography, electron beam evaporation coating and lift-off technology, as shown in Figure 4-7(f). The electrode material is Ti/Au with a thickness of 30/120 nm and a width of 5 μm. In this experiment, a number of electrode spacing are set up, which are 10 μm, 20 μm and 30 μm respectively. Meanwhile, planar structure detectors with the same electrode spacing were prepared on the same sample for comparison.

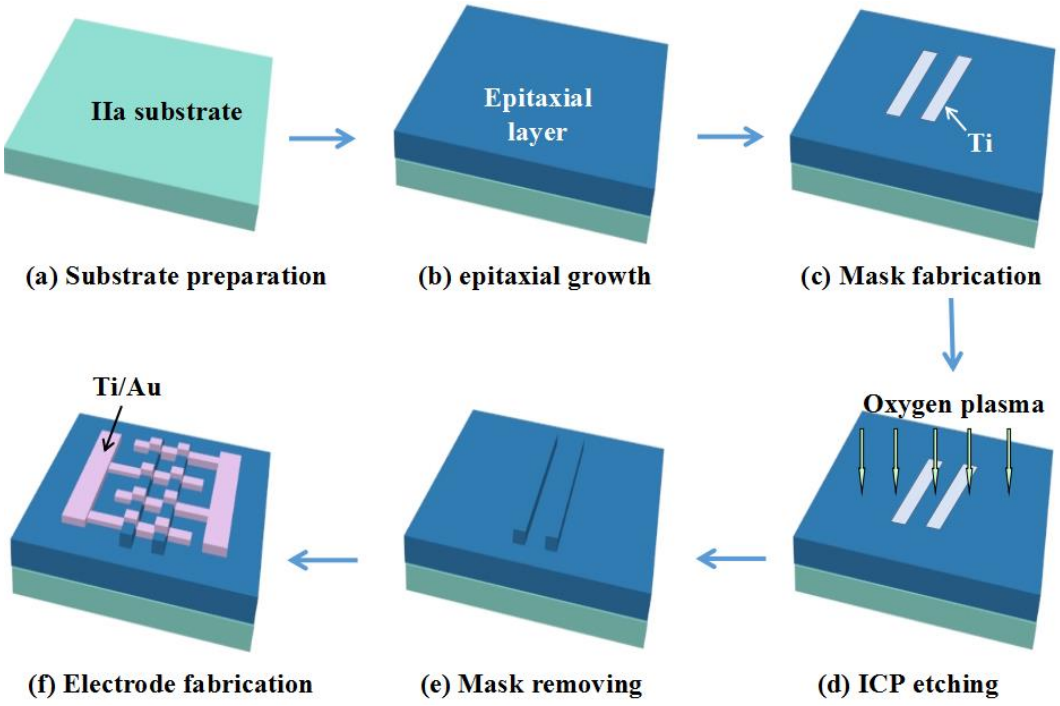

Figure 4-7 Fabrication process of the Q1D diamond UV photodetector

After the fabrication of the device, we observed its surface morphology by optical

microscopy and SEM to determine whether the Q1D structure was successfully fabricated. The photoelectric performance of the device was tested by Agilent B1505A power device analyzer. The incident light is 1000 W Xe light which is divided into monochrome light by a monochrometer. The optical power of incident light is measured by commercial ultraviolet enhanced silicon detectors.

4.3.2 Results and discussions

Figure 4-8 shows the photo of a quasi-one-dimensional structure detector with an electrode spacing of 10 μm. In the figure, the white strip is Ti/Au electrode, the black strip is ICP etched groove, the gray strip between the black strip is diamond strip, and the metal strip is orthogonal to the diamond strip. It can be seen that the diamond strips are parallel to each other and the boundary is clear, which indicates that ICP etching transfers the mask pattern to the diamond well. The metal electrodes are also very complete, indicating that the preparation process is very mature.

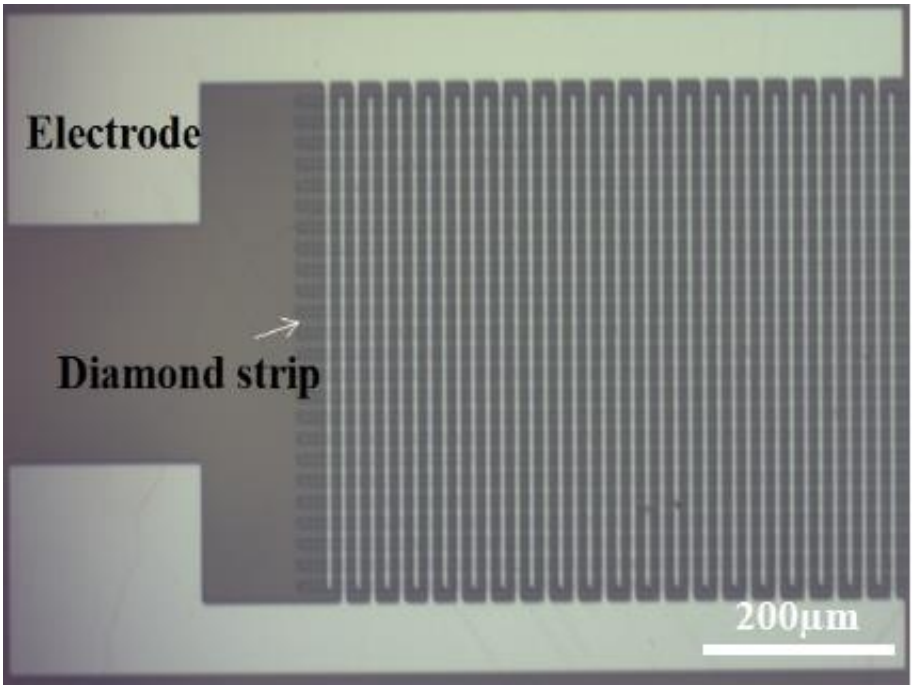

Figure 4-8 Optical image of a Q1D diamond UV photodetector with 10 μm electrode space.

Figure 4-9 shows the SEM image of a Q1D diamond UV photodetector with 20 μm electrode space. The white strip in the horizontal direction is the metal electrode strip, and the gray strip in the vertical direction is the diamond strip. It can be seen that the electrodes and diamond bars intersect vertically, similar to those observed in optical photographs. The side wall of the electrode strip is very vertical, and many contour boundaries are not observed. The grooves between the diamond strips are etched by ICP. The surface of the

grooves is very smooth and there are only a few nano-cone structures, which indicates that the optimized ICP process can be well applied to the structural etching of diamond.

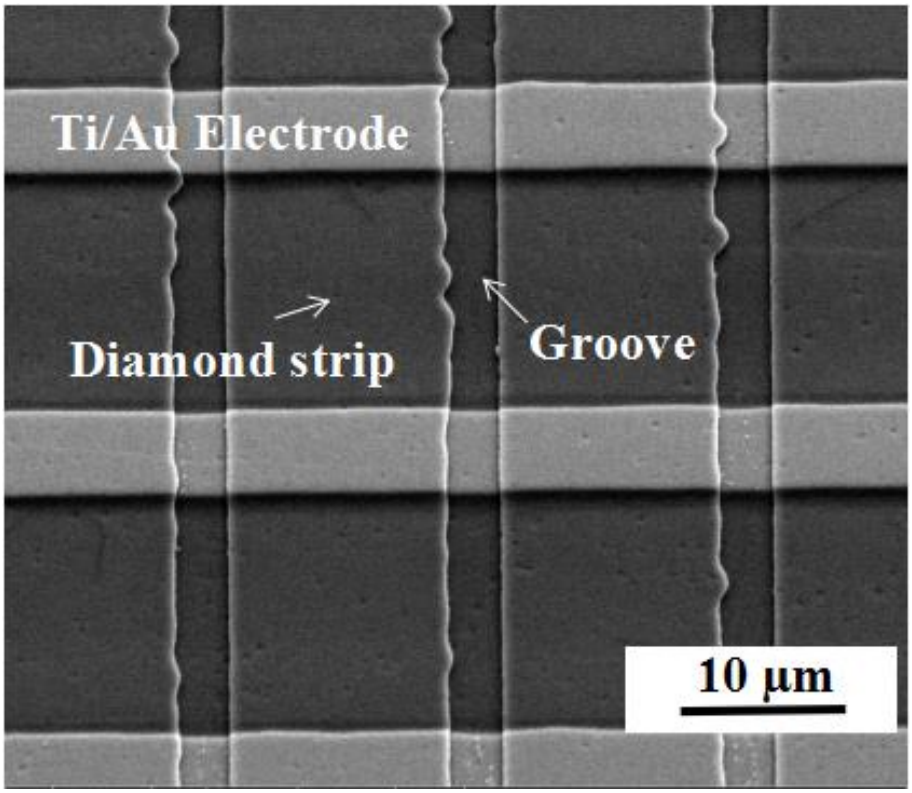

Figure 4-9 SEM image of a Q1D diamond UV photodetector with 20 μm electrode space.

Figure 4-10 shows the dark current characteristics of planar and Q1D detectors with different electrode space. For planar detectors, the dark current is very low, less than 200 fA at 5 V, and the value of dark current has little relationship with the distance between electrodes. This is because the intrinsic diamond resistivity is very large, even if the electrode space is only 10 μm, the resistance is still very large, so the dark current will be very low. In this test, the value of dark current is close to the detection limit of the instrument, so when the distance between electrodes increases, the accurate value of current can not be measured effectively. Compared with planar structure detector, the dark current of Q1D structure detector is larger, but it is still very small. At 5 V, the maximum dark current is less than 2 pA. The dark current of Q1D detector is related to the distance between electrodes. The maximum dark current is at 10-μm distance and the smallest is at 30-μm distance. The change of dark current of Q1D detector indicates that ICP etching introduces some surface states or defects on the surface, which generate additional surface conductance, thus increasing the dark current of the device. Assuming that the surface conductivity is constant, the resistance increases with the increase of electrode space, so the dark current decreases

with the increase of electrode space.

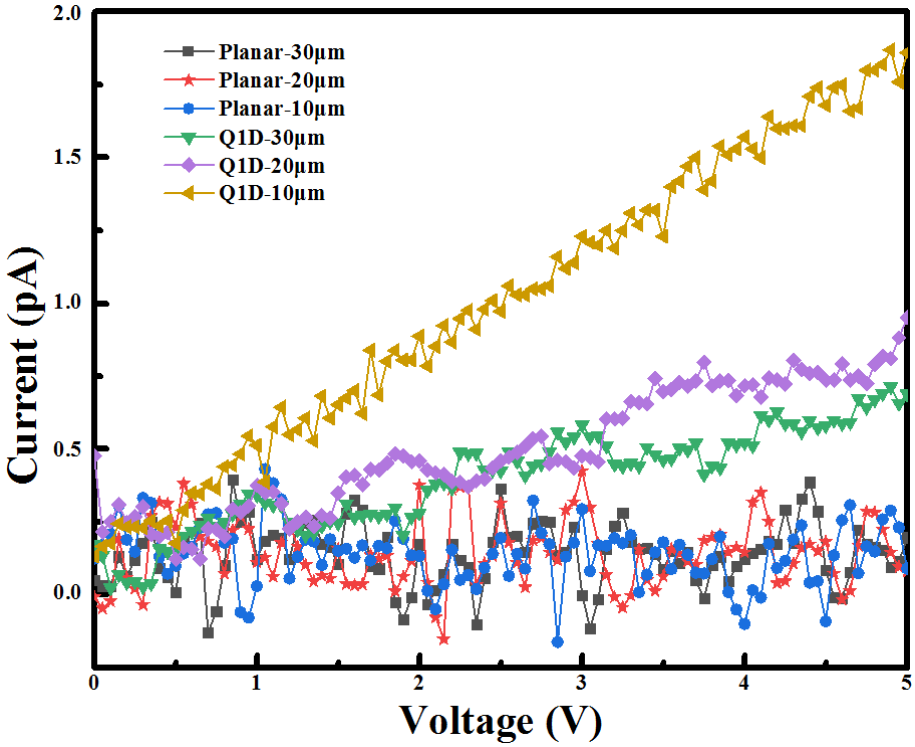

Figure 4-10 IV characteristics of Q1D and planar detectors in dark condition with different electrode space.

Figure 4-11 shows the IV characteristics of Q1D and planar detectors under 210 nm illumination at different space. The photocurrent of planar or Q1D detectors at 210 nm wavelength is much larger than that of dark current, which indicates that the detectors have good photoresponse performance. For planar detectors, the photocurrent at 20 μm space is the largest. The photocurrent of Q1D detectors increases with the increase of electrode space. This is because the carrier of Q1D detector is limited to transport along the direction of diamond strip. With the increase of electrode space, the area of photosensitive region increases, which makes the photoelectric current of the device larger. Carrier transport of planar detectors is not limited, and the probability of carrier recombination before being collected by electrodes is higher, especially when the distance between electrodes is larger, so the photocurrent at 30 μm distance is less than that at 20 μm distance. Another reason is the difference of electric field intensity. At the same voltage, the electric field intensity between the electrodes of the detector with 30 μm space is less than that of the detector with 20 μm space, which also results in low photocurrent.

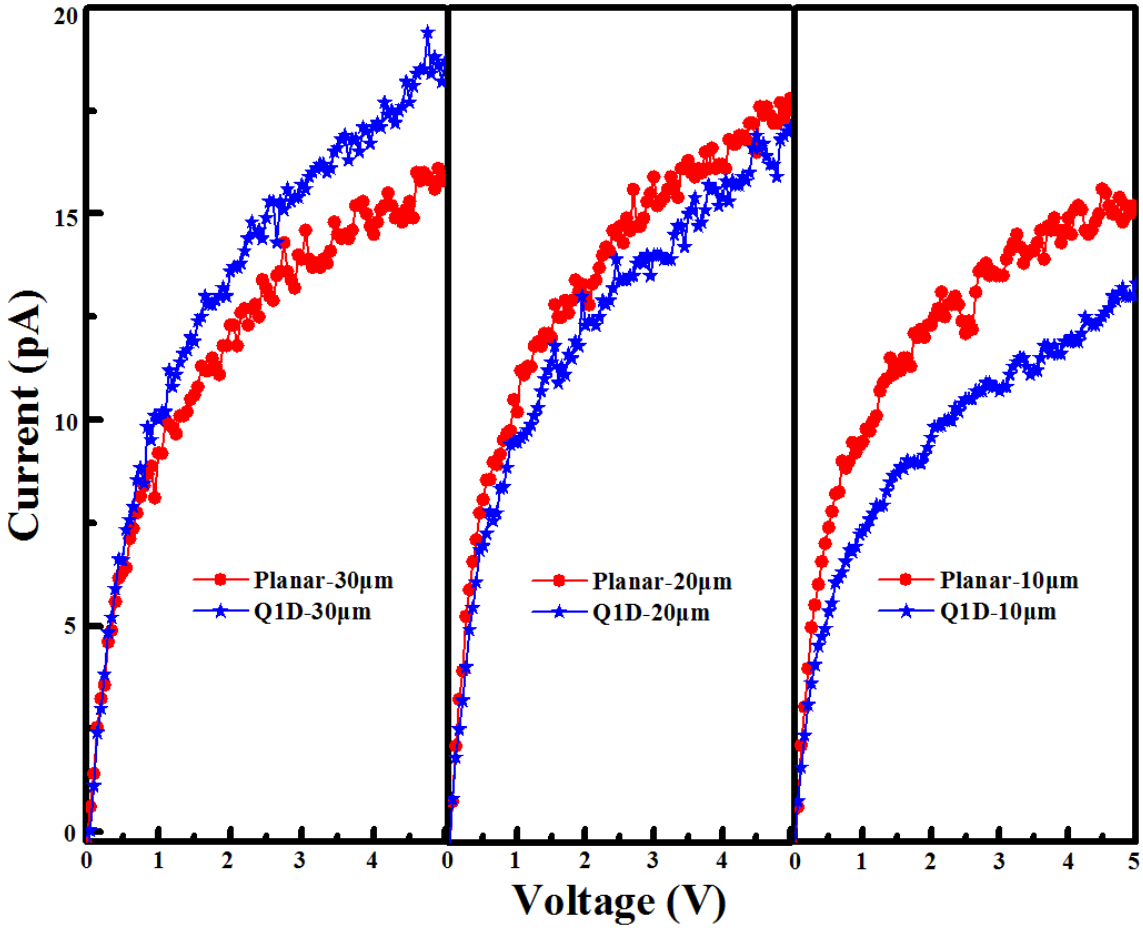

Figure 4-11 IV characteristics of Q1D and planar detectors under 210 nm illumination at different electrode space.

It also can be observed that the photocurrent of Q1D detector is lower than that of planar detector when the distance between electrodes is 10 μm and 20 μm, and the photocurrent of Q1D detector is higher than that of planar detector when the distance between electrodes is 30 μm. This is due to the balance between surface defect recombination and the increase of effective area in the photosensitive region. Surface defects trap photo-generated carriers and cause the decrease of photocurrent. The increase of the effective area of the photosensitive region results in more carriers and improves the photocurrent of the device. When the space is small, the increasing effect of carriers in the photosensitive region is weaker than the decreasing effect of carrier trapped by surface defects, so the photoelectric current of Q1D detector is lower than that of planar detector. However, with the increase of the space, the effective area of the photosensitive region increases, and the carrier increasing effect becomes stronger, which will reduce the gap between the photocurrent of the Q1D detector and the planar detector, so the gap between the photocurrent of the Q1D detector and the planar detector will decrease at 20 μm space. When the carrier increasing effect in the

photosensitive region exceeds the surface capture carrier decreasing effect, the photoelectric current of the Q1D detector will exceed that of the planar detector. This shows that the Q1D can improve the collection ability of photo-generated carriers at a larger electrode space. In addition, it should be noted that the effective photosensitive volume of Q1D detector is smaller than that of planar detector due to etching grooves, which means that the number of photo-generated carriers is lower than that of planar detector. However, the photocurrent of the Q1D detector can still exceed that of the planar detector, which further proves that the photonic carrier collection ability of the Q1D detector is better than that of the planar detector.

Table 4-1 gives the light to dark current ratio and net photocurrent values of Q1D structure detector and planar structure detector at 5V. It can be seen that the planar structure detector has the highest net current at 20 μm space and the maximum light-dark current ratio, while the Q1D structure detector has the highest net current and light-dark current ratio at 30 μm space. The light to dark current ratio of planar structure detectors is higher than that of Q1D structure detectors, which is due to the high dark current and low photocurrent caused by surface defects.

Table 4-1 Comparison of Q1D and planar detectors under 5V.

Sample	Dark current (pA)	210 nm current (pA)	210 nm/dark current ratio	Net current (pA)
Planar-10 μm	0.14	15.1	107.8	14.96
Planar-20 μm	0.15	17.8	118.7	17.65
Planar-30 μm	0.15	15.9	106	15.75
Q1D-10 μm	1.86	13.3	7.2	11.44
Q1D-20 μm	0.95	17.1	18	16.15
Q1D-30 μm	0.69	18.7	27.1	18.01

Figure 4-12 shows the curves of net photocurrent with electric field for Q1D structure detector and planar structure detector. The electric field intensity is simply obtained by dividing the bias voltage by the distance between the electrodes. Under the same electric field intensity, the net photocurrent of Q1D detector still increases with the increase of electrode space, and the net photocurrent of planar structure detector basically compounds this rule. The responsivity of the detector is obtained by dividing the net photocurrent by the optical power, so the responsivity of the detector with Q1D detector at 30 μm space is the

largest. This shows that the Q1D structure can improve the responsivity of the device.

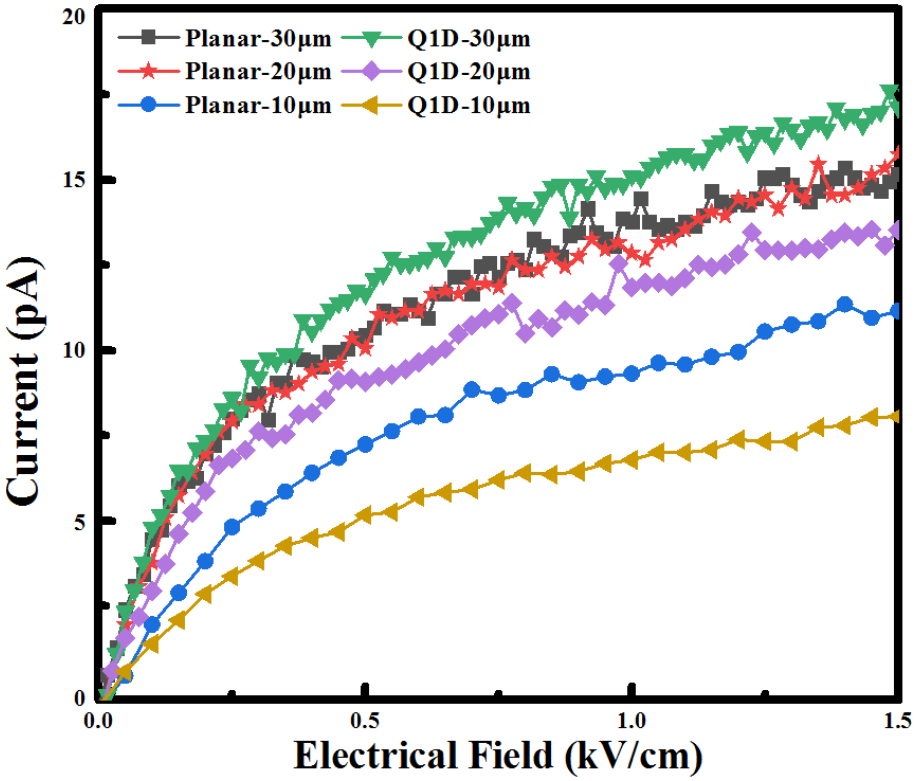

Figure 4-12 shows the curves of net photocurrent with electric field for Q1D structure detector and planar structure detector.

4.4 Q1D single crystal diamond UV photodetector with surface recovering

The large dark current of as-fabricated Q1D detector can be attributed to surface defects induced in ICP process, which could further affect the photoelectric response performance of devices. In order to solve this problem, we use MPCVD method to repair defects.

At first, the as-fabricated detectors were heated for 30 minutes at 80 ℃ in aqua regia to remove Ti/Au electrodes. Then, the diamond sample was heated for 2 hours at 250 ℃ in acid solution with 1:1 volume ratio of sulfuric acid and nitric acid to remove non-diamond compounds on the surface. Next, a 30 nm thick diamond epitaxial layer was grown by MPCVD method on the strip side. The growth conditions were as follows: the total flow rate is 500 sccm, the ratio of CH_4 to H_2 is 1%, the process pressure, growth temperature and microwave power are 100 Torr, 900 ℃ and 1 kW, respectively. After growth, the diamond sample was heated for 1 h at 260 ℃ in a 1:1 volume ratio mixture of sulfuric acid and nitric acid to remove the surface hydrogen terminal. Lastly, Q1D detectors were fabricated on the

surface again with the same electrode parameters as that of as-fabricated Q1D detectors. Meanwhile, planar detectors with the same electrode space were prepared for comparison.

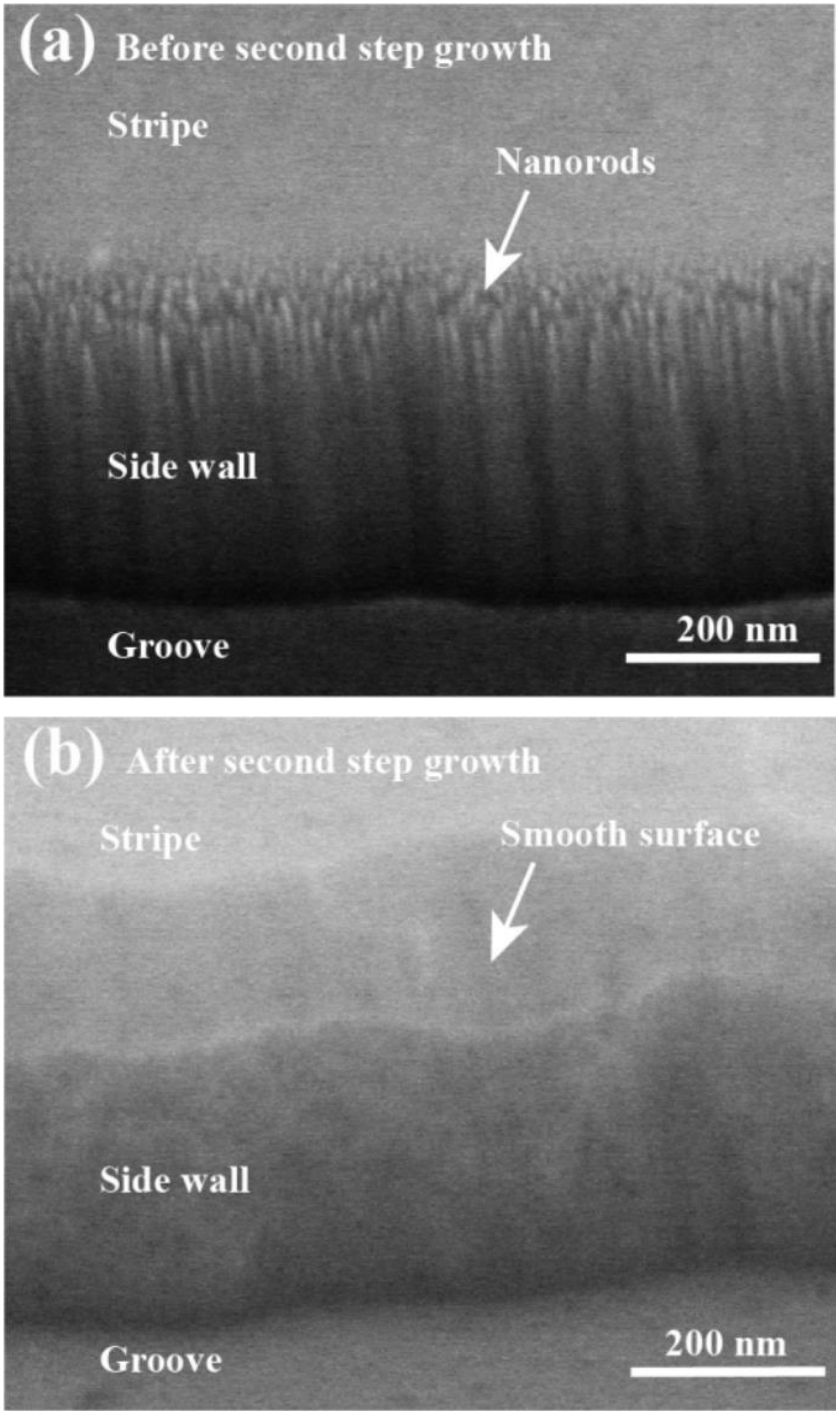

Figure 4-13 SEM images of the structured strips (a) before and (b) after recovering growth.

Figure 4-13 shows the SEM images of diamond strips before and after second step growth. Before second step, although the steps have good verticality, there are nano-column structures on the wall of the steps, as shown in Figure 4-13(a). This may be due to the thin edge of the metal mask, or even the appearance of holes. In the ICP etching process, the thin

edge metal will be etched first, and then the step will be etched further. It is also possible that the plasma etches the steps through the holes in the edge metal film to form nano-clusters. After second step, it can be observed that the surface of diamond becomes very smooth, as shown in Figure 4-13(b). The nano-pillar structure was placed by continuous smooth diamond film, which proved that the second step growth has successfully recovered the surface defects.

Figure 4-14 shows the test results of the step profiler. It can be observed that the verticality of the step was better before the recovering growth, but there was a turning point at the intersection of the step and the groove, which was caused by the different etching rates of the groove and the edge of the step. In addition, the curve in the groove area is not smooth and zigzag. Each turning point corresponds to a small bump on the surface, and there may be a nanoparticle, which is consistent with the surface morphology observed in the SEM image. After recovering growth, the verticality of the steps decreases slightly, and the edges of the surfaces and steps are no longer sudden changes, but slow transitions. This is the result of both vertical and lateral epitaxy growth of the surface. At the junction between the bottom of the step and the groove, the turning point disappears, indicating that the vertical direction of the step wall becomes more continuous and smooth. In the groove area, the contour curve is smooth and the shape of zigzag can not be observed, which indicates that the groove surface defect has been repaired successfully.

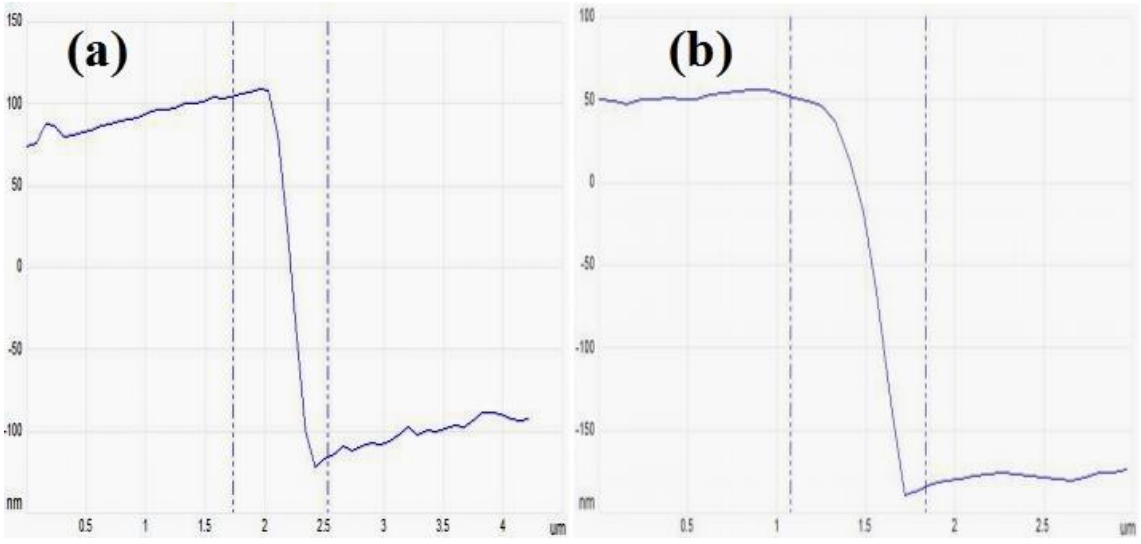

Figure 4-14 Stepped profile test (a) before and (b) after recovering growth.

Figure 4-15 shows the IV characteristics of Q1D and planar detectors in dark environment after the second step growth. The dark current of planar detector is very low, less than 300 fA at 5V, and the shaking range of dark current curve is basically the same at different electrode

space. The dark current of Q1D detectors decreased a lot compared with that of as-fabricated Q1D detector. The dark current of 10 μm, 20 μm and 30 μm space as-fabricated detectors at 5V was 1.86 pA, 0.95 pA and 0.69 pA, respectively. After second growth, the dark current of Q1D detectors decreased to 0.35 pA, 0.25 pA and 0.2 pA, with a maximum reduction of six times. This indicates that the surface defect has been repaired successfully, so the dark current decreases. It is noteworthy that the dark current of Q1D detectors is reduced to the same level as that of planar detectors. This further proves that surface defects are repaired during second epitaxial growth. Unlike planar detectors, the dark current of Q1D detectors is still related to the distance between the electrodes, increasing with the decrease of electrode space. This indicates that the Q1D device design brings different properties.

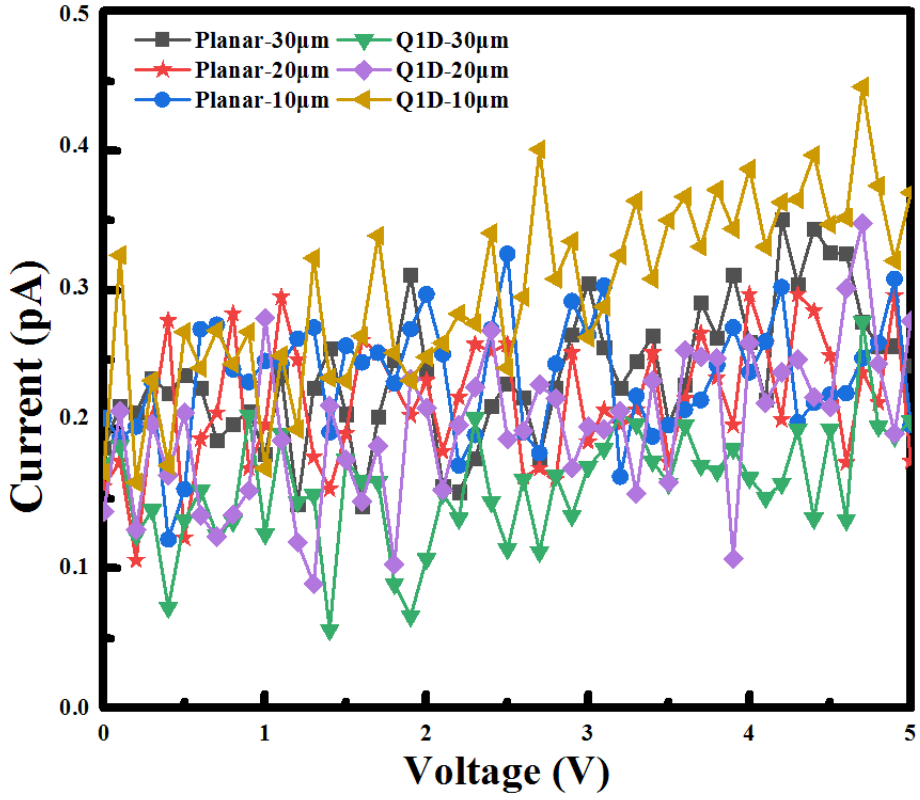

Figure 4-15 Dark IV characteristics of Q1D and planar detectors after recovering growth.

Fig. 4-16 shows the IV characteristics of Q1D and planar detectors under 210 nm wavelength illumination at different space after second step growth. The photocurrent of planar or Q1D detectors at 210 nm wavelength is much larger than dark current, which indicates that the detectors have good photoresponse performance. For planar detectors, the photoelectric current at 20 μm space is the smallest, which is different from that before second step growth. The current of Q1D detector is similar to that before second step growth, and its photocurrent increases with the increase of electrode space. From the characteristics

of photocurrent IV, it can be observed that the photocurrent of Q1D detector is larger than that of planar detector when the distance between electrodes is 10 μm, 20 μm and 30 μm, and the minimum photocurrent of Q1D detector is larger than that of planar detector. The results show that surface defect repair plays an important role in improving the performance of Q1D detector. After surface defect repair, the photo-generated carriers are no longer captured, so the collected photo-generated carriers increase. Because of the unique design of Q1D, the photoelectric gain of the device can be improved, so the photoelectric current of Q1D detector is much larger than that of planar detector. It should be noted that the effective photosensitive volume of Q1D detector is smaller than that of planar detector, which means that the number of photo-generated carriers is lower than that of planar detector. However, the photocurrent of the Q1D detector can still exceed that of the planar detector, which further proves that the photo-generated carrier collection ability of the Q1D detector is better than that of the planar detector.

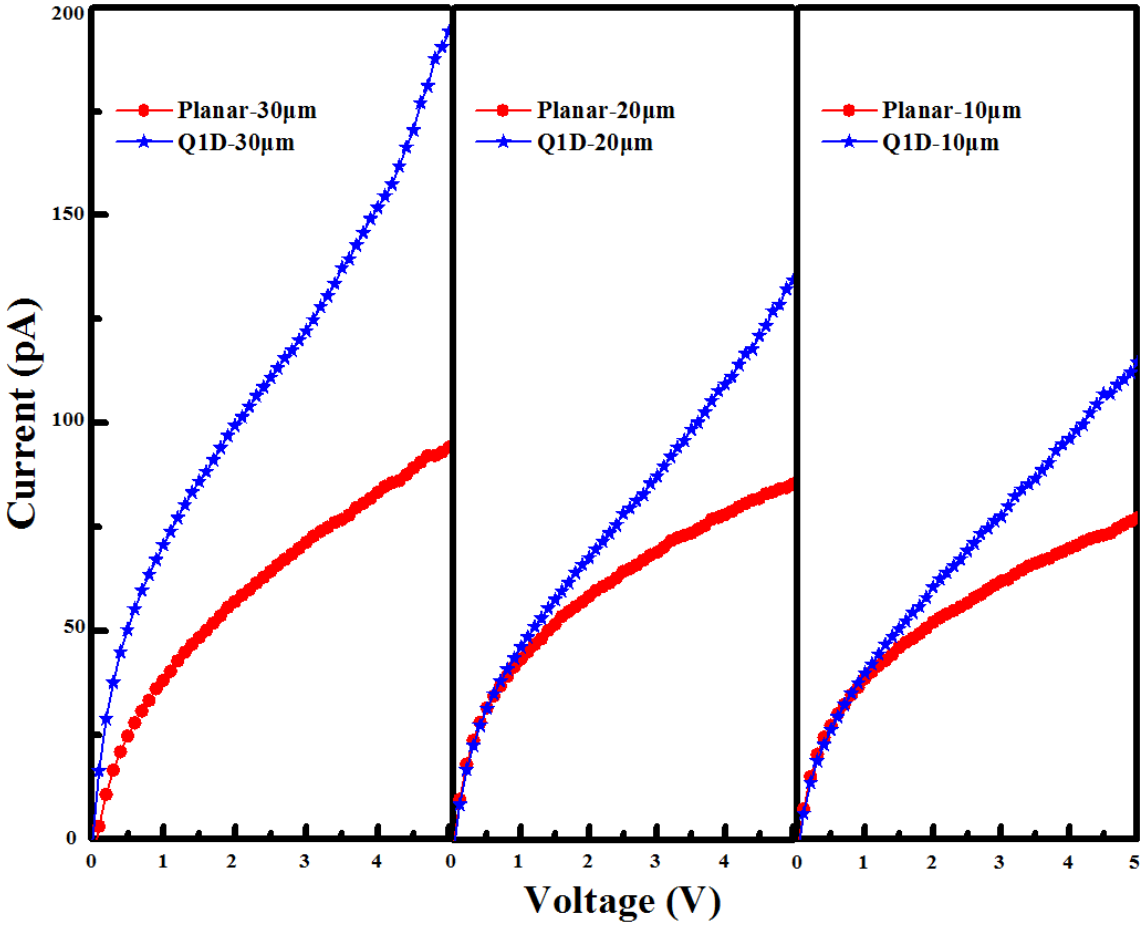

Figure 4-16 IV characteristics of Q1D and planar detectors under 210 nm light illumination at different space after second step growth.

Table 4-2 shows the current comparison between the quasi-one-dimensional structure

detector and the planar structure detector after repair growth at 5V. Before repair growth, the maximum dark current of quasi-one-dimensional structure detector is only 27, which is much smaller than that of planar structure. After repair and growth, the light-dark current ratio reached 971, which was 36 times higher than that. At the same time, the light-dark current ratio of quasi-one-dimensional structure detector is also higher than that of planar structure detector, which proves that repair growth has a significant effect on improving device performance. In addition, the maximum net photocurrent of quasi-one-dimensional structure detector is twice that of planar structure detector, which indicates that quasi-one-dimensional structure is beneficial to improve the photoelectric response performance of the device.

Table 4-2 Comparison of Q1D and planar detectors under 5V after recovering growth.

Sample	Dark current (pA)	210 nm current (pA)	210 nm/dark current ratio	Net current (pA)
Planar-10 μm	0.22	85.4	388.2	85.18
Planar-20 μm	0.22	77.2	350.9	76.98
Planar-30 μm	0.22	94.2	428.2	93.98
Q1D-10 μm	0.35	114.6	327.4	114.25
Q1D-20 μm	0.25	134.4	537.6	134.15
Q1D-30 μm	0.20	194.2	971.0	194.00

It is noteworthy that the photocurrent of Q1D detectors or planar detectors after second growth is much larger than that before second growth. This is because non-etched surfaces have also been repaired. For UV photodetectors, clean material surface has a crucial impact on the performance of the detector, because UV light penetration depth is relatively shallow, most carriers are located near the surface. If the material surface is contaminated, it will produce a large surface recombination rate, which will reduce the number of photo-generated carriers collected by the device. During the preparation of diamond strips, Ti metal acts as a mask and deposits on the surface of diamond. In ICP etching process, plasma not only bombards Ti, but also heats it, so that chemical reaction or diffusion may occur at the interface between metal and diamond, which affects the cleanliness of diamond surface. Even if the mask is removed with acid, the diamond surface is still difficult to recover to the origin surface. The second growth step can remove these contamination, then the surface become clean, leading to a strong photoresponse. Figures 4-17 (a) and (b) show a case of diamond surface contamination. The SEM images are diamond surface before and

after titanium dioxide (TiO_2) pickling. TiO_2 was deposited on diamond surface by magnetron sputtering, and then heated for 2 hours in a mixture of 1:1 volume ratio of sulfuric acid and nitric acid at 250 ℃. After pickling, the pattern of TiO_2 can not be observed under optical microscope, but the contour covered by TiO_2 can be clearly seen under scanning electron microscope.

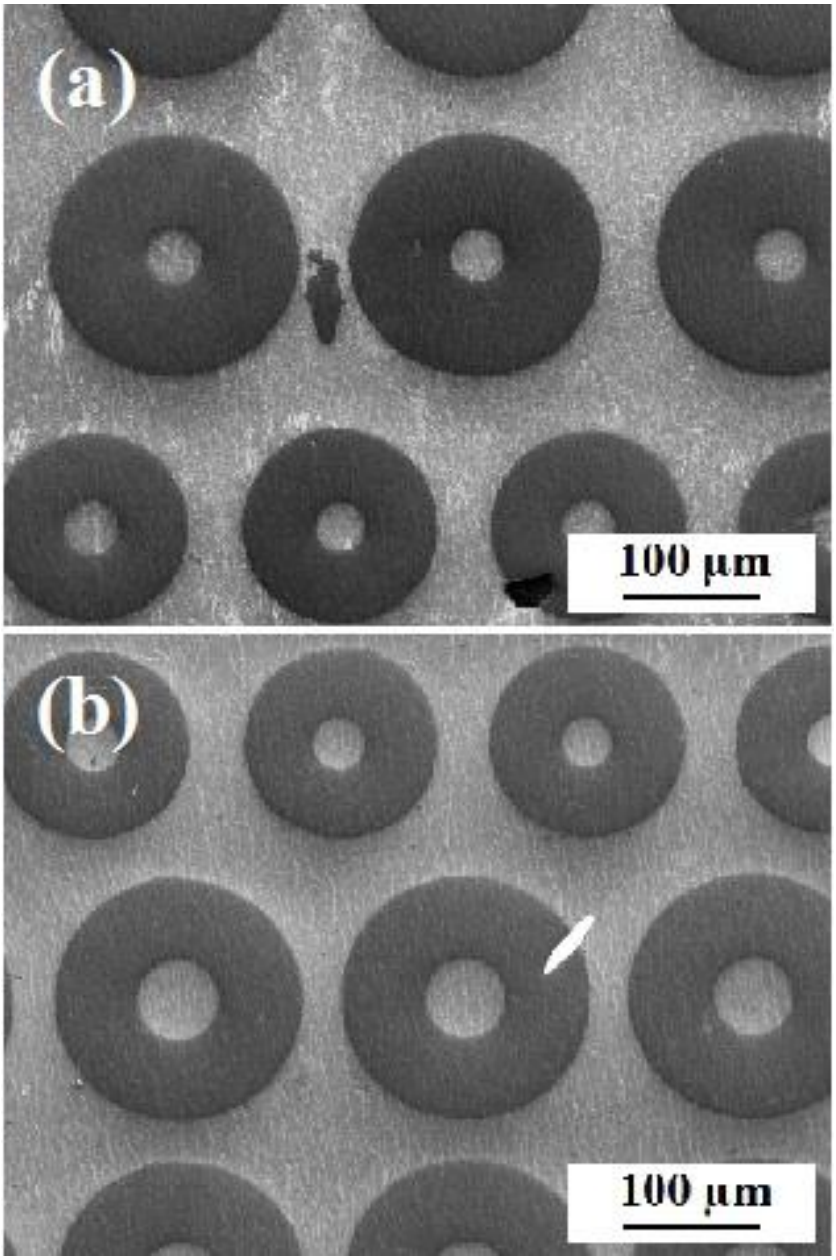

Figure 4-17 SEM images of diamond surface (a) before and (b) after TiO_2 pickling

Figure 4-19 shows the atomic force microscopy (AFM) morphology of the sample surface before and after recovering growth in this experiment. The apparent changes of the sample surface can be clearly observed from the AFM images. Before covering growth, there are many tips on the surface, but after repair growth, the surface becomes smooth, the number of

tips decreases and the sharpness decreases. This shows that recovering growth can also repair metal-contaminated diamond surface. It is precisely because the surface of diamond becomes clean after recovering growth that the photoelectric response of the material is improved.

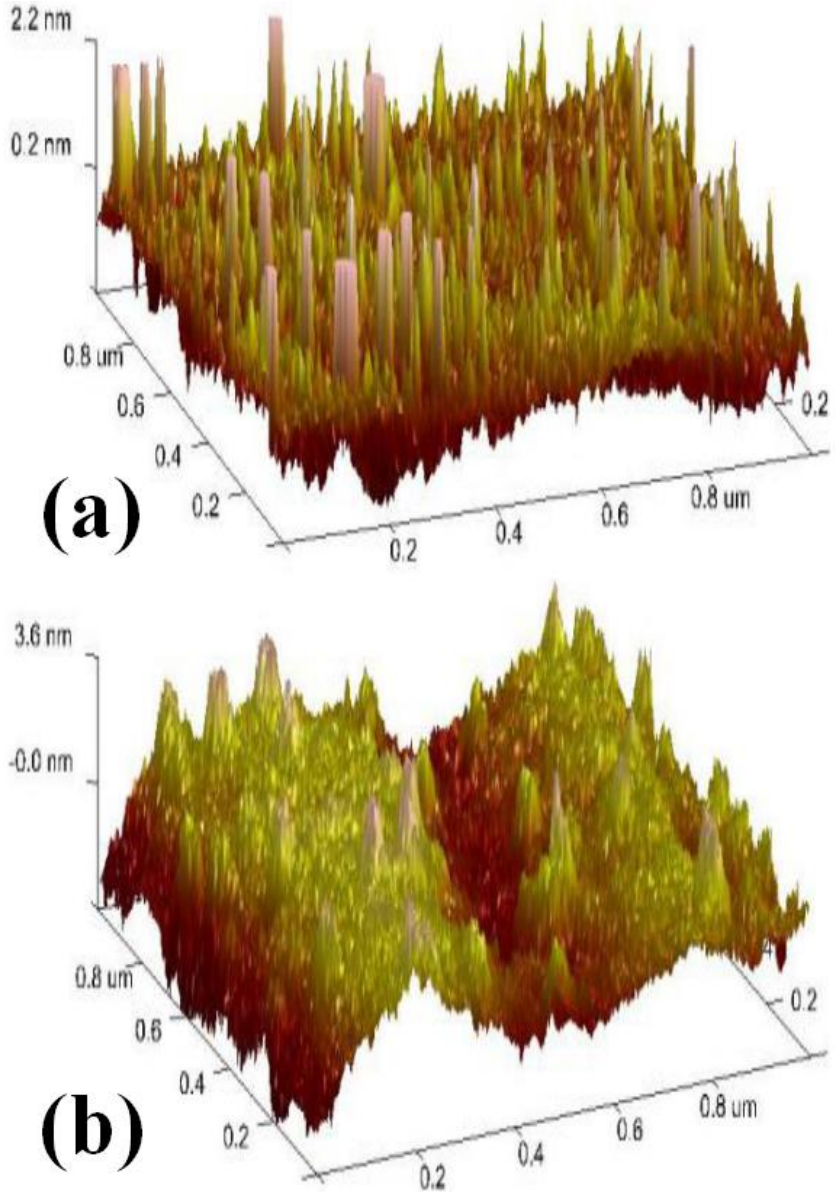

Figure 4-18 AMF images of unetched diamond surface (a) before and (b) after recovering growth.

Figure 4-19 shows shows the spectral responsivity of Q1D detector and planar detector at 20 V when the electrode space is 30 μm. In the UV region, the responsivity of Q1D detector is higher than that of planar detector. At 215 nm, the responsivity of Q1D detectors reaches the maximum of 16.3 mA/W, while that of planar detectors is 7.32 mA/W at 215 nm, which means that the responsivity of Q1D detector is 2.2 times higher than that of planar detector.

In the visible region, the responsivity of Q1D detector is lower than that of planar detector after the wavelength is more than 450 nm. At 400 nm wavelength, the responsivity of Q1D detector and planar detector are 2.45 μA/W and 2.27 μA/W, respectively. The UV/visible rejection ratios of Q1D detector and planar detector are calculated to be 6.65×10^3 and 3.22×10^3, respectively. Therefore, the Q1D detector not only has a large UV responsivity, but also has a high UV/visible rejection ratio.

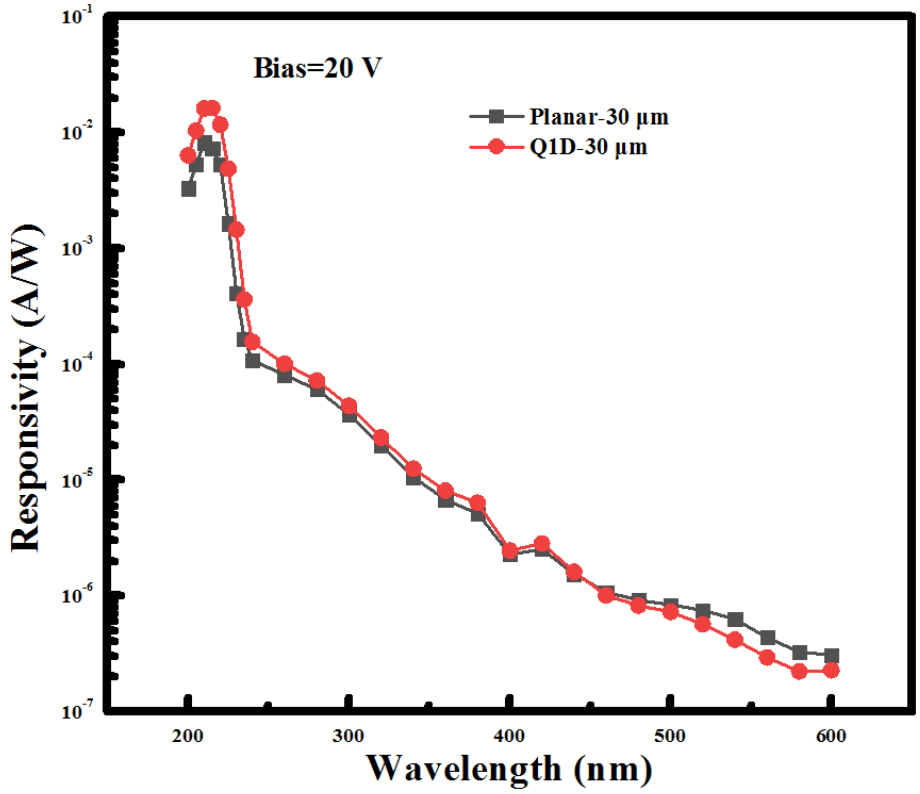

Figure 4-19 Spectral responsivity of Q1D detector and planar detector at 20 V when the electrode space is 30 μm.

Figure 4-20 shows the time response performance of Q1D detector and planar detector after second step growth. The electrode space is 30 μm, the incident light wavelength is 210 nm, and the optical power density is 0.366 μW/mm^2. The photocurrents of the two detectors have similar trends with time. When the optical signal is applied, the current of the detector increases rapidly to the saturation value; when the optical signal is removed, the current drops rapidly to the initial value. The rapid decrease of dark current indicates that there is no persistent photoconductivity effect, which discloses that the quality of diamond material is good. The rise and fall times of Q1D detectors are 800 ms and 18 ms respectively, while the rise and fall times of planar detectors are 1618 ms and 24 ms respectively, which shows that Q1D detectors have faster response speed. In addition, the switching current ratio of Q1D

detector is 309, while that of planar detector is only 267, which shows that Q1D detector has better time response performance.

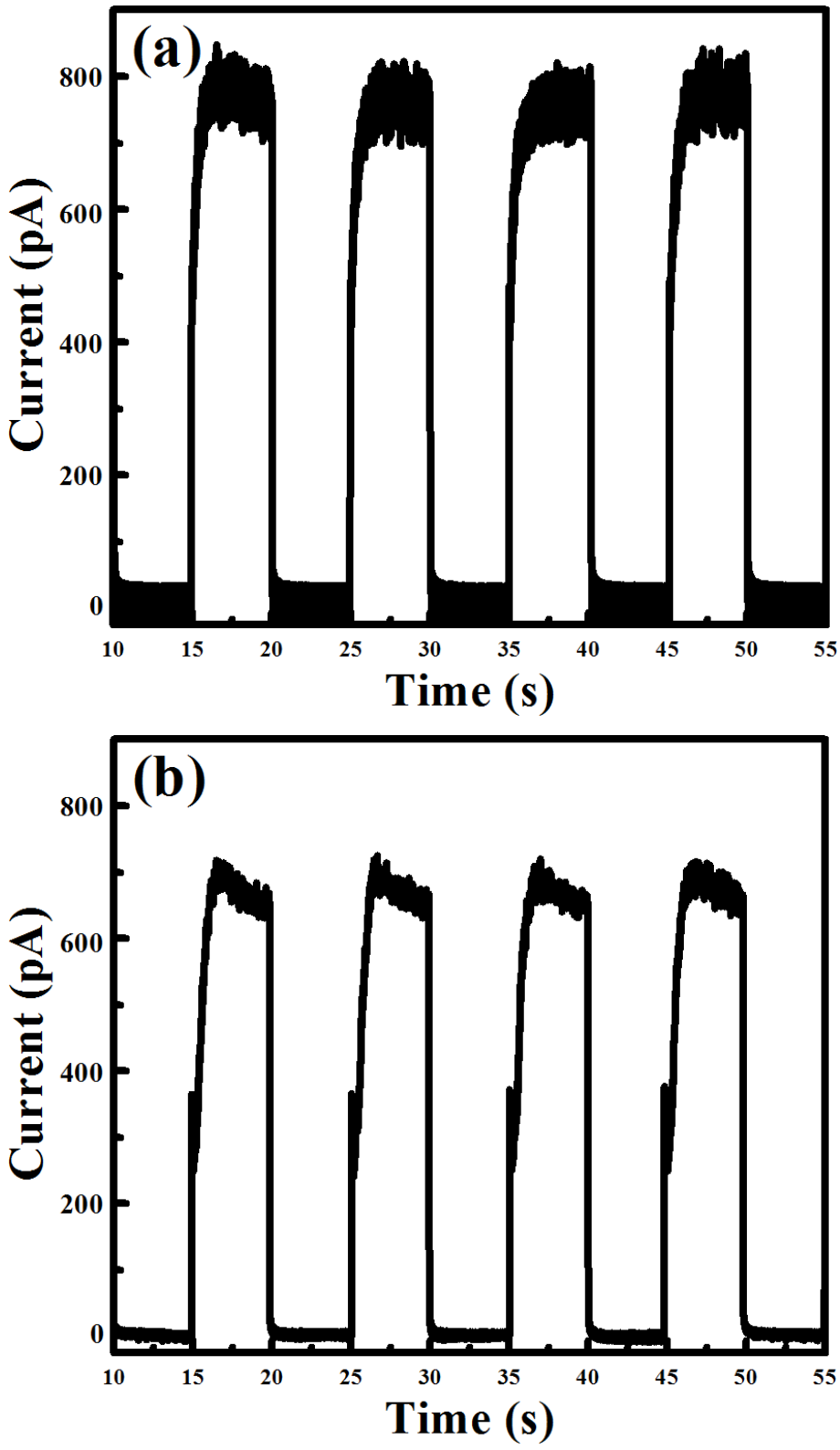

Figure 4-20 Time response performance of (a) Q1D and (b) planar detectors.

In order to further explore the effect of electrode space on the Q1D detectors, we compare

the performance ounder the same electric field intensity. Figure 4-21(a) shows the relationship between the responsivity of Q1D detectors at different space and the electric field intensity. It can be seen that the responsivity of the detector increases with the increase of electric field intensity, and the increasing speed in the UV region (215 nm) is faster than that in the visible region (400 nm). In the UV region, the responsivity of the detector reaches 22.21 mA/W under 16 kV/cm electric field when the electrode space is 30 μm. At low electric field intensity, the responsivity of 20 μm space detector is higher than that of 10 μm space detector, while at high electric field intensity, the responsivity of 20 μm space detector is lower than that of 10-μm space detector. In the visible region, the responsivity of the detector decreases with the increase of the electrode space. This indicates that the increase of the electrode space can reduce the light response of the device in the visible region. Figure 4-21(b) shows the relationship between the 210 nm/400 nm UV/visible rejection ratio and the electric field at different space of Q1D detectors after second step growth. It can be observed that the rejection ratio of the device increases with the increase of electric field intensity. In addition, the rejection ratio is also related to the electrode space, which increases with the increase of the electrode space. At 16 kV/cm, the rejection ratios of 30, 20 and 10 μm space detectors are 6.65×10^3, 3.74×10^3 and 2.35×10^3, respectively. The high rejection ratio indicates that the device has good spectral selectivity, and the larger the electrode space, the better the spectral selectivity of the device.

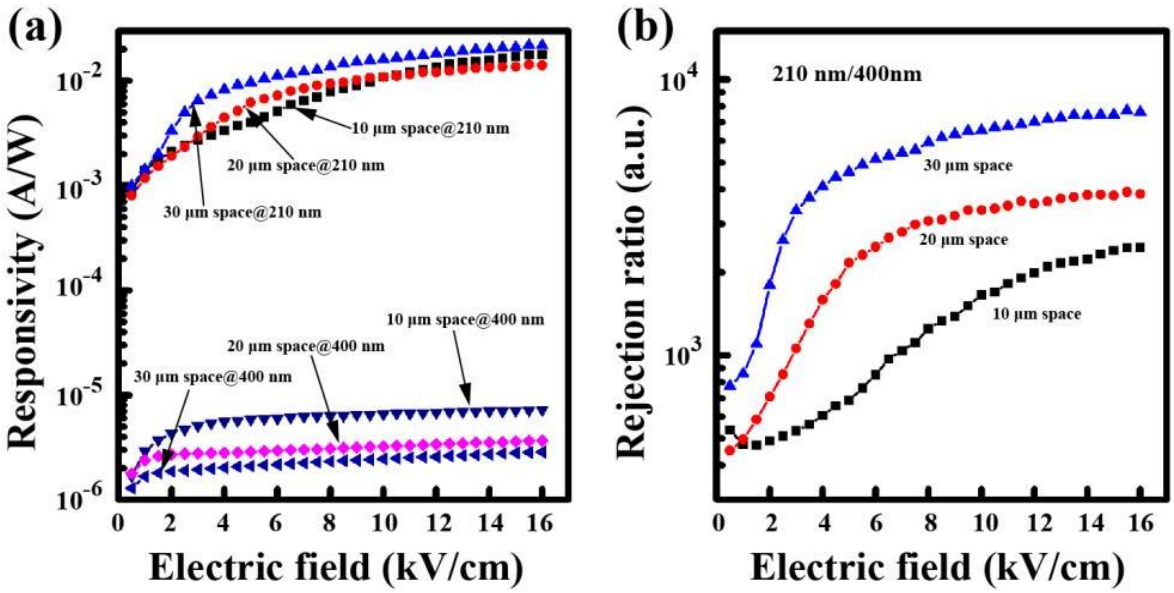

Figure 4-21 (a) Responsivity at 210 nm and 400 nm and (b) 210 nm/400 nm rejection ratio of Q1D detectors with different electrode space dependence on electric field.

For photodetectors, the responsivity is proportional to the internal photoelectric gain

(G). The expression of internal photoelectric gain is as follows:

$$G = \frac{V}{kT}\left(\frac{\lambda_{DL}}{L}\right)^2 \qquad (4\text{-}2)$$

where V is the bias voltage and L is the electrode space [67]. When the bias voltage and the distance between electrodes are constant, the diffusion length determines the internal photoelectric gain. In the Q1D transport mode, the carrier diffusion length increases [72]. Therefore, under the same electrode spacing and bias voltage, the response of Q1D structure detector is higher than that of planar structure detector. At the same time, formula (4-2) can also be rewritten as follows:

$$G = \frac{E}{kT}\frac{\lambda_{DL}^{\ 2}}{L} \qquad (4\text{-}3)$$

where E = V/L is the electric field strength. It can be seen that under the same electric field intensity, the larger the distance between the electrodes, the smaller the internal photoelectric gain. Therefore, the responsivity of the detector with 20-μm space is smaller than that of the detector with 10-μm spacing. But there is another factor to be considered, that is, the increase of photosensitive area. At larger electrode space, the number of photogenerated carriers is larger, so although the gain is slightly smaller, it can still obtain a larger responsivity.

Figure 4-22 shows the time response of Q1D detectors with different space. The bias voltage is 20 V and the light wavelength is 215 nm. The current-time curves under different space are similar: when the light signal is applied, the current increases rapidly to its maximum value, then decreases slowly; when the light signal is withdrawn, the current value decreases rapidly and falls back to its initial value. Under the second light pulse, the maximum current of the device is less than that under the first light pulse. The dynamic response of the device is different from the static response. The rise time of the device with 30, 20 and 10 μm space is 105 ms, 430 ms and 470 ms, and the decay time is 25 ms, 20 ms and 28 ms, respectively. The rise time of the device decreases with the increase of the electrode space, while the decay time is close. In conclusion, the detector has a faster response speed at a larger electrode space.

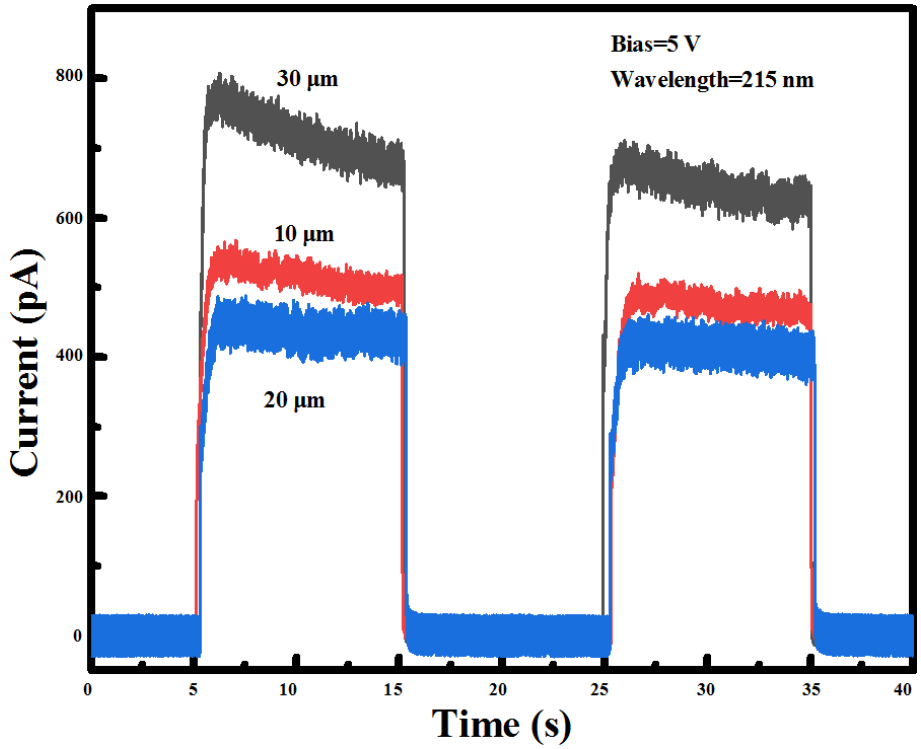

Figure 4-22 Time response of Q1D detectors with different space.

4.5 Summary

Low-dimensional materials have unique physical properties. In this chapter, the design of Q1D structure is applied to single crystal diamond UV photodetectors for the first time, and its performance is characterized. Q1D diamond UV detector were obtained by etching diamond strips on the surface of diamond and setting the interdigital electrodes perpendicular to the direction of diamond strips. Because of the etching defects, the as-fabricated detectors have better performance than planar detectors only when the electrode spacing is large, and the photocurrent of the detectors is increased by 14.6%. The surface defects were repaired by diamond secondary epitaxy technology, and the Q1D structure detectors were fabricated again. The photocurrent of the repaired detector is larger than that of the planar structure. When the distance between the electrodes is 30 μm, the photocurrent even increases by 106%. In addition, the responsivity, UV/visible rejection ratio and transient response performance of Q1D structure detector are better than those of planar structure detector with the same electrode spacing. The experimental results show that the performance of diamond UV photodetectors can be effectively improved by combining QiD structure design with secondary epitaxy surface defect repair.

5 TiO_2/diamond UV photodetector

5.1 Introduction

The band gap of diamond is 5.45 eV, and the corresponding cut-off wavelength is 225 nm. Therefore, when the wavelength of light is greater than 225 nm, diamond is transparent. Therefore it transmits most of the optical signals in the ultraviolet band. In order to expand the scope of diamond detectors, diamond and other wide bandgap semiconductors can be combined.

TiO_2 is also a kind of broadband gap semiconductor. It has three crystal structures: slate, anatase and rutile. The band gap is 2.36 eV, 3.2 eV and 3.0 eV, respectively. Among them, the band gap of anatase phase TiO_2 corresponds to the boundary between ultraviolet and visible wavelength. TiO_2 also has excellent photoelectric properties and many studies focus on gas sensors, photocatalysis and solar cell applications [73]. In recent years, Huang *et al.* have fabricated TiO_2-based photodetectors [74,75] with very low dark current and high response by magnetron sputtering. We know that for photodetectors, when the photon energy is larger than the bandgap, the responsivity will gradually decrease [76]. Therefore, the combination of TiO_2 and diamond can not only expand the spectrum detection range of diamond, but also improve the responsivity. In this work, we try to deposit TiO_2 directly on the epitaxial layer of single crystal diamond in order to develop ultraviolet photodetectors and study their photoelectric properties.

5.2 Preliminary study of TiO_2/diamond UV photodetector

5.2.1 Experiment

Figure 5-1 shows the fabrication process of TiO_2/diamond UV photodetector. About 200 nm undoped single crystal diamond epitaxial layer was grown on 3×3×0.3 mm^3 Ib-type HPHT diamond substrate by microwave plasma chemical vapor deposition method. The total flow rate of H_2 and CH_4, the ratio of $CH_4/(H_2+CH_4)$, the process pressure, the growth temperature and the microwave power were 500 sccm, 0.8%, 80 Torr, 850 ℃ and 800 W, respectively. Raman spectrum was used to characterize the quality of the epitaxial layer. After growth, the sample was boiled in acid mixture (H_2SO_4:HNO_3=1:1 by volume) at 300℃

for 2 h to change the hydrogen terminated surface to oxygenated surface.

Half of this epitaxial layer was used to deposit TiO_2 by radio frequency magnetron sputtering technique. The source material was 3 inches sintered TiO_2 ceramic target with the purity of 99.99%. The background pressure was as low as 3×10^{-4} Pa. Ar and O_2 were used as sputtering gas, whose flow rate were 40 sccm and 20 sccm, respectively. Before deposition, the target was cleaned by Ar ion for five minutes. During sputtering process, the power was 150 W, and the working pressure was 1.2 Pa. The thickness of TiO_2 was measured to be 450 nm. Another half of diamond layer remained as oxygenated surface state.

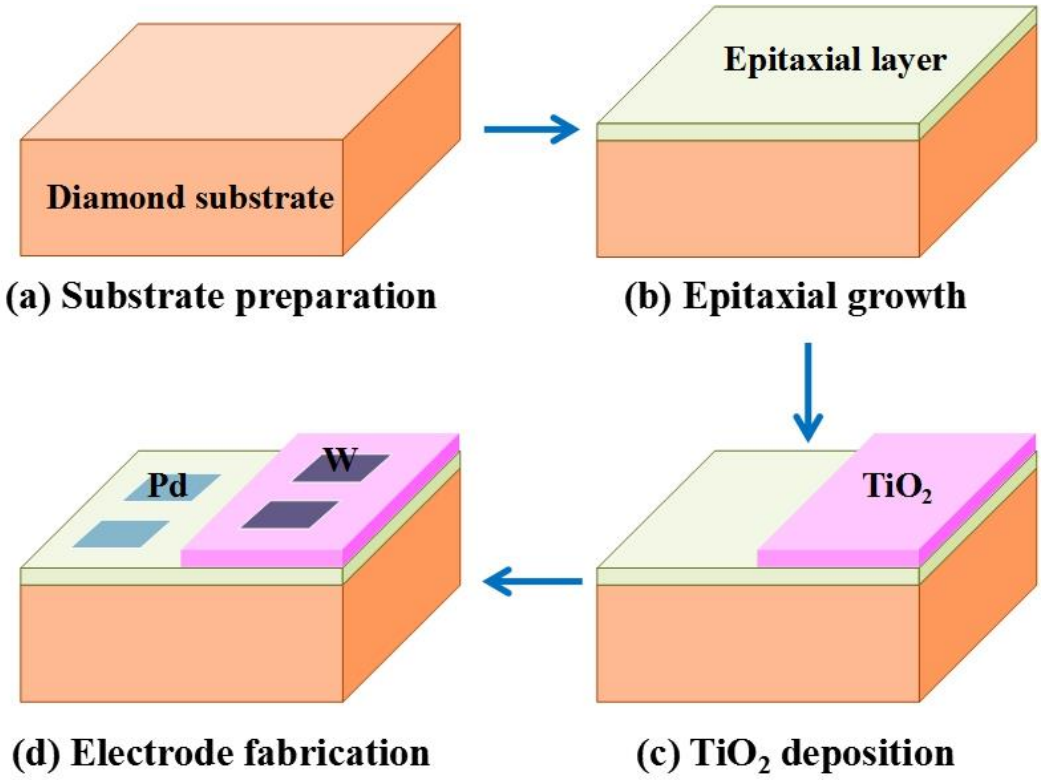

Figure 5-1 Fabrication process of TiO_2/diamond UV photodetector.

Two W electrodes with a thickness of 100 nm were patterned on TiO_2/diamond film using radio frequency magnetron sputtering method to fabricate the novel photodetector. The electrode width was 1000 μm and the space between electrodes was 200 μm. Thus the total active area was 0.2 mm^2. Two Pd electrodes with a thickness of 50 nm were patterned on diamond film using thermal evaporation method to fabricate traditional diamond photodetector. These two electrodes had the same parameters as W electrodes. The I-V characteristics of the as-fabricated photodetectors were investigated by Agilent B1505A power device analyzer. The optoelectronic properties were evaluated with a Keithley 6487 picoammeter/voltage source, a 500 W Xe lamp source and a monochromator. The light

power at the sample surface was measured by a commercial UV-enhanced Si detector. The time response is measured by a KrF excimer laser and an oscilloscope.

5.2.2 Results and discussion

The inset in Figure 5-2 shows SEM photograph of the boundary between diamond and titanium dioxide. It is obvious that there is a boundary between the diamond surface and the titanium dioxide surface, which indicates that the titanium dioxide film is deposited on the magnetron sputtered electrode successfully. In order to further determine the composition of the film, X-ray photoelectron spectroscopy (XPS) was used to characterize the film. Figure 5-2 shows the XPS spectra of titanium. Two peaks, Ti 2p1/2 458.8 eV and Ti 2p3/2 464.5 eV, can be observed. The difference between the two peaks is 5.7 eV, indicating that the film is titanium dioxide [75].

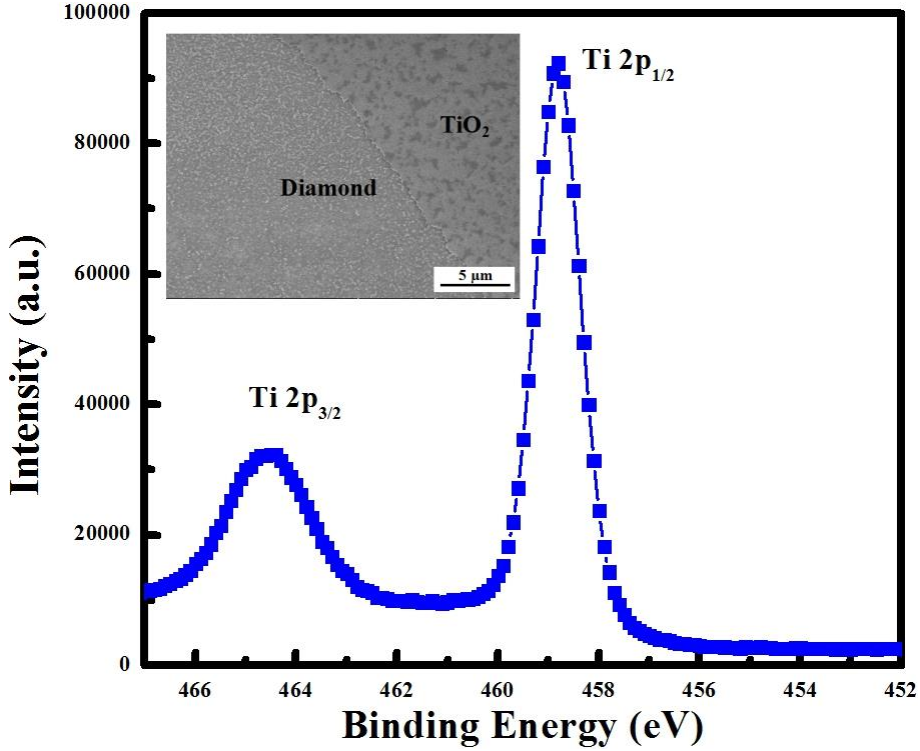

Figure 5-2 XPS spectrum of Ti 2p. The inset is SEM image of the boundary between diamond and TiO_2.

Dark currents of diamond detector and TiO_2/diamond detector were investigated and shown in Figure 5-3. Both I-V curves are almost linear, showing that W/TiO_2 and Pd/diamond contacts are both ohmic contacts. The dark current of sample A was measured to be 0.5 pA at bias voltage of 4 V. When the bias voltage increased to 30 V, the dark current increased slowly to 1.12 pA. For sample B, the dark currents are 1.28 pA and 1.9 pA at 4 V

and 30 V, respectively. Both detectors show extremely low dark current, which plays an important role in lowering the signal to noise ratio [77]. Moreover, the dark currents are comparable, indicating that TiO_2 film on diamond may not introduce additional leakage current path.

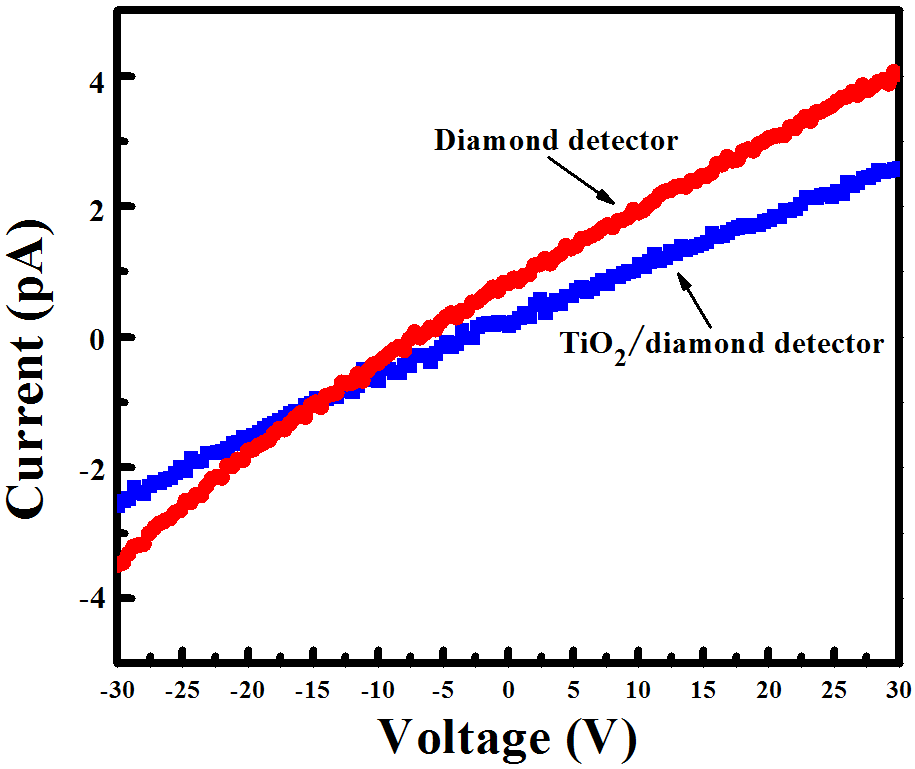

Figure 5-3 Dark currents of diamond detector and TiO_2/diamond detector

The photocurrents of diamond detector and TiO_2 detector were investigated by using UV-light with the parameter of 180 nW/mm^2 at 220 nm and 23 μW/mm^2 at 340nm, as shown in Figure 5-4. Compared with dark currents shown in Figure 5-3, it indicates a significant increase of photocurrent in Figure 5-4. For both detectors, photocurrents increase with bias voltage increasing, and no saturation phenomenon appears even at 30 V. A possible reason is that the electric field is not strong enough to collect all the photo-generated carriers before their recombination. Under the illumination of both 340 nm and 220 nm, the photocurrents of TiO_2/diamond detector are bigger than that of diamond detector, indicating a higher photo response.

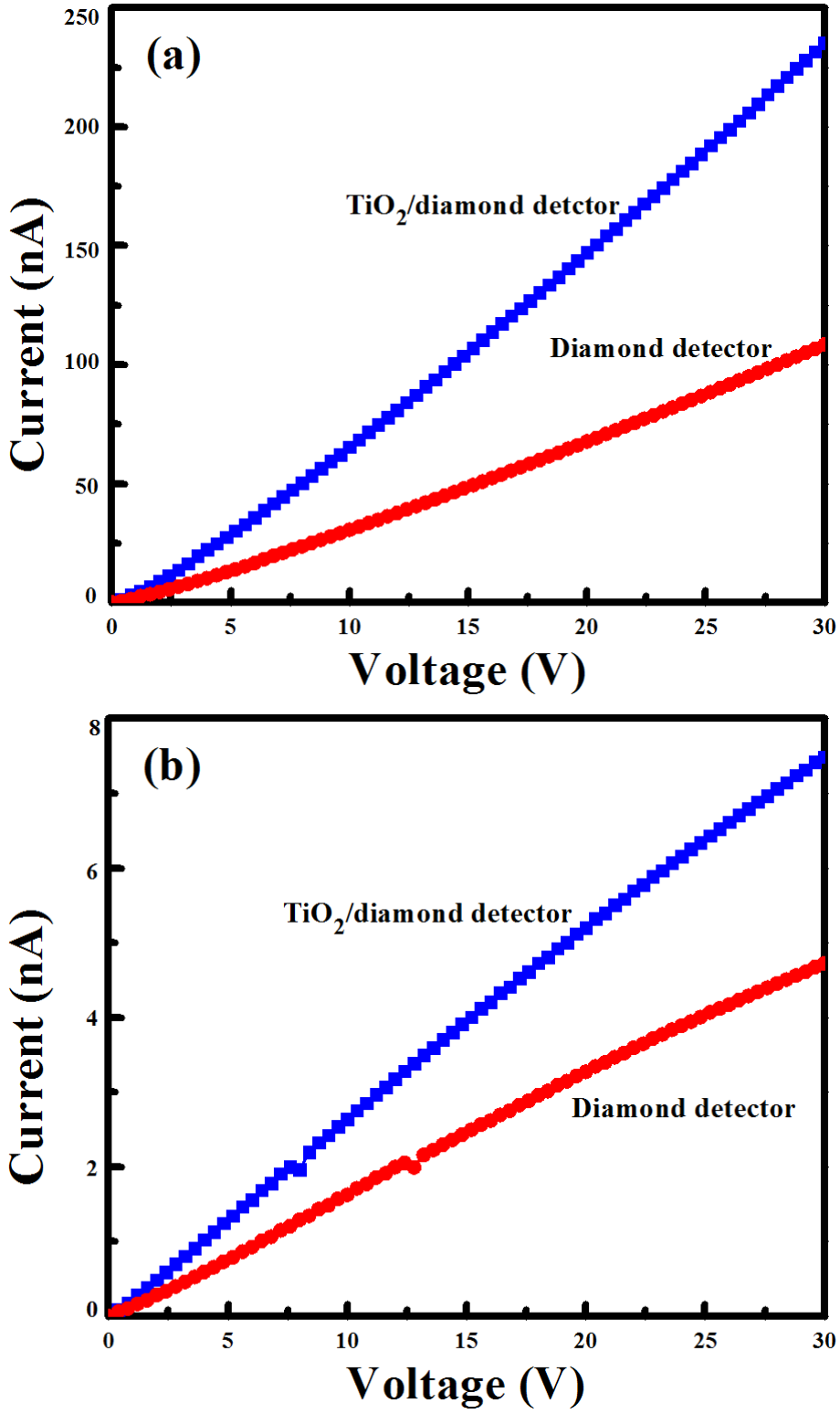

Figure 5-4 Dark currents of diamond detector and TiO_2/diamond detector.

Figure 5-5 shows the responsivity of TiO_2/diamond detector varying with the wavelength changing under different bias voltages. The photo responsivity shows a decrease tendency with wavelength increasing. An obvious rejection ratio between UV and visible light can be

observed. When the bias voltage is 10 V, under the illumination of 220 nm, 340 nm and 400 nm, the responsivity is calculated to be 0.071 A/W, 0.013 A/W and 0.00071×10^{-4}, respectively. Thus, the UV-to-visible rejection ratios for 340 nm versus 400 nm and 220 nm versus 400 nm are 18 and 100, respectively. When the bias voltage is increased to 30 V, the responsivity is evaluated to be 0.2 A/W, 0.048 A/W and 0.0019 A/W, leading to rejection ratios of 25 and 105, respectively. This indicates that when the bias voltage increases, the responsivity and rejection ratio also increase. The phenomenon is in agreement with the unsaturation of photocurrent. When higher electric field is applied, more photo-generated carriers can be collected, leading to responsivity enhancement. The detectivities at 220 nm and 340nm are 6.57×10^{10}/W and 1.33×10^{10}/W, respectively, indicating good UV detective ability.

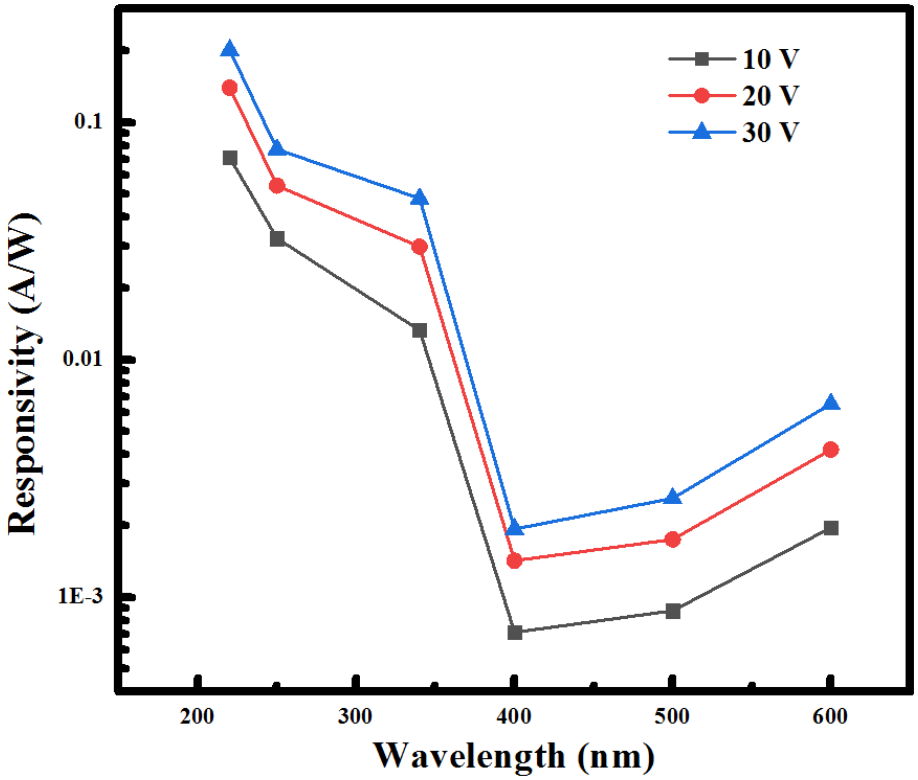

Figure 5-5 Spectral responsivity of TiO_2/diamond detector under different bias voltages.

Figure 5-6 shows the spectral response of both detectors at 30 V, which displays the difference between TiO_2/diamond detector and diamond detector. For diamond detector, when the bias voltage is 30V, under the illumination of 220 nm, 340 nm and 400 nm, the responsivity is calculated to be 0.13 A/W, 0.02 A/W and 0.0019 A/W, respectively. The UV-to-visible rejection ratio for 340 nm versus 400 nm is 11, while that for 220 nm versus 400 nm is 68. Compared with TiO_2/diamond detector, both of the responsivity and rejection

ratio are lower. This means that the structure of TiO_2/diamond can enhance the detector responsivity and rejection ratio.

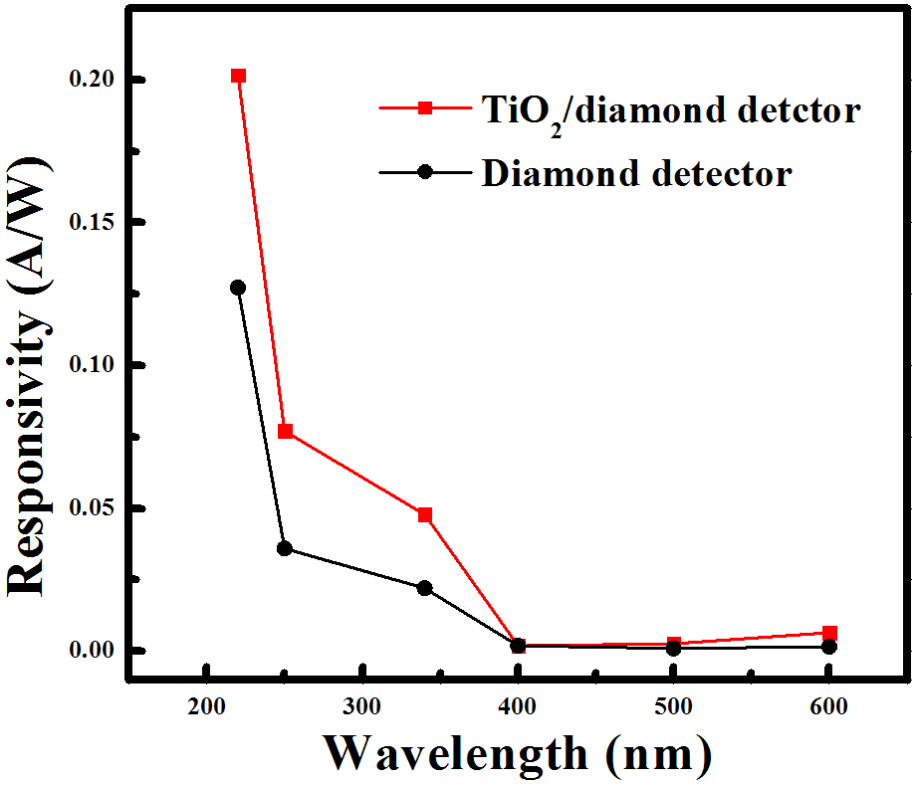

Figure 5-6 Spectral responsivity of both detectors at 30 V.

5.3 Effect of TiO_2 thickness on TiO_2/diamond UV photodetector

5.3.1 Experiment

In section 5.2, the film of TiO_2 is thick, and the penetration depth of ultraviolet light decreases with the shortening of wavelength, so it will affect the ultraviolet light reaching the diamond surface. In this section, we will study the effect of TiO_2 film thickness on detector performance. Firstly, a single crystal diamond film is grown by placing a single crystal diamond substrate in the MPCVD cavity. The substrate was made of 3 mm × 3 mm × 0.3 mm HPHT Ib (100)-oriented single crystal diamond, which was cleaned by acid, alkali and organic before growth. The growth parameters of epitaxy layer are as follows: the total flow rate of reaction gas is 500 sccm, the ratio of CH_4 to H_2 is 1%, the process pressure, growth temperature and microwave power are 100 Torr, 900 ℃ and 1 kW, respectively, and the thickness of epitaxial layer is about 200 nm. After the growth, the diamond samples were heated for 1 h at 260 ℃ in a 1:1 volume ratio sulfuric acid/nitric acid mixture to remove the surface hydrogen terminal.

Using photolithography technology, photoresist masks were prepared on the epitaxial layer surface to cover three-quarters of the surface in turn, and TiO_2 films were deposited on the exposed one-quarter diamond surface. TiO_2 was deposited by radio frequency magnetron sputtering. The raw material was sintered 3 inch TiO_2 ceramic target with 99.99% purity. The background chamber pressure of magnetron sputtering is 3×10^{-4} Pa, the working gas is argon and oxygen, and the flow velocities are 40 sccm and 20 sccm, respectively. Before deposition, the target is cleaned with argon ion for 5 minutes. In the sputtering process, the RF power is 150 W, the working pressure is 1.2 Pa, and the thickness of TiO_2 film is 2, 6, 12 and 18 nm, respectively.

Finally, tungsten interdigital electrodes with 150 nm thickness were fabricated on the surface of TiO_2 by photolithography and radio frequency magnetron sputtering, and the TiO_2/diamond ultraviolet detector was obtained. The width of the electrode is 12 microns, the distance between the electrodes is 8 μm, and the total active area is 0.33 mm^2. The IV characteristics of the detectors were studied by Agilent B1505A power device analyzer and monochrome light source system.

5.3.2 Results and discussions

Figure 5-7 shows the optical photos of the detectors. It can be seen that the preparation process is very successful, and the boundary of the four regions of the titanium dioxide film can be clearly seen.

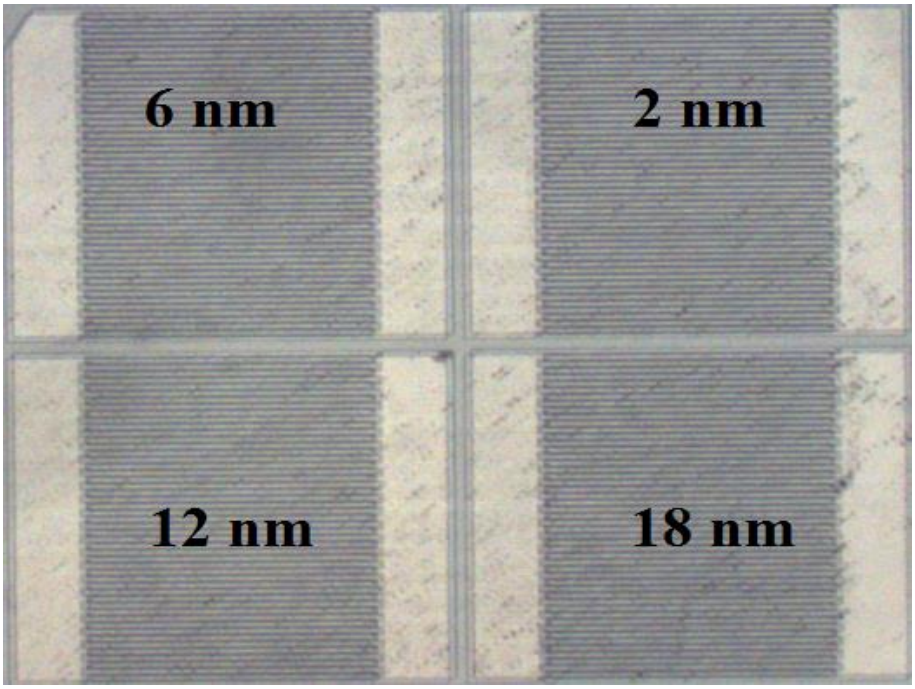

Figure 5-7 Optical image of TiO_2/diamond detectors with different TiO_2 thickness.

Figure 5-8 shows the XPS spectra of Ti elements in different TiO_2 thickness. At each film thickness, there are two peaks of Ti: Ti 2p 1/2 and Ti 2p 3/2. Although the positions of Ti 2p 1/2 and Ti 2p 3/2 peaks are different, the difference between the two peaks is 5.7 eV or 5.8 eV for thin films with thickness of 2, 6, 12 and 18 nm, which indicates that the thin films are TiO_2 thin films. It is found that the positions of Ti 2p 1/2 and Ti 2p 3/2 peaks move towards high binding energies with the increase of the TiO_2 thickness. This is because the bonding energy of TiO_2 films deposited on diamond is affected by diamond, which decreases with the increase of film thickness, and the bonding energy increases gradually. In addition, the intensity of Ti 2p 1/2 and Ti 2p 3/2 peaks also increases with the increase of film thickness, which is due to the increase of detected Ti element, thus enhancing the signal.

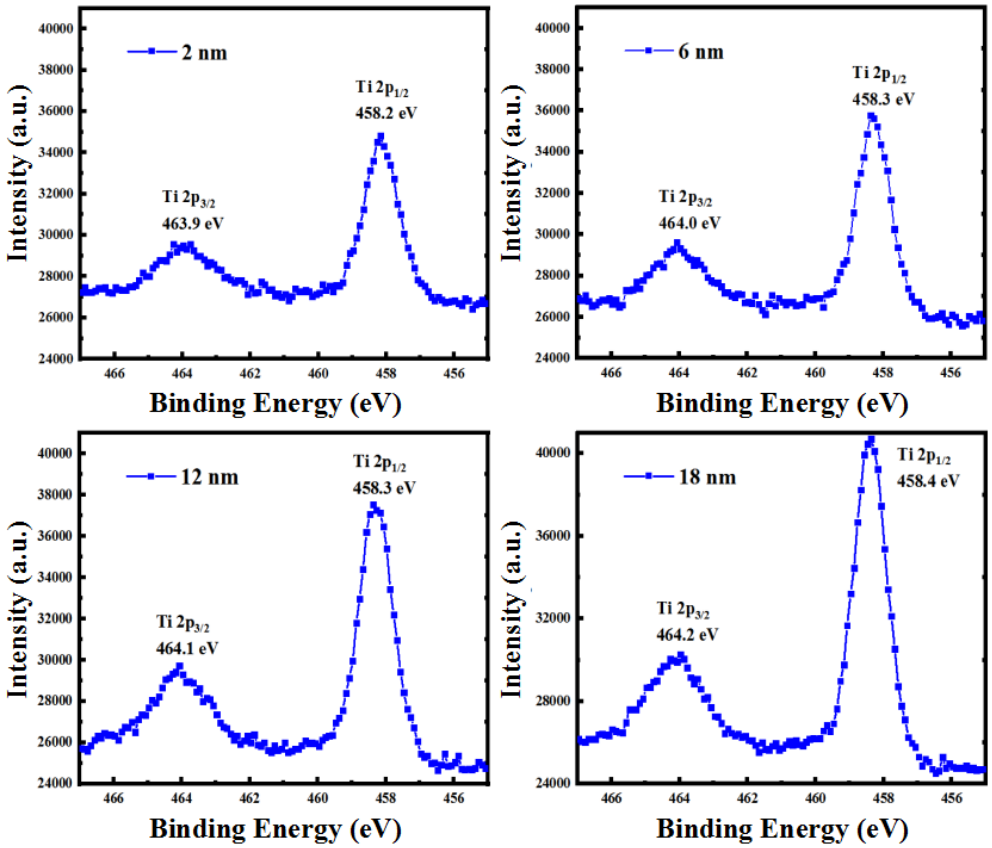

Figure 5-8 XPS spectra of Ti elements with different TiO_2 thickness.

Since diamond affects the peak position of Ti 2p, then TiO_2 also affects the C 1s peak on the surface of diamond. Figure 5-9 shows the XPS spectra of C element in different thickness of TiO_2 region. Under each film thickness, the C 1s element can also be divided into two peaks, one representing the sp^3-C peak of diamond and the other representing the C-O-C bond on the surface of oxygen-terminated diamond. It can be seen from the figure that the sp^3-C peak of diamond is at 284.0 eV and its position is basically unchanged. The C

peak of C-O-C bond on oxygen-terminated diamond surface moves to low binding energy with the increase of the TiO_2 thickness. When the TiO_2 thickness is 6, 12 and 18 nm, the peak is less near 285.2 eV, while when the TiO_2 thickness is 2 nm, the peak moves to 285.7 eV. This is because after deposited on diamond, because of its thin thickness, the TiO_2 film will interact with the carbon atoms on the diamond surface, making the binding energy larger. With the increase of film thickness, titanium atoms and oxygen atoms at the interface between TiO_2 film and diamond mainly combine with oxygen atoms and titanium atoms in TiO_2, so the influence of C-O-C bond becomes smaller and the binding energy becomes smaller. In addition, the intensity of C1s peak decreases with the increase of the TiO_2 thickness, because the X-ray penetration depth is limited, and the intensity of light reaching the diamond decreases, which weakens the excitation signal.

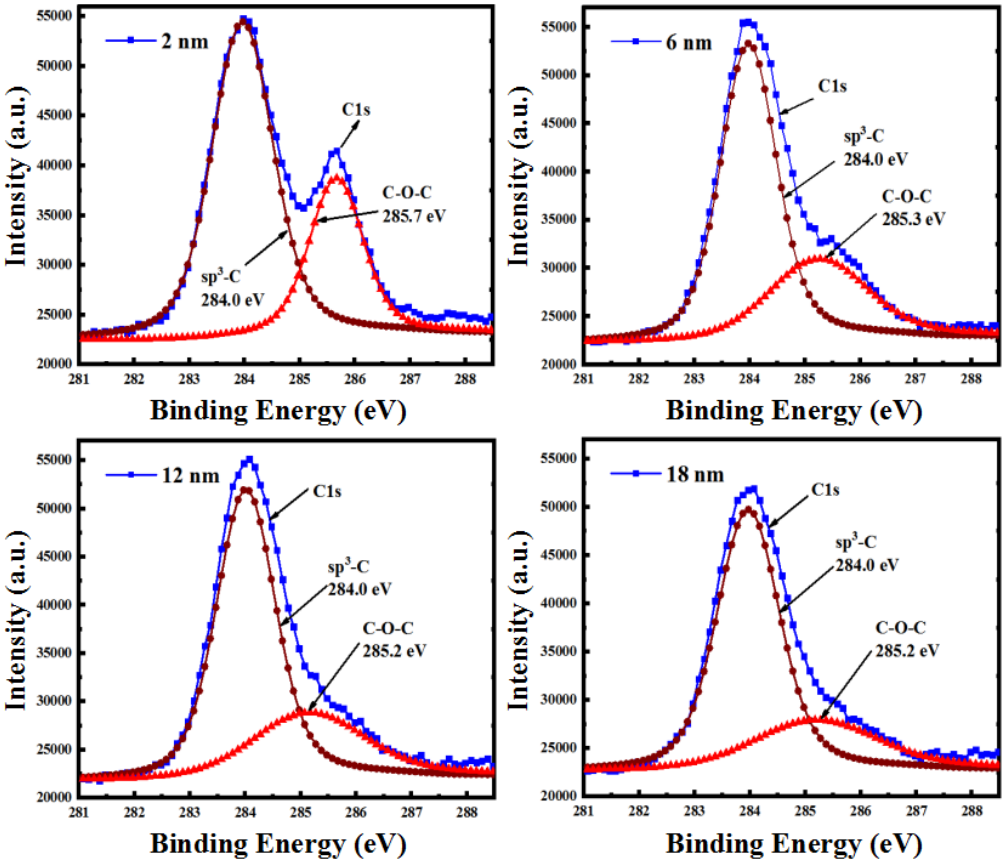

Figure 5-9 XPS spectra of C 1s peak covered with different thick TiO_2.

Figure 5-10 shows the dark current characteristics of the TiO_2/diamond detectors. It can be seen that the 2 nm TiO_2/diamond detector has a non-linear IV curve, while the 6, 12 and 18 nm TiO_2/diamond detector has a linear IV curve. In addition, the dark current of 2 nm TiO_2/diamond detector is the largest, reaching 314 pA at 8 V. When the thickness of TiO_2 changes from 2 to 6 nm, the dark current decreases sharply and is only 0.75 pA at 8 V. As the

thickness of TiO_2 continues to increase, the dark current of the device also increases slightly. The dark current of the TiO_2/diamond detector with 12 and 18 nm thick TiO_2 is 4.33 pA and 4.58 pA, respectively. When TiO_2 is deposited on diamond, because the Fermi level of diamond is higher than that of TiO_2, some electrons on the surface of diamond are transferred to the TiO_2 film to balance the Fermi level, resulting in extra electrons in the TiO_2 film near the interface and extra holes in the diamond. Although the TiO_2 film is dielectric [78,79], when its thickness is 2 nm, these additional carriers can pass through the film under a sufficient bias voltage and be collected by the electrode, resulting in an increase in dark current. Therefore, the dark current of 2 nm TiO_2/diamond detector is very small at low voltage, but increases rapidly at high voltage. When the thickness of TiO_2 film increases to 6 nm, the additional carriers near the interface can not pass through TiO_2 film, resulting in a sharp decrease in dark current. As the thickness of TiO_2 increases from 6 to 18 nanometers, the dark current increases slightly. This phenomenon may be due to the existence of more defects when the TiO_2 film is thicker, resulting in additional conductive paths [80]. Therefore, the dark current increases.

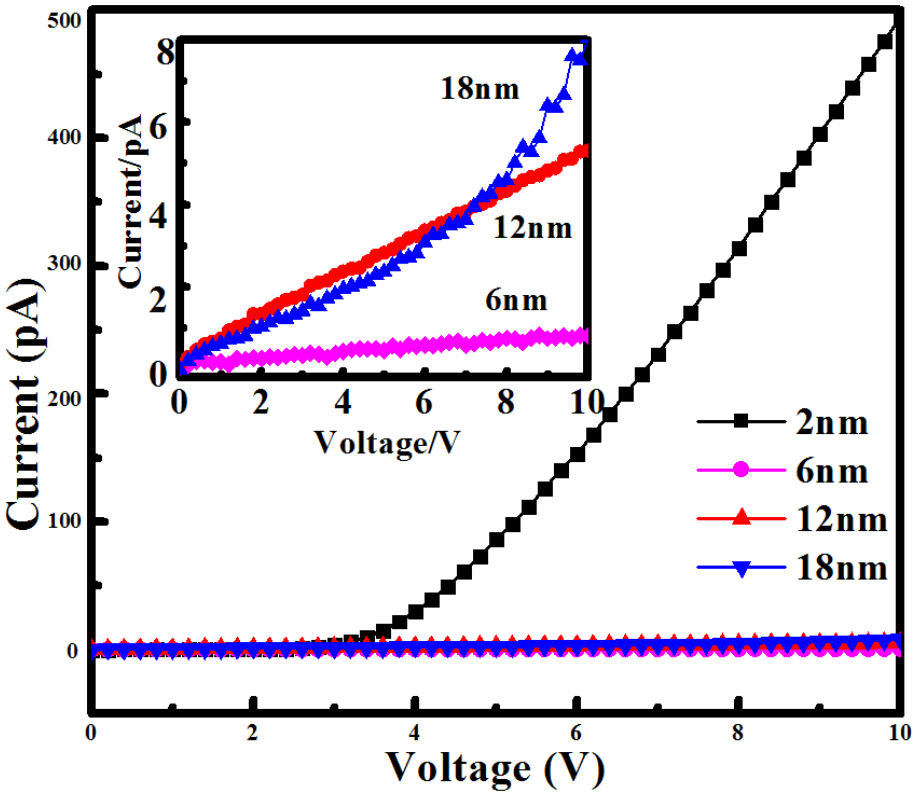

Figure 5-10 IV characteristics of the TiO_2/diamond detectors with different thick TiO_2.

Figure 5-11 shows the photocurrent of TiO_2/diamond detectors with different thick TiO_2. Under 220 nm and 335 nm irradiation, the current of the device increases rapidly, which is

much larger than the dark current of the device. However, under visible (660 nm) irradiation, the current of the device increases less, indicating that the device has good spectral selectivity. Because of the existence of TiO_2, the photocurrent of the device at 335 nm is larger than that at 220 nm, and the photocurrent increases when the film thickness increases from 6 to 18 nm. The net photocurrent can better show the photocurrent characteristics of the device. Under 8 V bias, the net photocurrents of 2 nm, 6 nm, 12 nm and 18 nm-TiO_2/diamond detectors under 220 nm illumination are 0.301 nA, 0.289 nA, 0.299 nA and 0.387 nA, respectively, and those under 335 nm illumination are 1.17 nA, 0.966 nA, 1.33 nA and 25.1 nA, respectively. It can be seen that the net photocurrent increases as the film thickness increases from 6 to 18 nm. When the thickness of titanium dioxide film is 2 nm, the photocurrent is unique due to the interaction between diamond and TiO_2.

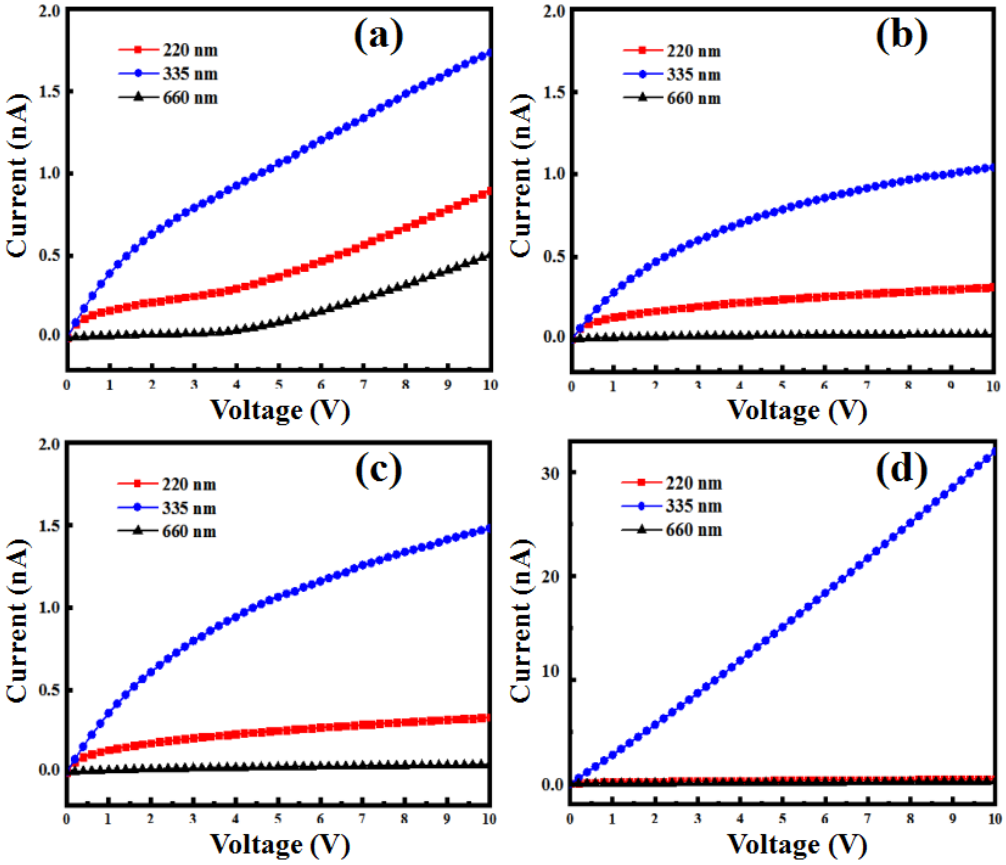

Figure 5-11 shows the photocurrent of TiO_2/diamond detectors with different thick TiO_2: (a) 2 nm; (b) 6 nm; (c) 12 nm; (d) 18 nm.

Figure 5-12 displays the spectral responsivity of TiO_2/diamond detector with TiO_2 thickness of 18 nm at 8 V. Two response peaks are centered at 225 nm (3 mA/W) and 290 nm (23.6 mA/W), which are different from those of pure diamond detectors and pure TiO_2 detectors. The response peak at 225 nm is caused by the response of diamond to ultraviolet

light, while the response peak at 290 nm comes from the ultraviolet response of TiO_2 film.

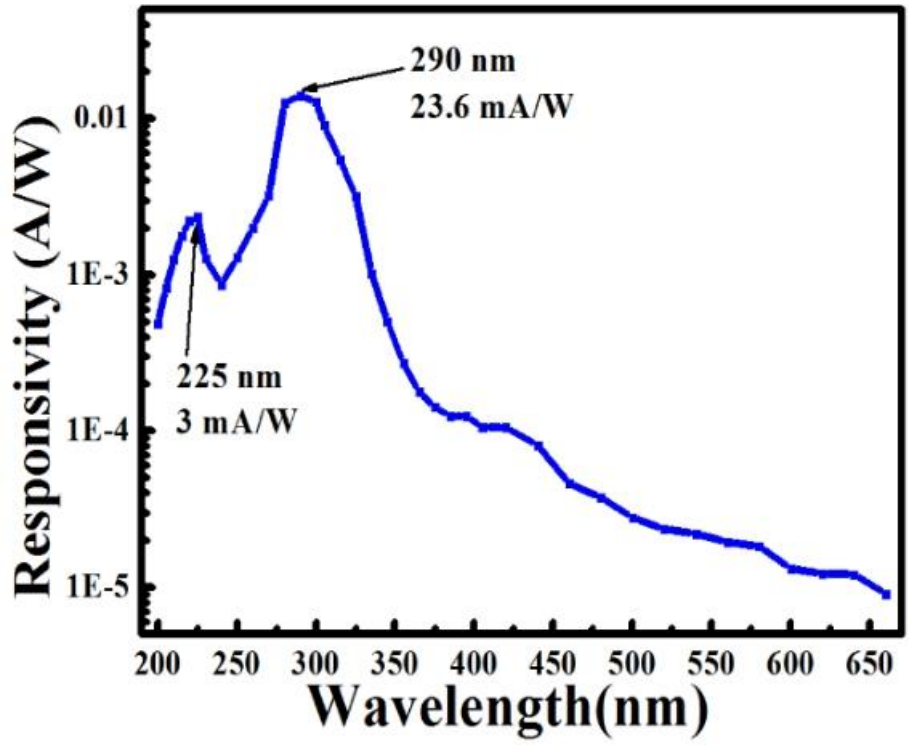

Figure 5-12 Spectral responsivity of TiO_2/diamond detector with 18 nm thick TiO_2 at 8 V.

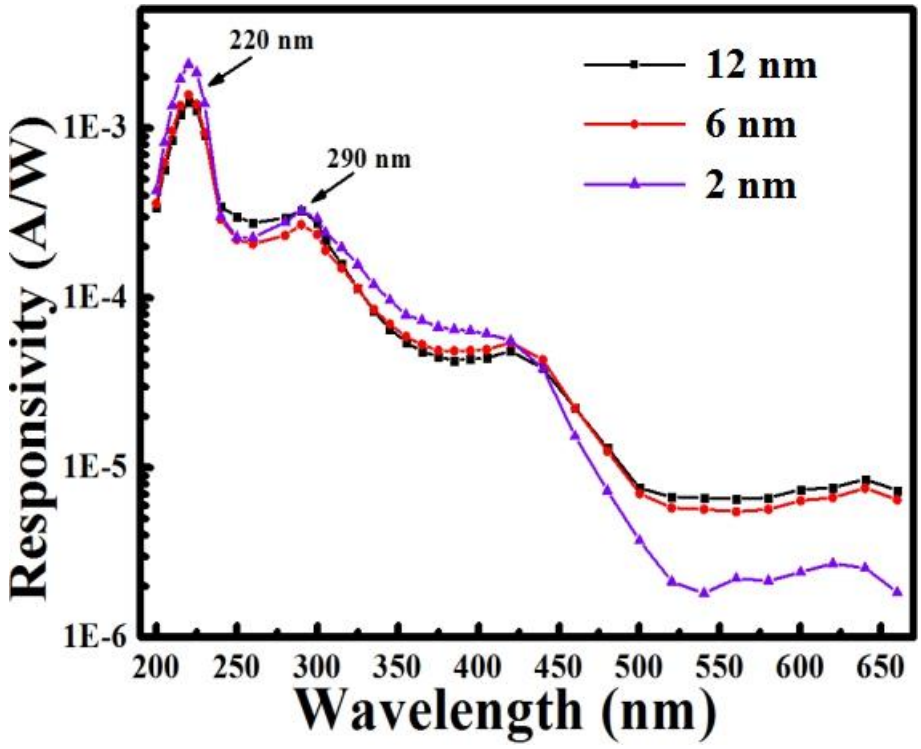

Figure 5-13 Spectral responsivity of TiO_2/diamond detector with 12 nm, 6 nm, and 2 nm thick TiO_2 at 8 V.

The variation of TiO_2 film thickness could affect the photo response behavior. Figure 5-13 shows the spectral response of TiO_2/diamond detectors with 12 nm, 6 nm, and 2 nm thick TiO_2 at 8 V. There are also two response peaks for all the three photodetectors centered at 220 nm and 290 nm. However, the responsivity at 290 nm is lower than that at 220 nm, which is different from TiO_2/diamond detector with 18 nm thick TiO_2. This could be ascribed to the film thickness, since ultra thin TiO_2 film can only absorb less UV light. Consequently, when TiO_2 film is thinner, its responsivity becomes lower.

Figure 5-14 shows the time response of the TiO_2/diamond detector at 20 V and 220 nm. It can be seen that the device has similar time response behavior when the thickness of TiO_2 film is 2, 6 and 12 nm. Under illumination, the current increases rapidly at first and then decreases to a stable value. When the light is removed, the current drops rapidly to its origin. The rising time of 2, 6 and 12 nm-TiO_2/diamond detectors is 30 ms, 20 ms and 60 ms, and the falling time is 600 ms, 200 ms and 350 ms, respectively. When the thickness of TiO_2 film is 18 nm, the device has different time response behavior. The current increases rapidly (30 ms) under illumination and then slowly over time. After shading, the current decreases rapidly (200 ms), then slowly, and can not return to the initial current value during testing. As the thickness increases, TiO_2 plays a dominant role in the light response, and the longer the response time is related to the defects.

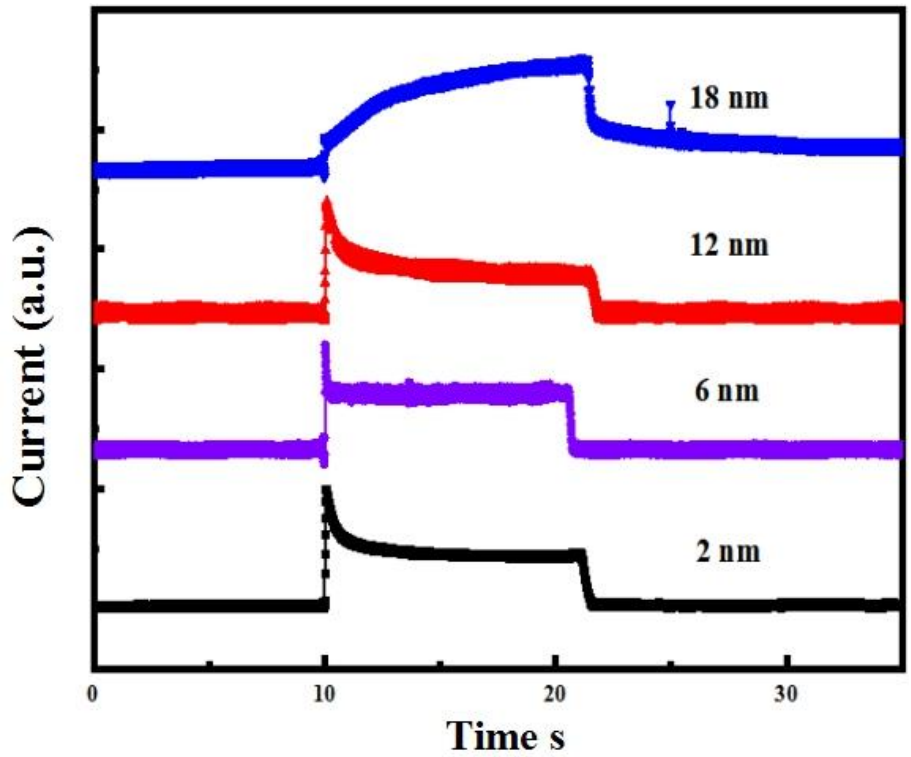

Figure 5-14 Time response of the TiO_2/diamond detector at 20 V and 220 nm.

5.4 Summary

In this paper, for the first time, the intrinsic single crystal diamond was combined with TiO_2 to fabricate TiO_2/diamond detector and its performance was studied. In the experiment, a photoconductive TiO_2/diamond detector was designed and fabricated. The dark current at 30 V was 2.6 pA, the response at 220 nm was 0.2 A/W, and the response at 340 nm was 0.048 A/W. Compared with pure diamond detectors, the responsivity in the ultraviolet region is improved. Next, the effect of film thickness on the performance of TiO_2/diamond ultraviolet detectors was studied. Titanium dioxide thin films with thickness of 2, 6, 12 and 18 nm were deposited on four regions of the same diamond sample surface, and four ultraviolet detectors with the same electrode parameters were prepared. The spectral response curves of the four detectors all show response peaks at 290 and 225 nm. Among them, 290 and 225 nm peaks are derived from the ultraviolet response of TiO_2 and diamond. When the film thickness is 12 nm or less, the responsivity of the detector at 225 nm is greater than that at 290 nm, which indicates that the response of the detector at this time is mainly diamond. The response enhancement of the structure of the titanium dioxide/diamond film to ultraviolet band is small. When the film thickness is 18 nm, the responsivity of the detector at 225 nm is less than that at 290 nm, indicating that the detection at this time. The device mainly responds to TiO_2, and the structure of TiO_2/diamond film enhances the photoresponse in ultraviolet band.

6 Preliminary exploration of diamond p-i-n photodiode

6.1 Introduction

With the development of social technology, Schottky barrier diodes, metal oxide semiconductor field effect transistors, p-n junction diodes and other high-power high-frequency electronic devices began to rapidly popularize. Compared with typical materials such as SiC and GaN, diamond has attracted much attention due to its high breakdown field, high thermal conductivity, high carrier mobility and low dielectric constant. In recent ten years, due to the difficulty of n-type doping technology, the research of diamond power devices mainly focuses on p-type Schottky barrier diodes and hydrogen-terminated field effect transistors [81-86]. In recent years, phosphorus (P) doping on (111) and (100) surfaces has been successfully realized by microwave plasma chemical vapor deposition (MPCVD). Since then, diamond p-i-n structures have been studied for deep ultraviolet light emitting diodes, vacuum switching devices and power electronic devices [87-89]. Of course, diamond p-i-n structure can also be applied to photodiodes.

Compared with N-doping on (111) orientation, (001) p-doping on (001) orientation diamond has better properties of metal-diamond crystals and electrical and optical thin films, which shows that the prospect of diamond electronic applications is closer to the actual market [90]. However, (001) there is a problem in oriented P-doped films, that is, the surface morphology is not flat and it is difficult to optimize [91]. In order to obtain a smooth surface, additional polishing processes are needed. This requires a relatively thick doped film. In the existing literature, (001) orientation doped methane concentration and growth temperature are low, resulting in a low growth rate of 0.2-2.5 um/h [91]. So it takes a long time to grow a thick film.

In this paper, the high growth rate of p-doped (001) oriented diamond films was achieved by using high methane concentration (>3.2%) and high growth temperature (1100 C). A diamond p-i-n photodiode was fabricated and characterized based on fast doping growth technology, which shows its potential application prospects.

6.2 Study on epitaxial growth of single crystal diamond

In order to prepare p-i-n structure, the surface of i layer should be smooth, so as to prepare for n layer epitaxial growth. Therefore, we studied the effect of growth process on the surface morphology of intrinsic epitaxial layer of single crystal diamond, including pressure, methane flow rate and temperature.

(1) Effect of pressure on surface morphology of intrinsic epitaxial layer

In order to study the effect of pressure on the surface morphology of intrinsic epitaxial layer, we keep the methane concentration, hydrogen flow rate, substrate temperature and growth time unchanged, and only change the pressure of the cavity. The parameters are shown in Table 6-1.

Table 6-1 Growth parameters for pressure study.

Sample ID	Pressure (kPa)	CH_4 (%)	H_2 (sccm)	Temperature (℃)	Time (h)
#1	8	6	500	1000	1
#2	11	6	500	1000	1
#3	14	6	500	1000	1
#4	16	6	500	1000	1

Figure 6-1 shows the surface morphology of diamond epitaxial layer grown under different chamber pressures. The surface of the sample under 8 kPa is black, but the surface under other pressure conditions is bright. At 8 kPa, the diamond surface did not realize epitaxial growth, but deposited a layer of black film, which could be wiped off by double cotton swabs. The composition of the film is also diamond by Raman spectroscopy. With the increase of chamber pressure to 11 kPa, the diamond surface appears dense bulging, which is a typical surface morphology of diamond epitaxy growth, indicating that diamond epitaxy growth has been achieved. When the pressure reaches 14 kPa, the surface becomes smooth, and the number of surface bulges decreases. When the pressure is further increased to 16 kPa, the surface becomes smoother, the bulge disappears and the black spots appear. Therefore, with the increase of pressure, the surface morphology can become smooth.

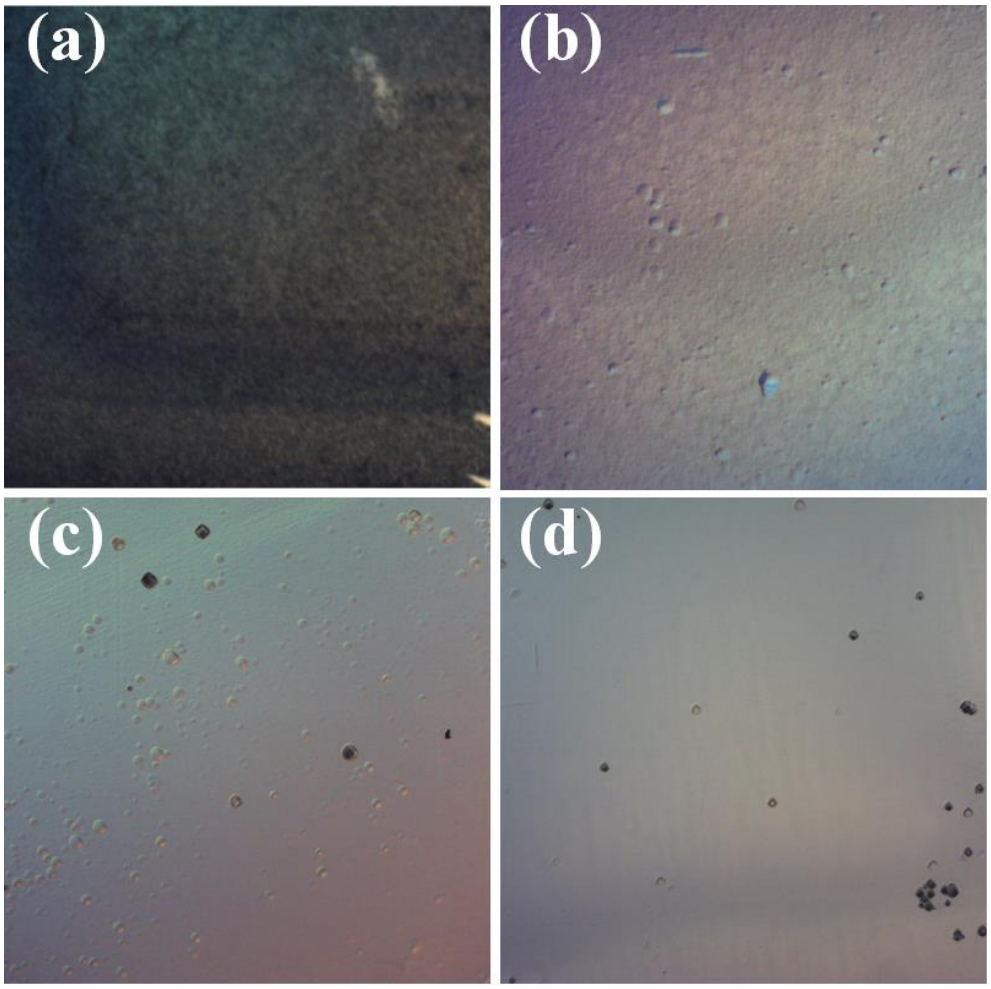

Figure 6-1 Surface morphology of diamond epitaxial layer grown under different chamber pressures: (a) 8 kPa, (b) 11 kPa, (c) 14 kPa, and (d) 16 kPa.

From the surface morphology of samples at 8 kPa and 11 kPa, it can be seen that large pressure is more conducive to the epitaxial growth of diamond. In the process of growth, we observed that the plasma sphere is larger at 8 kPa. During the process of increasing microwave power, the temperature of the substrate surface rises slowly. When the temperature rises to 1000 ℃ the microwave power reaches 4000 W, and the microwave power reacts on the plasma sphere, making it more dispersed and the center rises. In this case, the microwave power density on the substrate surface is low. The energy of hydrogen plasma is not enough to open the pentacarbon ring of diamond (2×1) to reconstruct dimer, so hydrocarbon groups in plasma atmosphere can not be embedded into diamond surface to realize epitaxy growth. In this way, hydrocarbon groups can only accumulate and nucleate at lower surface energy, and then small diamond particles can be gradually grown from the nucleation point. Moreover, because of the insufficient power density and slow growth process, these particles can not rapidly form continuous thin films.

At 11 kPa, the plasma sphere in the cavity is small and can aggregate onto the surface of the diamond substrate. During the process of increasing microwave, the substrate temperature rises rapidly. When the temperature rises to 1000 ℃, the microwave power is 2500 W. At this time, the plasma sphere is still relatively small and concentrated on the surface of the diamond substrate, and the center of the plasma sphere is closer to the surface of the sample than 8 kPa. In this case, both the power density and the energy of hydrocarbon groups on the surface of diamond substrates meet the conditions of diamond epitaxy growth, so the epitaxy growth of diamond films is realized. With the increase of the pressure, the plasma sphere is more concentrated on the surface of the diamond substrate, which is beneficial to the improvement of the surface morphology of the sample. In the follow-up study, the working pressure of the reaction chamber was set to be 16 kPa.

(2) Effect of methane concentration on surface morphology of intrinsic epitaxial layer

In order to study the effect of methane concentration on single crystal diamond epitaxial films, the hydrogen flow rate, chamber pressure, temperature and growth time is unchanged, and only change the methane concentration. Its parameters are shown in Table 6-2.

Table 6-2 Growth parameters for methane concentration study.

Sample ID	CH_4 (%)	Temperature (℃)	Pressure (kPa)	H_2 (sccm)	Time (h)
#1	4	1000	16	500	1
#2	6	1000	16	500	1
#3	8	1000	16	500	1
#4	10	1000	16	500	1

Fig. 6-6 shows the surface morphology of samples grown at different methane concentrations. When the methane concentration is 4 %, the stripe morphology appears on the surface. When the methane concentration is 6 %, the diamond surface is smooth and the stripe morphology decreases, but there are black spots. When the methane concentration is 8 %, the stripe morphology and the black spot morphology disappear, replaced by the drum morphology. When the methane concentration is 10 %, the drum becomes dense and sharp, and increases directly. In the process of growth, when hydrogen plasma opens the ring, the sixth carbon atom is supplemented by hydrocarbon groups. The growth of hydrogen plasma is directional, which makes the surface rough. However, due to the existence of surface migration process, the surface can be smoothed [92]. When the concentration of methane is

low (4 %), the hydrocarbon group concentration is low and grows in a specific direction preferentially. The growth rate of hydrocarbon group in other directions is slow because the concentration of hydrocarbon group is insufficient, thus forming a uniform stripe morphology. When the methane concentration increases to 6%, the concentration of hydrocarbon groups in the cavity increases, and there are enough hydrocarbon groups for surface migration, so the surface becomes smooth. The black shape is formed by etching the top of the hill on the surface. In the process of epitaxy, surface point defects grow faster and become hills. Later, hydrogen etches the top faster than it grows, making it darker. When the methane concentration is 8 %, the hydrogen etching rate at the top of the hill is less than the growth rate, so the bulging morphology is formed. With the further increase of methane concentration, the number of preferential nucleation points increases and the growth rate is faster, so the bulge becomes dense and the diameter becomes larger.

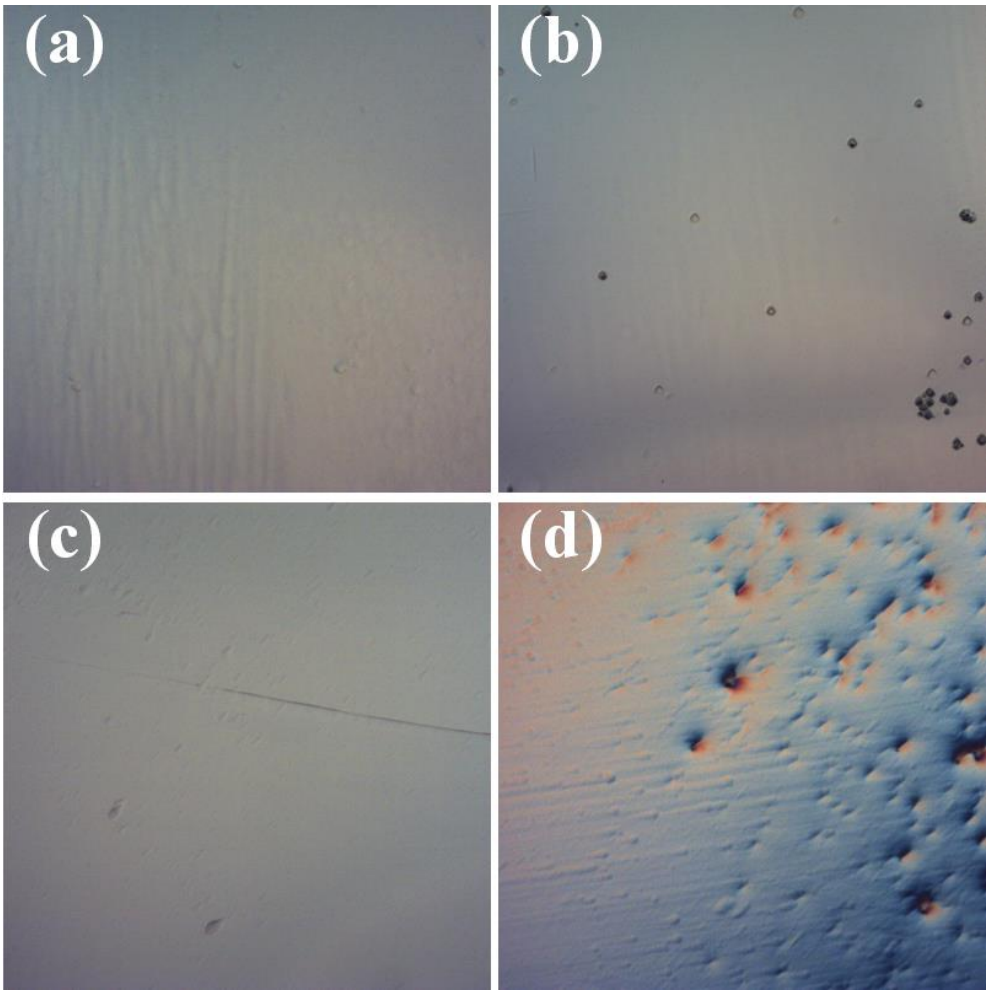

Figure 6-2 Surface morphology of diamond epitaxial layer grown under different methane concentration: (a) 4 %, (b) 6 %, (c) 8 %, and (d) 10 %.

(3) Effect of temperature on surface morphology of intrinsic epitaxial layer

In order to study the effect of temperature on surface morphology, the methane concentration, hydrogen flow rate, chamber pressure and growth time are unchanged, and only change the substrate temperature. The parameters are shown in Table 6-3.

Table 6-3 Growth parameters for temperature study.

Sample ID	Temperature (℃)	Pressure (kPa)	CH_4 (%)	H_2 (sccm)	Time (h)
#1	950	16	4	500	1
#2	1000	16	6	500	1
#3	1050	16	8	500	1
#4	1100	16	10	500	1

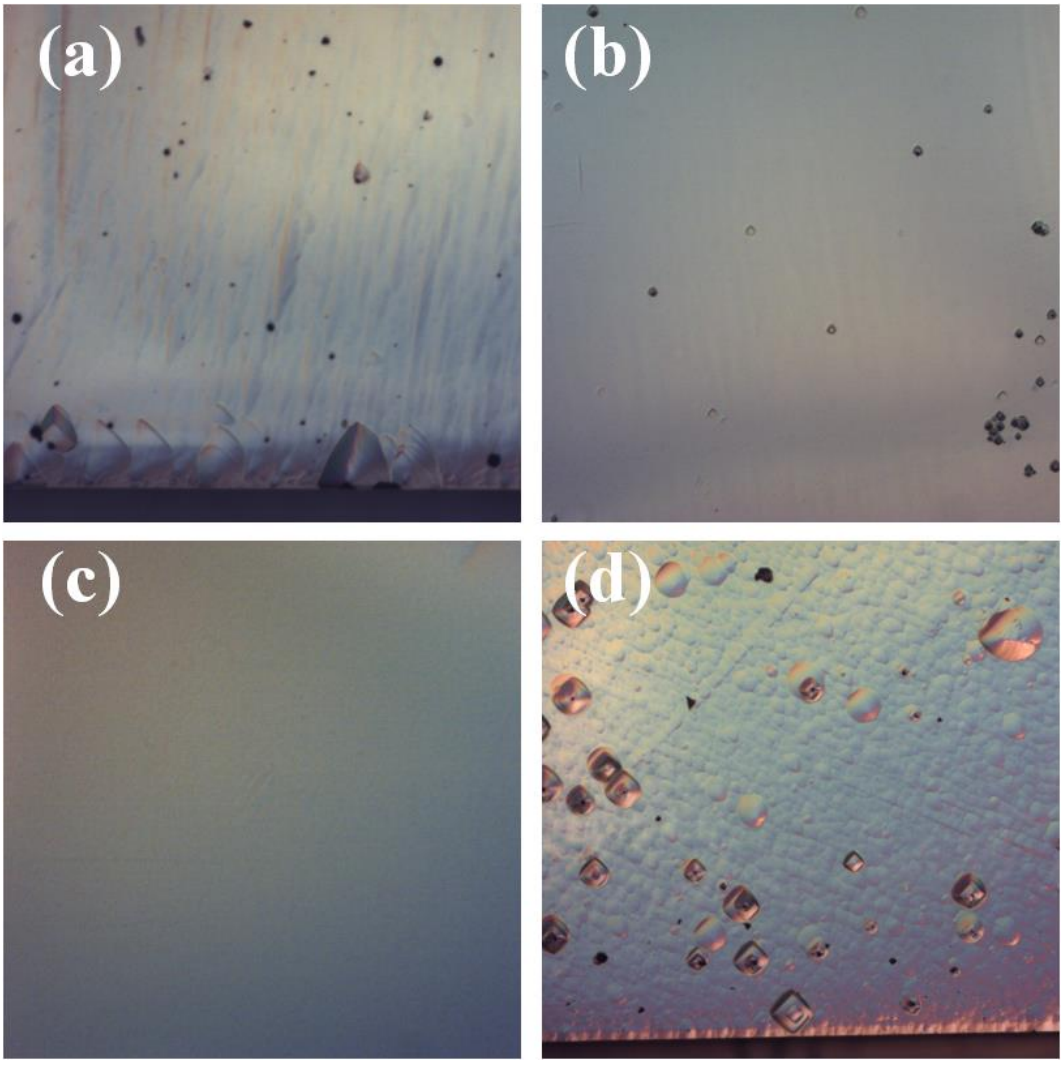

Figure 6-3 Surface morphology of diamond epitaxial layer grown under different temperature: (a) 950 ℃, (b) 1000 ℃, (c) 1050 ℃, and (d) 1100 ℃.

Figure 6-3 shows the surface morphology of diamond epitaxial films at different temperatures. At 950 ℃, the surface of the sample has stripes; at 1050 ℃, the surface is very smooth; at 1100 ℃, the surface appears pyramid. Surface migration requires sufficient energy. At low temperature (950 ℃), energy is not enough to migrate, so there are a lot of stripes on the surface. At 1000 ℃, the energy is higher and can be migrated, so the fringes are less. When the temperature is further increased, the growth rate of the sample surface increases, so that the point defects can be repaired to make the surface smooth. When the temperature is further increased to 1100 ℃, the growth rate is further increased, and the point defects can not be repaired, which will form a pyramid structure.

(4) Quality characterization of epitaxial intrinsic layer grown by optimized condition

Through the study of process parameters, we obtained the process of growing smooth diamond epitaxial layer: pressure 16 kPa, methane concentration 6%, temperature 1050 ℃, hydrogen flow 500 sccm, and the growth time is 1 h. Using this parameter, diamond epitaxial growth was carried out. The grown sample is shown in Figure 6-4. It can be seen that the surface is very smooth.

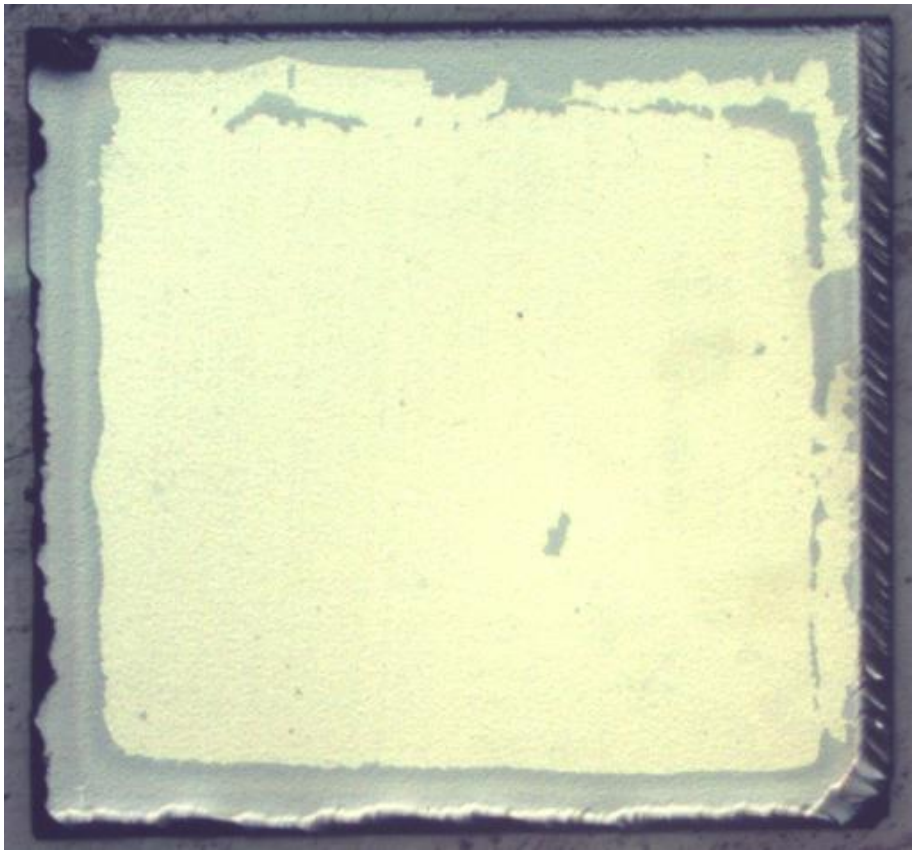

Figure 6-4 Optical image of diamond grown with optimized condition.

Figure 6-5 gives the Raman spectrum of the epitaxial intrinsic diamond sample. There is

only one single sharp peak located 1332.9 cm^{-1}, indicating the existence of diamond phase. Additionally, the half-peak width is 3 cm^{-1}, indicating that the quality of the diamond is acceptable.

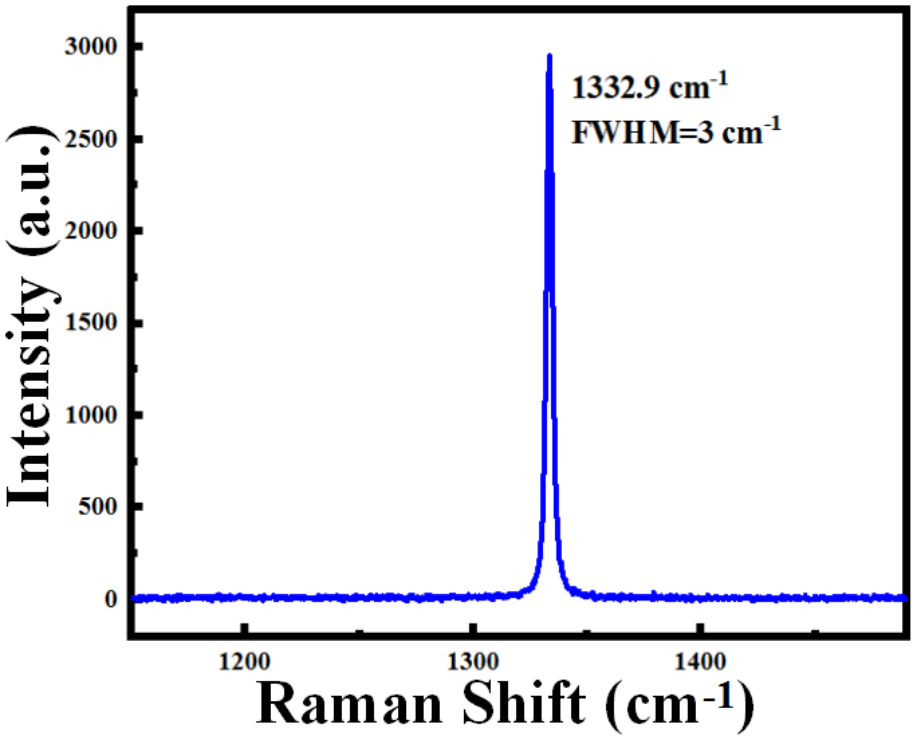

Figure 6-5 Raman spectrum of diamond grown with optimized condition.

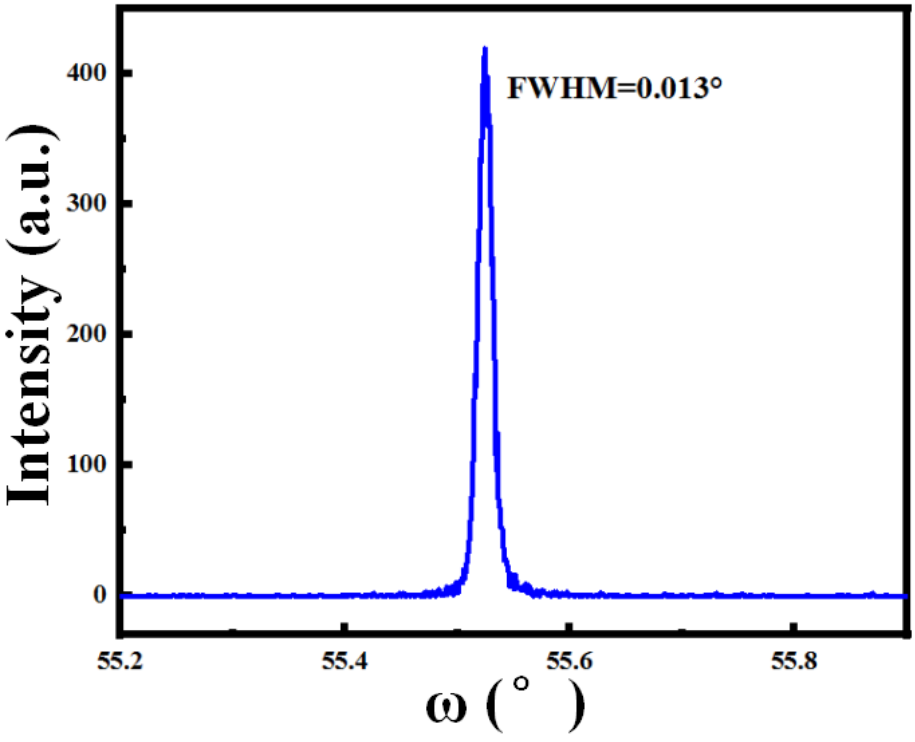

Figure 6-6 XRD spectrum of diamond grown with optimized condition.

Figure 6-6 shows the XRD rocking curve of diamond (400) orientation. A sharp peak can

be observed in the figure, which is a characteristic peak for diamond (100) surface. This indicates that the growth is successful to remain the origin orientation. The half-peak width of is about 0.0132 degree, indicating a good crystal quality.

Figure 6-7 gives PL spectrum of the epitaxial diamond, and the emission peak near 235 nm can be clearly observed. The emission peak near 235 nm is free exciton peak, which can only be observed in high quality diamond samples. The PL spectrum of commercialized high quality single crystal diamond substrates is also shown. The luminescence peak can also be observed at 235 nm. Compared with commercial high-quality single crystal diamond substrates, the emission peak and intensity at 250-400 nm band are reduced, which indicates that the quality of single crystal diamond substrates is better.

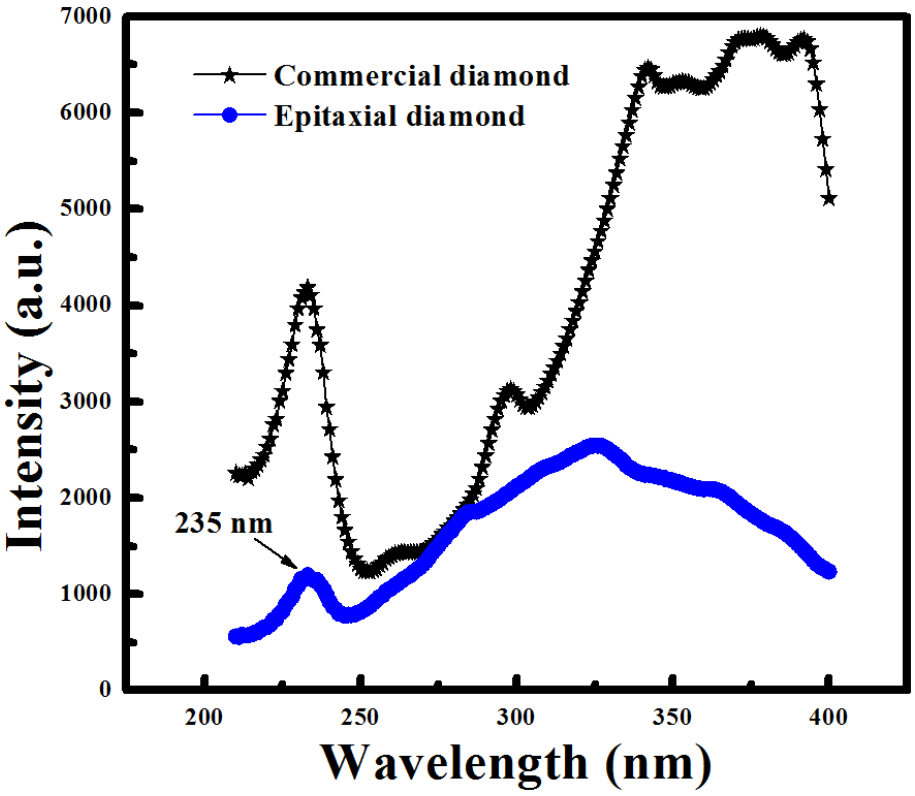

Figure 6-7 PL spectra of diamond grown with optimized condition and commercial diamond.

6.3 N-type doping of (100)-oriented single crystal diamond

N-type doping of diamond is mainly realized by phosphorus doping. Compared with (111)-oriented phosphorus-doping, the efficiency of phosphorus-doping in (100) direction is low. To this end, we have continuously optimized the process and improved the equipment, and finally successfully realized (100)-oriented phosphorus doping. The doping concentration of phosphorus is mainly related to two factors: temperature and

phosphorus/carbon ratio.

(1) Effect of temperature on doping concentration

The hydrogen flow rate of 500 sccm, methane flow rate of 40 sccm and phosphine flow rate of 100 sccm were maintained unchanged, and the doping growth was carried out for 30 minutes in the temperature range of 1000-1100 ℃. Figure 6-8 shows the surface morphology of phosphorus-doped diamond grown at different temperatures.

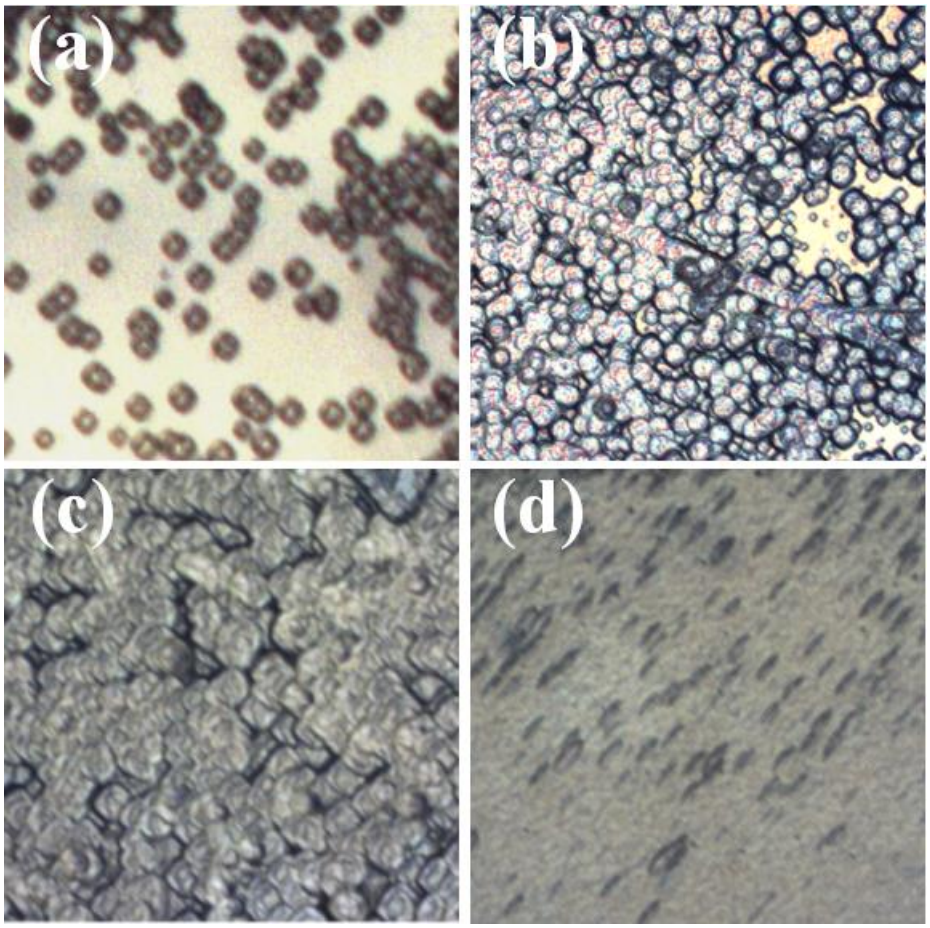

Figure 6-8 Optical image of phosphorus-doped diamond grown at different temperatures: (a) 1000 ℃, (b) 1030 ℃, (c) 1060 ℃, and (d) 1100 ℃.

When the growth temperature is 1000 ℃, the sample surface is composed of smooth surface and dispersed particles. When the temperature increases to 1030 ℃, the surface microparticles become more and connect with each other, covering most of the surface, and only a few smooth surfaces are exposed. When the temperature increases to 1060 ℃, all surfaces are covered by micro-particles, and the degree of coalescence of micro-particles increases. When the temperature continues to increase to 1100 ℃, there is no micro-particle morphology on the surface, but fine step morphology. The micro-structure is given by Figure 6-9. This is because at low temperatures, phosphorus atoms aggregate on the surface, which

will cause diamond nucleation, and then grow larger, resulting in a lot of micro-particles on the surface. With the increase of temperature, the phosphorus atoms gradually disperse, so the number of micro-particles will increase, and the growth rate will increase with the increase of temperature, so that the transverse coalescence of micro-particles will be accelerated, and even coalesced into continuous films. At high temperature (1100 ℃), phosphorus atoms can be uniformly dispersed on the surface, and the growth mode of the surface becomes step growth.

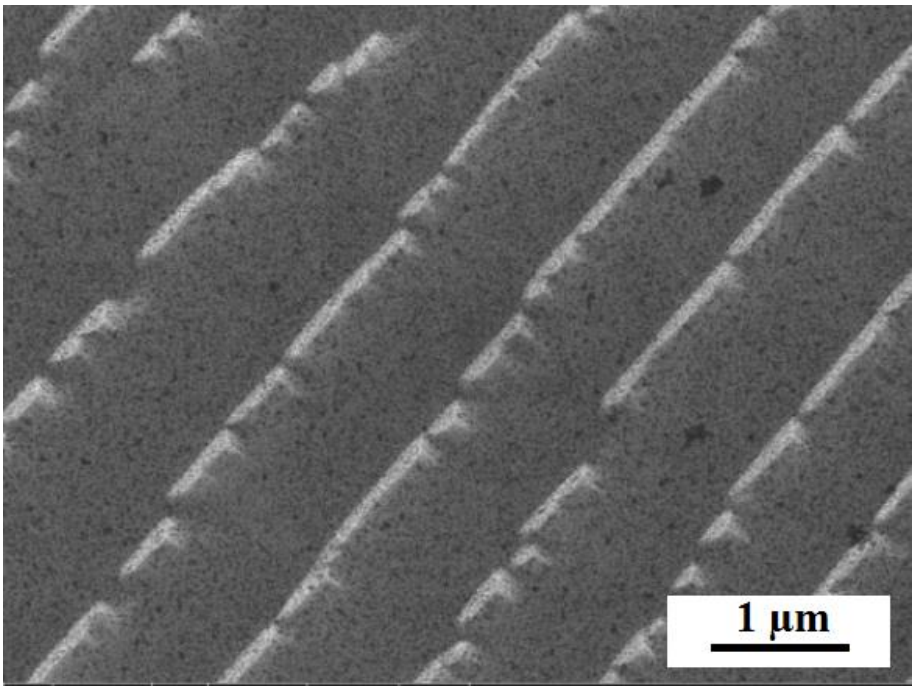

Figure 6-9 SEM image of diamond grown at 1100 ℃.

The doping concentration of phosphorus atoms needs to be measured by secondary ion mass spectrometer (SIMS). Figure 6-10 shows the SIMS results of phosphorus doping concentration at growth temperature of 1060 ℃ and 1100 ℃. The doping concentration of phosphorus is 2×10^{17} cm^{-3} at the growth temperature of 1060 ℃, and 4×10^{17} cm^{-3} at the growth temperature of 1100 ℃. The results show that the higher the temperature is, the higher the phosphorus doping concentration is. This is because the radius of phosphorus atom is larger than that of carbon atom, the solid solubility of diamond is lower, and precipitation phenomenon exists. The growth rate of diamond at 1060 ℃ is lower than that of 1100 ℃, and the phosphorus precipitation rate is higher, resulting in the doping concentration of diamond is lower than that of phosphorus doping at 1100 ℃.

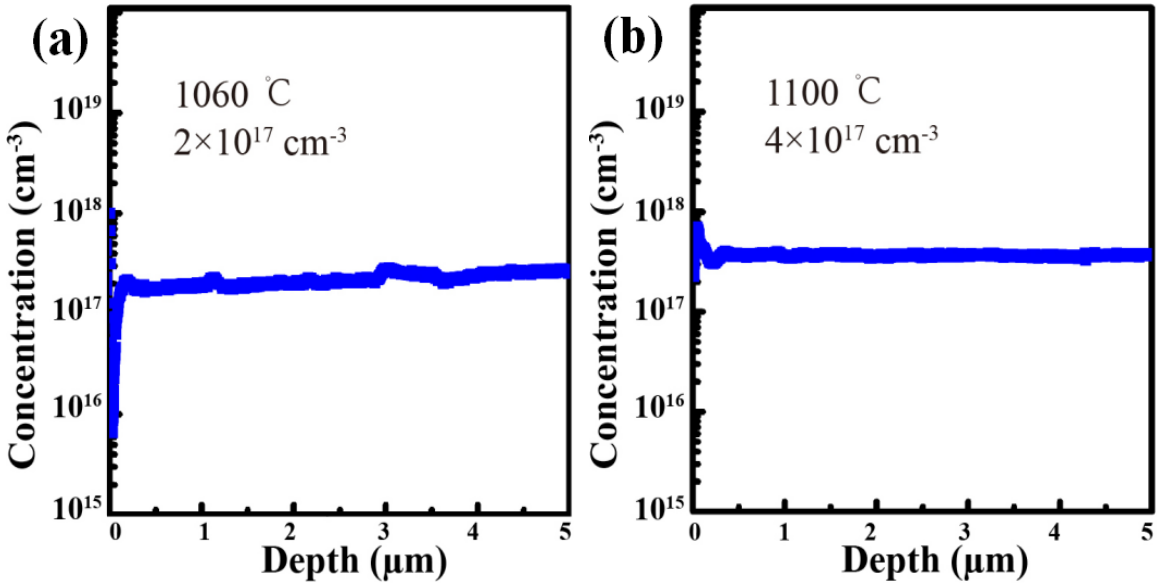

Figure 6-10 SIMS results of phosphorus doping concentration at (a) 1060 and (b) 1100 ℃ growth temperatures.

(2) Effect of methane concentration on doping concentration

The C/P ratio in the growth atmosphere is also a key factor affecting the doping concentration. In order to study the effect of methane concentration on the surface morphology and doping concentration of phosphorus-doped diamond, we maintained hydrogen flow rate of 500 sccm, phosphorus flow rate of 100 sccm, substrate temperature of 1100 ℃, growth for 30 minutes at 3.2 %, 4.7%, 6.25%, 7.7% and 9.1% methane concentration.

Figure 6-11 gives SIMS results of phosphorus doping concentration of doped growth samples at different methane concentrations. It can be seen from the results that the concentration of methane has a great influence on the phosphorus doping concentration. At the concentration of methane of 9.1%, 7.7%, 6.25%, 4.7% and 3.2 %, the phosphorus doping concentration is 1×10^{17} cm^{-3}, 2×10^{17} cm^{-3}, 3×10^{17} cm^{-3}, 1×10^{18} cm^{-3}, and 1.5×10^{18} cm^{-3}, respectively. This indicates that the phosphorus doping concentration increases with the decrease of methane concentration. Therefore, in order to achieve higher doping concentration, the methane flow rate can be further optimized.

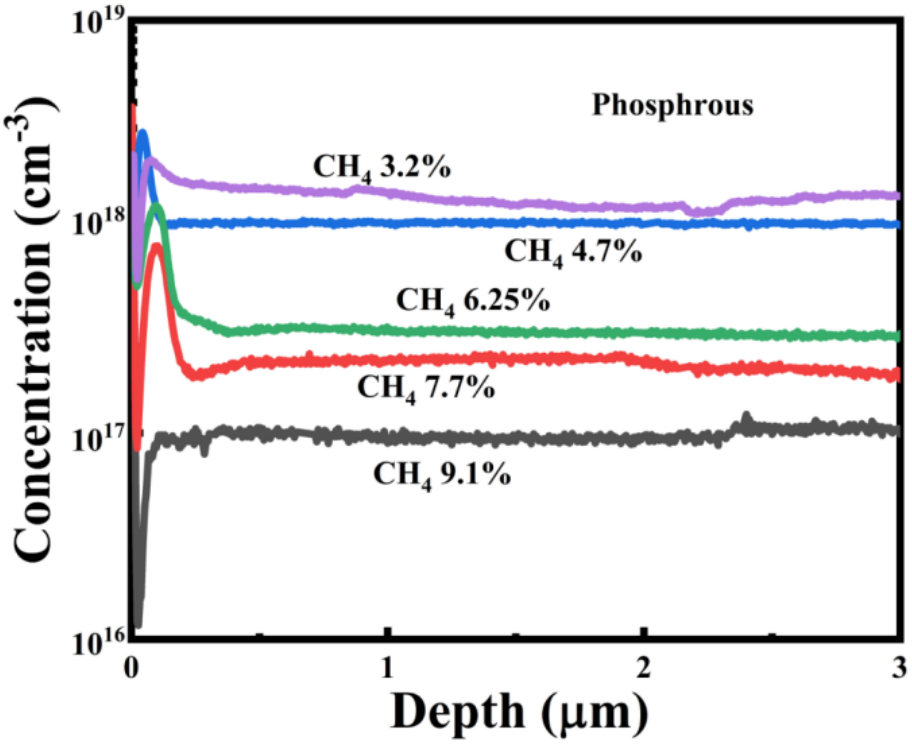

Figure 6-11 SIMS profiles of P-doped diamond films with CH_4 concentration varying.

Figure 6-12(a) shows the cross section of the doped sample at 4.7% methane concentration. A clear boundary can be observed in the SEM image due to the difference in conductivity between the phosphorus-doped film and the intrinsic diamond substrate. The white area is diamond substrate and the black filament area is epitaxial phosphorus doped film. The thickness of the phosphorus-doped film is about 10.14 μm. The growth rate of the phosphorus-doped film reaches 20.28 μm/h because the growth time is 30 min. The growth rate of phosphorus doping is much higher than that in other literatures [91,93,94]. Using the same method, the growth rate of other methane concentrations can be calculated. Figure 6-12(b) shows the variation of doping growth rate with methane concentration. It can be seen that the growth rate increases with the increase of CH_4 concentration. When the concentration of CH_4 was 9.1%, the growth rate even reached 54.5 μm/h. However, the concentration of phosphorus doping is low at this time, which is only 1×10^{17} cm^{-3}. In order to obtain high doping concentration and high growth rate at the same time, the concentration of methane and phosphane can be increased simultaneously.

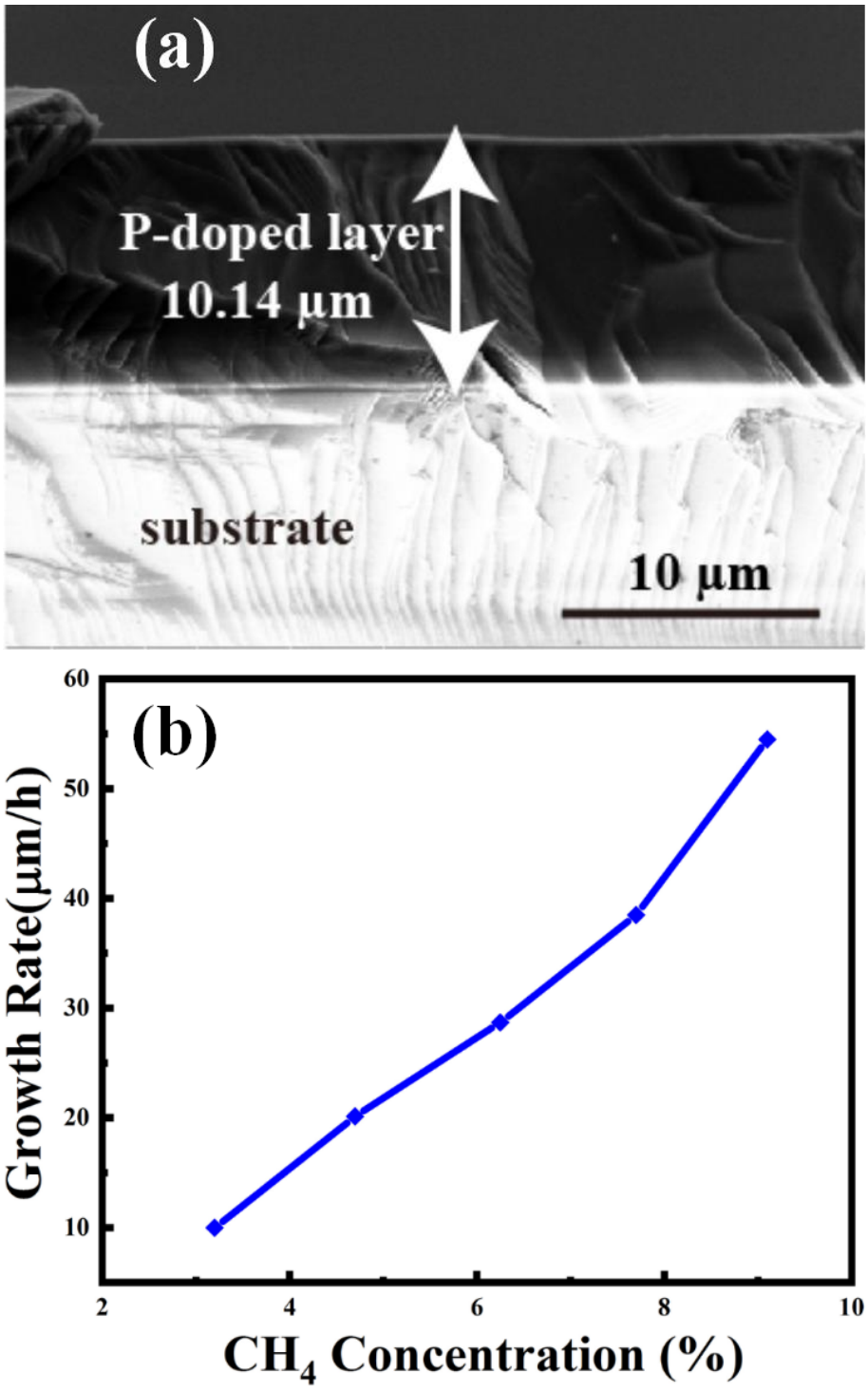

Figure 6-12 (a) Cross section of the doped sample at 4.7% methane concentration. (b) Doping growth rate as a function of CH_4 Concentration.

6.4 Investigation of (100)-oriented diamond p-i-n photodiode

Based on the success of fast doping technique, a (001)-oriented diamond p-i-n junction diode was fabricated, and the schematic is shown in Figure 6-13. The p-type layer is 300 µm

thick HPHT IIb type (001)-orientated single crystal diamond substrate with a boron concentration of 3×10^{19} cm^{-3}. The intrinsic layer and P-doped n-type layer grown by MPCVD method have thicknesses about 400 nm and 500 nm, respectively. The n-type layer growth conditions are the same with that of the CH_4 4.7 % sample. Therefore, the P concentration is about 1×10^{18} cm^{-3}. Due to the high growth rate (~20.28 μm/h), the doping process was finished in 2 min. The cathode and anode electrodes were formed on n top layer and p bottom layer respectively using Ti and Pd. To form a better ohmic contact, the sample was annealed at 500 ℃ for 30min in vacuum.

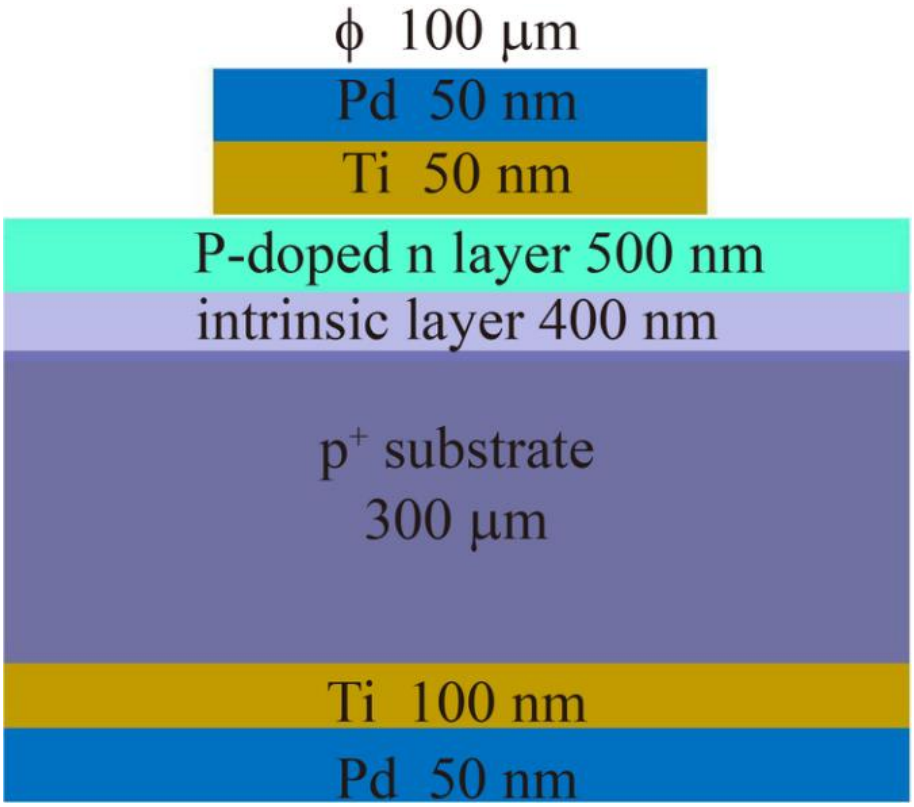

Figure 6-13 Schematic diagram of the p-i-n photodiode structure

Figure 6-14 shows the IV characteristics of diamond p-i-n junction diodes at room temperature. It can be seen from the figure that the diode has obvious rectification characteristics. At 14.5 V, the forward current density is 5812 A/cm^2, while at -14.5 V, the reverse current density is 56 mA/cm^2. Therefore, the rectification ratio of the diode at 14.5 V is about 1×10^5. The leakage current density of the p-i-n junction diode is higher and the rectification ratio is lower. This is because the intrinsic layer is thinner and the reverse-biased carrier is easier to pass through the intrinsic layer, which increases the leakage current density. Therefore, the thickness of intrinsic layer should be selected according to the device use.

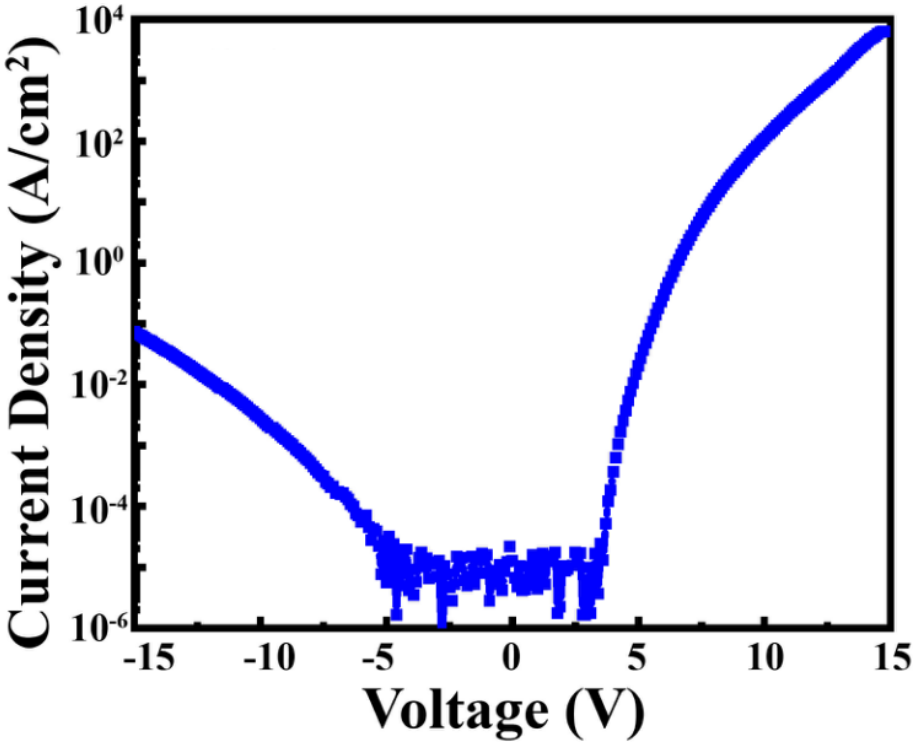

Figure 6-14 Current density as a function of the bias voltage.

Figure 6-15 shows the capacitive voltage (C-V) characteristics of diamond p-i-n diodes at room temperature and 10 kHz. In the range of -5V to 2V, the capacitance value is constant, and its value is 940fF, which indicates that the eigen layer has been exhausted. Because the calculation formula of capacitance is $C=A\varepsilon_{diamond}\varepsilon_0/W$, the calculation result of depletion zone width W is 420 nanometers. In the $1/C^2$-V characteristic, $1/C^2$ decreases rapidly in the range of 2.5 V to 5 V, which indicates that the depletion width of layer I shrinks. The built-in potential Vbi of the device is 4.74 eV and the acceptor concentration of the intrinsic layer is 4.9×10^{16} cm^{-3} by fitting the linear part of the device and combining formula (3-5) and (3-6). Since the activation energy level of boron is 0.37 eV and that of phosphorus is 0.57 eV, the theoretical value of built-in potential difference is V_{bi}= (5.5-0.37-0.57) eV=4.56 eV. The calculated value of the p-i-n diode in this study is close to the theoretical value and reasonable. The calculated values of the acceptor concentration are relatively large, which indicates that the boron concentration in the intrinsic thin films is higher than that of the unintentionally doped ones, which is also one of the reasons for the high reverse current density and low rectification ratio.

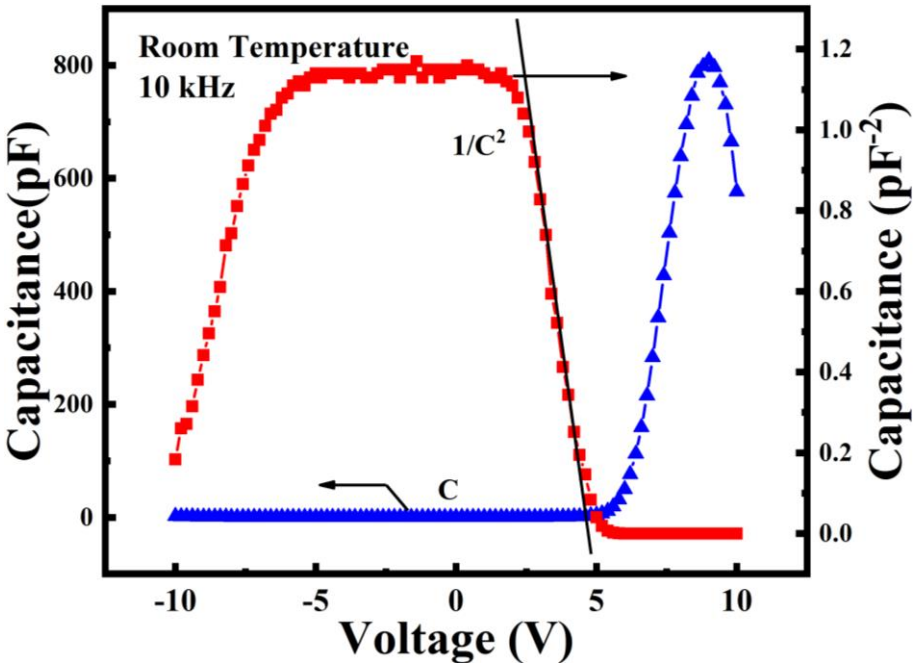

Figure 6-15 Capacitance-voltage characteristics of the p-i-n diode.

Figure 6-16 shows the IV characteristics of diamond p-i-n junction photodiodes. It can be found that the photocurrent of the device is larger than that of the dark current when the light intensity is 210 nm of 0.366 W/mm^2. At reverse bias of 5 V, the dark current of the device is 35.2 nA and the photocurrent is 1.9 μA, so the light-dark current ratio is 54 and the net photocurrent reaches 1.865 μA.

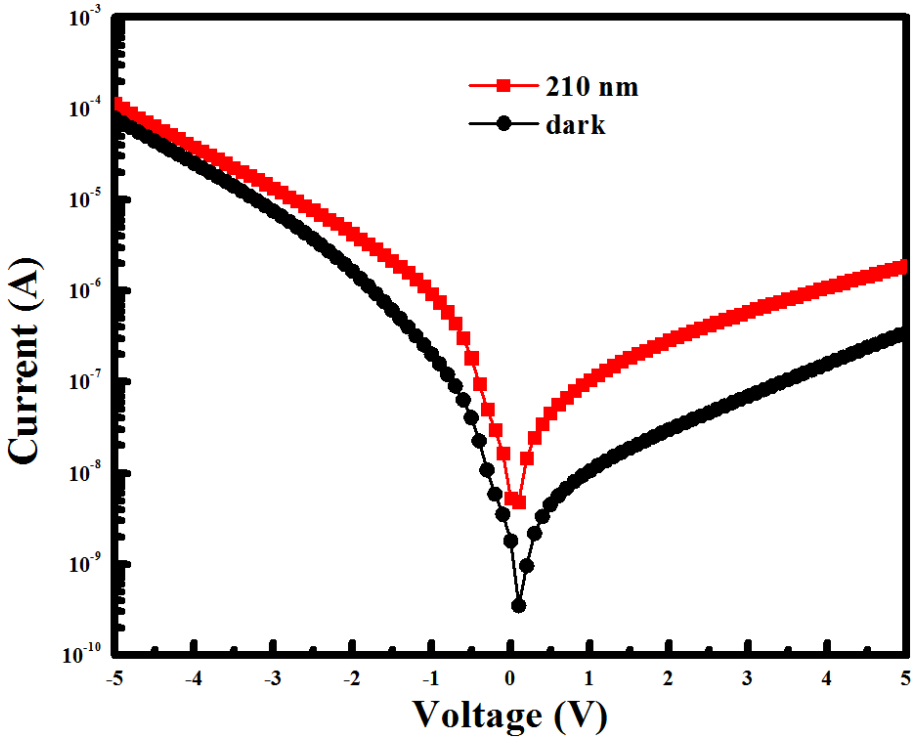

Figure 6-16 IV characteristics of diamond p-i-n junction photodiode.

Generally speaking, the p-i-n junction photodiode works in the reverse bias state, so we study the spectral response under the reverse bias. Figure 6-17 shows the spectral response curve of diamond p-i-n junction photodiode with a bias of 5V. The device has good spectral selectivity, with a response of 730 A/W at 215 nm and 0.52 A/W at 400 nm, so its UV/visible suppression ratio of 215 nm/400 nm is 1.4×10^3.

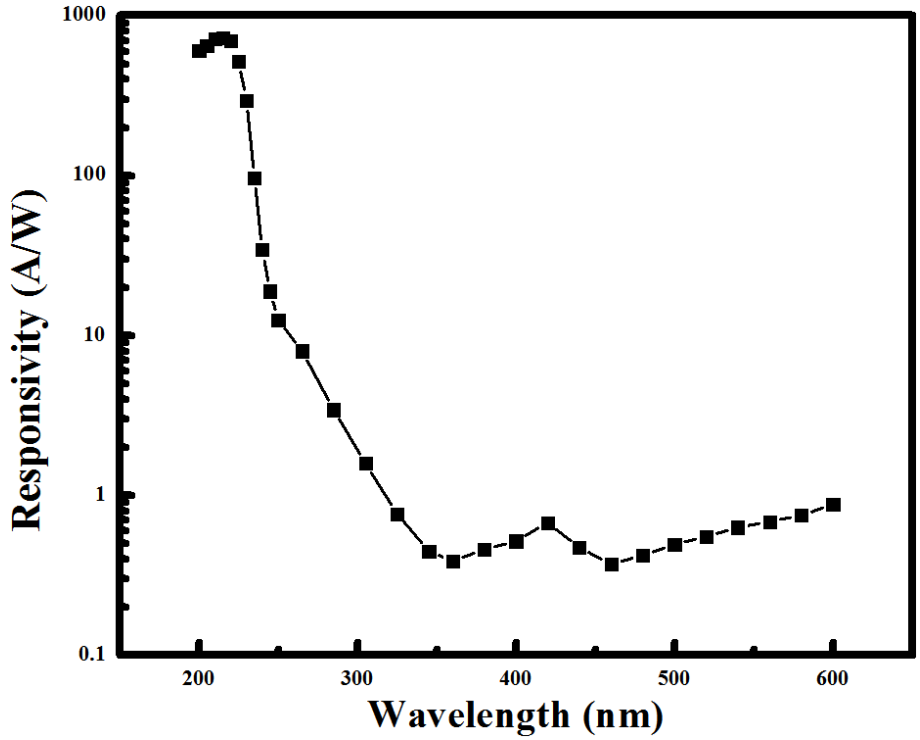

Figure 6-17 Spectral response of diamond p-i-n junction photodiode with a bias of 5V.

Figure 6-18 shows the relationship between current and time under 1V reverse bias of diamond p-i-n junction photodiode. The wavelength of incident light is 215 nm. When the illumination is turned on, the current of the device increases slowly and does not reach the saturation value within 10 seconds. When the illumination is removed, the current of the device decreases slowly and does not reach the initial current value within 200 seconds. The time response curve shows that the device has a very serious persistent photoconductivity effect. This is because there is a large acceptor concentration in the intrinsic layer. Once an electron-hole pair is generated under light, most of the electrons will recombine with the hole, so the photocurrent can only rise slowly. When the light is withdrawn, the electrons captured by the acceptor are released slowly, which makes the photocurrent of the device decrease slowly. Therefore, it is necessary to further optimize the process to inhibit the unintentionally doped boron concentration.

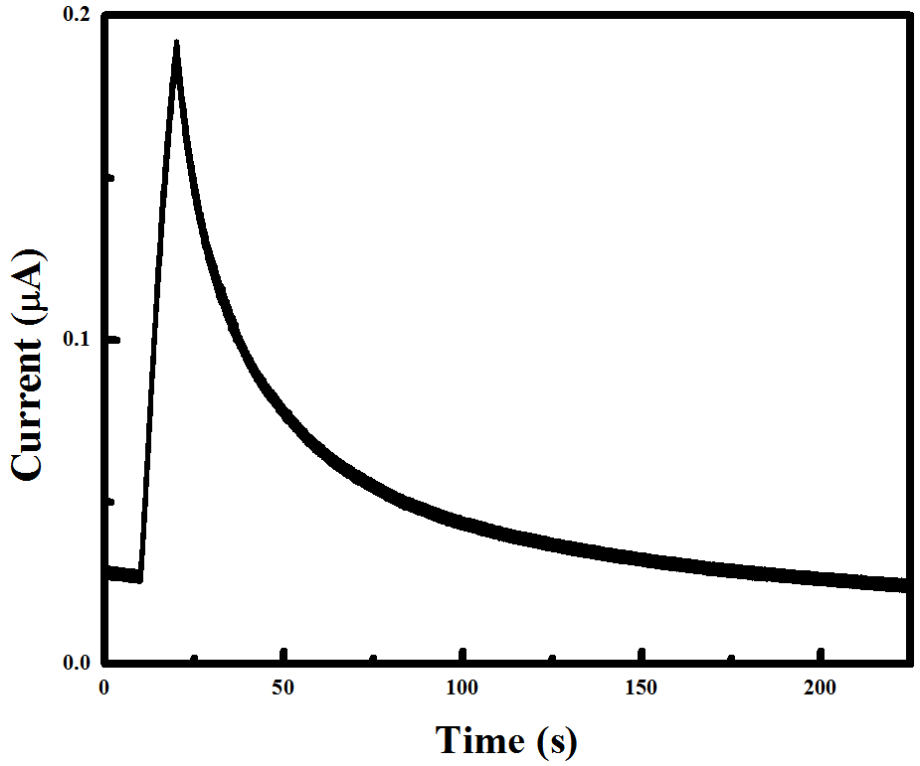

Figure 6-18 Time response of the diamond p-i-n junction photodiode under 1 V reverse bias.

6.5 Summary

In the experiment, the intrinsic single crystal diamond epitaxy process was studied firstly. By adjusting the chamber pressure, methane concentration and temperature, the technological conditions for the growth of smooth epitaxy layer surface were obtained as follows: chamber pressure 16 kPa, methane concentration 6%, temperature 1050 C, hydrogen flow 500 sccm. The Raman half-peak width and XRD half-peak width of the diamond epitaxy films prepared by this process are 3 cm^{-1} and 0.0132 ° respectively, and 235 nm free exciton peaks can be clearly observed. Next, the factors affecting n-type phosphorus doping in single crystal diamond were studied. The results show that the phosphorus doping concentration increases with the increase of growth temperature, and decreases with the decrease of methane concentration. Finally, diamond p-i-n junction photodiodes were fabricated based on high quality intrinsic epitaxy and n-type doping rapid growth process. Under light, the device has obvious photoelectric response. At 5 V, the dark current of the rejection ratio at 215 nm/400 nm is 1.4×10^{3}. The acceptor concentration introduced by non-intentional boron doping in the intrinsic layer is higher, which results in a slower response speed.

7 Conclusion and outlook

7.1 Conclusion

Diamond materials have excellent optoelectronic properties, and have high application potential in the direction of ultraviolet detectors. In this paper, the improvement of the responsivity of single crystal diamond UV photodetector is studied.

(1) diamond UV photodetector with photocurrent gain were prepared, and the mechanism of the photocurrent gain was investigated. When the bias voltage is larger than the open voltage, the photogenerated electrons accumulated near the positive electrode/diamond interface can tunnel through the barrier and inject into the electrode, thus generating photocurrent gain. The turn-on voltage is related to the concentration of photoelectrons. The higher the concentration, the lower the turn-on voltage. Due to the existence of photocurrent gain in diamond ultraviolet photodetectors, the responsivity can be enhanced. When the bias voltage is less than the open voltage, the wavelength responsivity of 210 nm is only 4.29 mA/W; when the bias voltage is larger than the open voltage, the responsivity increases rapidly to 51 mA/W. When the voltage is further increased, the avalanche effect occurs, then the photocurrent increases 10 times rapidly, and the responsivity reaches 1.18 A/W at 50 V.

(2) A bottom-up method for fabricating three-dimensional diamond grooved ultraviolet detectors is proposed for the first time. In the experiment, the metal interdigital electrode was fabricated on the surface of the diamond epitaxial layer, and then the grooved three-dimensional ultraviolet detector was obtained by selective growth in the diamond area which was not covered by metal. The detector is a photoconductive detector with dark current of 4.74 μA at 5V, responsivity of 9.36 A/W at 220 nm and UV/visible light rejection ratio of 10^3. To solve the problem of large dark current and slow response of the photoconductive detector, we fabricated photovoltaic three-dimensional ultraviolet detectors by bottom-up method. The dark current of the photoconductive detector is five orders of magnitude lower than that of the photoconductive detector, and the decay time is 590 ms, which is much shorter than the response time of the photoconductive detector.

(3) Low-dimensional materials have unique physical properties. In this chapter, the design of Q1D structure is applied to single crystal diamond UV photodetectors for the first time,

and its performance is characterized. Q1D diamond UV detector were obtained by etching diamond strips on the surface of diamond and setting the interdigital electrodes perpendicular to the direction of diamond strips. Because of the etching defects, the as-fabricated detectors have better performance than planar detectors only when the electrode spacing is large, and the photocurrent of the detectors is increased by 14.6%. The surface defects were repaired by diamond secondary epitaxy technology, and the Q1D structure detectors were fabricated again. The photocurrent of the repaired detector is larger than that of the planar structure. When the distance between the electrodes is 30 μm, the photocurrent even increases by 106%. In addition, the responsivity, UV/visible rejection ratio and transient response performance of Q1D structure detector are better than those of planar structure detector with the same electrode spacing. The experimental results show that the performance of diamond UV photodetectors can be effectively improved by combining QiD structure design with secondary epitaxy surface defect repair.

(4) The intrinsic single crystal diamond was combined with TiO_2 to fabricate TiO_2/diamond detector and its performance was studied. In the experiment, a photoconductive TiO_2/diamond detector was designed and fabricated. The dark current at 30 V was 2.6 pA, the response at 220 nm was 0.2 A/W, and the response at 340 nm was 0.048 A/W. Compared with pure diamond detectors, the responsivity in the ultraviolet region is improved. Next, the effect of film thickness on the performance of TiO_2/diamond ultraviolet detectors was studied. Titanium dioxide thin films with thickness of 2, 6, 12 and 18 nm were deposited on four regions of the same diamond sample surface, and four ultraviolet detectors with the same electrode parameters were prepared. The spectral response curves of the four detectors all show response peaks at 290 and 225 nm. Among them, 290 and 225 nm peaks are derived from the ultraviolet response of TiO_2 and diamond. When the film thickness is 12 nm or less, the responsivity of the detector at 225 nm is greater than that at 290 nm, which indicates that the response of the detector at this time is mainly diamond. The response enhancement of the structure of the titanium dioxide/diamond film to ultraviolet band is small. When the film thickness is 18 nm, the responsivity of the detector at 225 nm is less than that at 290 nm, indicating that the detection at this time. The device mainly responds to TiO_2, and the structure of TiO_2/diamond film enhances the photoresponse in ultraviolet band.

(5) A (100)-oriented diamond p-i-n photodiode was investigated in this paper. The intrinsic single crystal diamond epitaxial process was studied firstly. By adjusting the chamber pressure, methane concentration and temperature, the technological conditions for

the growth of smooth epitaxy layer surface were obtained as follows: chamber pressure 16 kPa, methane concentration 6%, temperature 1050 C, hydrogen flow 500 sccm. The Raman half-peak width and XRD half-peak width of the diamond epitaxy films prepared by this process are 3 cm^{-1} and 0.0132 ° respectively, and 235 nm free exciton peaks can be clearly observed. Next, the factors affecting n-type phosphorus doping in single crystal diamond were studied. The results show that the phosphorus doping concentration increases with the increase of growth temperature, and decreases with the decrease of methane concentration. Finally, diamond p-i-n junction photodiodes were fabricated based on high quality intrinsic epitaxy and n-type doping rapid growth process. Under light, the device has obvious photoelectric response. At 5 V, the dark current of the rejection ratio at 215 nm/400 nm is 1.4×10^{3}. The acceptor concentration introduced by non-intentional boron doping in the intrinsic layer is higher, which results in a slower response speed.

7.2 Outlook

In this paper, the research of avalanche photodetectors, three-dimensional structure detectors, quasi-one-dimensional structure detectors, TiO_2/diamond heterojunction detectors and diamond p-i-n photodiodes is mainly focused on the improvement of diamond responsivity. There are still many tasks that can be carried out in detail. In addition, some assumptions have not yet been realized.

(1) The mechanism of photocurrent gain and the origin of avalanche effect need further study. In this paper, photoelectric current gain and avalanche effect are observed in back-to-back Schottky junction detectors, but it is not clear whether they can be observed in photoconductive detectors and single Schottky junction detectors.

(2) The photoconductive detector fabricated by bottom-up method has high dark current, high responsiveness and slow response speed, while the photovoltaic detector has low dark current and fast response speed, but low responsiveness. Therefore, appropriate design can be adopted to combine the advantages of both.

(3) In the research of quasi-one-dimensional structure detector, the influence of width and height of diamond strip on detector performance can be further studied. In addition, drawing on the idea that other materials have high responsiveness in nanowire dimension, the dimension of diamond bars can be further approached to one-dimensional nanowires to improve the responsiveness of detectors.

(4) In the research of diamond p-i-n photodiodes, the high concentration of unintentional

doping in the intrinsic layer leads to high dark current and slow response. Therefore, the acceptor concentration of the intrinsic layer can be reduced and the device performance can be improved by optimizing the process to suppress the unintentional doping.

REFERENCE

[1] Sang L, Liao M. A comprehensive Review of Semiconductor Ultraviolet Photodetectors: From Thin Film to one-dimensioanl nanostructures. Sensors, 2013, 13(8):10482-10518.

[2] Razeghi M, Rogalski A. Semiconductor ultraviolet detectors. Journal of Applied Physics, 1996, 79(10):7433-7473.

[3] Monroy E, Franck Omnès, Calle F. Wide-bandgap semiconductor ultraviolet detectors. Semiconductor Science & Technology, 2003, 18(4):R33.

[4] Liao MY, Sang LW, Teraji T, et al. Comprehensive investigation of single crystal diamond deep-ultraviolet detectors. Jpn. J. Appl. Phys. 2012, 51, 090115:1-090115:7.

[5] Khan MA, Kuznia JFUN, Olson DFUT, et al. High-responsivity photoconductive ultraviolet sensors based on insulating single-crystal GaN epilayer. Applied Physics Letters, 1992, 60(23):2917-2919.

[6] Flannery LB, Harrison I, Lacklison DE, et al. Fabrication and characterisation of p-type GaN metal-semiconductor-metal ultraviolet photoconductors grown by MBE. Materials Science & Engineering B, 1997, 50(1-3):307-310.

[7] Huang ZC, Mott DB, Shu PK, et al. Improvement of metal-semiconductor-metal GaN photoconductors. Journal of Electronic Materials, 1997, 26(3):330-333.

[8] Liu HY, Hsu WC, Chou BY, et al. Fabrication AlGaN/GaN MIS UV Photodetector by H2O2 Oxidation. IEEE Photonics Technology Letters, 2014, 27(1):101-104.

[9] Monroy E, Muñoz E, Sánchez FJ, et al. High-performance GaN p-n junction photodetectors for solar ultraviolet applications. Semiconductor Science & Technology, 1998, 13(9):1042.

[10] Elbar M, Alshehri B, Tobbeche S, et al. Design and Simulation of InGaN/GaN p-i-n Photodiodes. Physica Status Solidi, 2018, 215(9):1700521.

[11] Ravikiran L, Radhakrishnan K, Dharmarasu N, et al. GaN Schottky Metal Semiconductor Metal UV Photodetectors on Si(111) grown by Ammonia-MBE. IEEE Sensors Journal, 2016, PP(99):1-1.

[12] Li J, Fan ZY, Dahal R, et al. 200 nm deep ultraviolet photodetectors based on AlN. Applied Physics Letters, 2006, 89(21):3365-6.

[13] Casady JB, Johnson RW. Status of silicon carbide (SiC) as a wide-bandgap semiconductor for high-temperature applications: A review. Solid-State Electronics, 1996, 39(10): 1409-1422.

[14] Anikin MM, Andreev AN, Pyatko SN, et al. UV photodetectors in 6H-SiC. Sensors and Actuators A Physical, 1992, 33(1-2):91-93.

[15] Yang WF, Zhang F, Liu ZG, et al. High responsivity 4H-SiC based metal semiconductor metal ultraviolet photodetectors. Science in China Series G (Physics, Mechanics and Astronomy), 2008, 51(11):1616-1620.

[16] Edmond J, Kong H, Suvorov A, et al. 6H-Silicon Carbide Light Emitting Diodes and UV Photodiodes. physica status solidi (a), 1997, 162(1):11.

[17] Stéphane B, Lazar M, Ottaviani L, et al. 4H-silicon carbide thin junction based ultraviolet photodetectors. Thin Solid Films, 2012, 522(10):17-19.

[18] Bai X, Guo X, Mcintosh, et al. High Detection Sensitivity of Ultraviolet 4H-SiC Avalanche Photodiodes. IEEE Journal of Quantum Electronics, 2007, 43(12):1159-1162.

[19] Wang Z, Safdar M, Jiang C, et al. High-performance UV-visible-NIR broad spectral photodetectors based on one-dimensional In_2Te_3 nanostructures. Nano Letters, 2012, 12(9):4715.

[20] Zhang D, Liu C, Yin B, et al. Organics filled one-dimensional TiO_2 nanowires array ultraviolet detector with enhanced photo-conductivity and dark-resistivity. Nanoscale, 2017, 9(26).

[21] Tian W, Lu H, Li L. Nanoscale ultraviolet photodetectors based on onedimensional metal oxide nanostructures. Nano Research, 2015, 8(2):382-405.

[22] Kind H, Yan H, Messer B, et al. Nanowire Ultraviolet Photodetectors and Optical Switches. 2002, 14(2):158-160.

[23] Son MS, Im SI, Park YS, et al. Ultraviolet photodetector based on single GaN nanorod p-n Junctions. Mater. Sci. Eng. C 2006, 26, 886–888.

[24] Du J, Xing J, Ge C, et al. Highly sensitive and ultrafast deep UV photodetector based on a β-Ga_2O_3 nanowire network grown by CVD. Journal of Physics D Applied Physics, 2016, 49(42).

[25] Adib M, Eckstein R, Hernandez-Sosa G, et al. SnO_2 Nanowire Based Aerosol Jet Printed Electronic Nose as Fire Detector. IEEE Sensors Journal, 2017, PP(99):1-1.

[26] Chinh ND, Quang ND, Lee H, et al. NO gas sensing kinetics at room temperature under

UV light irradiation of In2O3 nanostructures. Sci Rep, 2016, 6:35066.

[27] Yan C, Singh N, Lee PS. Wide-bandgap Zn_2GeO_4 nanowire networks as efficient ultraviolet photodetectors with fast response and recovery time. Applied Physics Letters, 2010, 96(5):158.

[28] Liu Q, Zhou Y, Ma Y, et al. ChemInform Abstract: Synthesis of Highly Crystalline $In_2Ge_2O_7$(En) Hybrid Sub-Nanowires with Ultraviolet Photoluminescence Emissions and Their Selective Photocatalytic Reduction of CO_2 into Renewable Fuel. Cheminform, 2012, 2(8):3247-3250.

[29] Binari SC, Marchywka M, Koolbeck DA, et al. Diamond metal-semiconductor-metal ultraviolet photodetectors. Diamond & Related Materials, 1993, 2(5-7):1020-1023.

[30] Pace E, Di Benedetto R, Scuderi S. Fast stable visible-blind and highly sensitive CVD diamond UV photodetectors for laboratory and space applications. Diamond and Related Materials, 2000, 9(3-6):987-993.

[31] Wang WL, Liao KJ, Cai CZ, et al. Ultraviolet electroluminescence at room temperature from a pn junction of heteroepitaxial diamond film by CVD. Diamond and Related Materials, 2003, 12(8):1385-1388.

[32] Thaiyotin L, Ratanaudompisut E, Phetchakul T, et al. UV photodetector from Schottky diode diamond film. Diamond & Related Materials, 2002, 11(3):442-445.

[33] Rossi MC, Spaziani F, Conte G, et al. Metal/Diamond/Vacuum-type photodetectors in the ultraviolet band. Diamond and Related Materials, 2005, 14(3-7):552-555.

[34] Salvatori S, Scala AD, M.C Rossi, et al. Optimised contact-structures for metal diamond metal UV-detectors. Diamond & Related Materials, 2002, 11(3):458-462.

[35] Mckeag RD, Chan SSM, Jackman RB. Polycrystalline diamond photoconductive device with high UV-visible discrimination. Applied Physics Letters, 1995, 67(15):2117-2119.

[36] Yao K, Yang C, Zang X, et al. Carbon SP^2-SP^3 technology: Graphene-on-diamond thin film UV detector[C]. IEEE International Conference on Micro Electro Mechanical Systems. IEEE, 2014.

[37] Iwakaji, Kanasugi, Maida. Characterization of diamond ultraviolet detectors fabricated with high-quality single-crystalline chemical vapor deposition films. Applied Physics Letters, 2009, 94(22):S51.

[38] Salvatori S, Pace E, Rossi MC, et al. Photoelectrical characteristics of diamond UV detectors: Dependence on device design and film quality. Diamond and Related

Materials, 1997, 6(2-4):361-366.

[39] Benmoussa A, Schühle U, Haenen K, et al. PIN diamond detector development for LYRA, the solar VUV radiometer on board PROBA II. Physica Status Solidi, 2010, 201(11):2536-2541.

[40] Liao M, Koide Y. High-performance metal-semiconductor-metal deep-ultraviolet photodetectors based on homoepitaxial diamond thin film. Applied Physics Letters, 2006, 89(11):113509-113509-3.

[41] Teraji T, Yoshizaki S, Wada H, et al. Highly sensitive UV photodetectors fabricated using high-quality single-crystalline CVD diamond films. Diamond and Related Materials, 2004, 13(4-8):858-862.

[42] Liao M, Wang X, Teraji T, et al. Light intensity dependence of photocurrent gain in single-crystal diamond detectors. Physical Review B, 2010, 81(3):033304.

[43] Doherty MW, Wrachtrup J, Manson NB, et al. The nitrogen-vacancy colour centre in diamond. Physics Reports, 2013, 528(1):1-45.

[44] Direct determination of the barrier height of Ti-based ohmic contact on p-type diamond (001). Diamond and Related Materials, 2015, 60:117-122.

[45] Maier F, Ristein J, Ley L. Electron affinity of plasma-hydrogenated and chemically oxidized diamond (100) surfaces. Physical Review B, 2001, 64(16):165411.

[46] Sugeta T, Urisu T. WP-B2 High-Gain Metal-Semiconductor-Metal Photodetectors for High-Speed Optoelectronic Circuits. IEEE Transactions on Electron Devices, 1979, 26(11):1855-1856.

[47] Zhao B, Wang F, Chen H, et al. Solar-Blind Avalanche Photodetector Based On Single ZnO-Ga_2O_3, Core-Shell Microwire. Nano Letters, 2015, 15(6):3988.

[48] Williams OA, Jackman RB. High growth rate MWPECVD of single crystal diamond. Diamond and Related Materials, 2004, 13(4-8):557-560.

[49] Chayahara A, Mokuno Y, Horino Y, et al. The effect of nitrogen addition during high-rate homoepitaxial growth of diamond by microwave plasma CVD. Diamond and Related Materials, 2004, 13(11-12):1954-1958.

[50] Caylar B, Pomorski M, Bergonzo P. Laser-processed three dimensional graphitic electrodes for diamond radiation detectors. Applied Physics Letters, 2013, 103(4):S105-309.

[51] Forneris J, Giudice AL, Olivero P, et al. A 3-dimensional interdigitated electrode geometry for the enhancement of charge collection efficiency in diamond detectors.

Epl, 2014, 108(1):18001.

[52] Kuzmany H, Hulman M, Pfeiffer R, et al. RAMAN SCATTERING OF CARBON NANOTUBES[M]. Carbon Nanotubes. 2006.

[53] Huang Y, Wu J, Hwang KC. Thickness of graphene and single-wall carbon nanotubes. Physical Review B, 2016, 74(24):4070-4079.

[54] Takagi D, Homma Y, Hibino H, et al. Single-walled carbon nanotube growth from highly activated metal nanoparticles. Nano Letters, 2006, 6(12):2642.

[55] Yoshida H, Takeda S, Uchiyama T, et al. Atomic-scale in-situ observation of carbon nanotube growth from solid state iron carbide nanoparticles. Nano Letters, 2008, 8(7):2082.

[56] Chen X, Wang YX. An Experimental Analysis of Fast Annealed Ti/AlN Interface. Vacuum Science and Technology (CHINA), 1997(3):160-166.

[57] Boukherroub R, Wallart X, Szunerits S, et al. Photochemical oxidation of hydrogenated boron-doped diamond surfaces. Electrochemistry Communications, 2005, 7(9):937-940.

[58] Ohta R, Saito N, Inoue Y, et al. Organosilane self-assembled monolayers directly linked to the diamond surfaces. Journal of Vacuum Science & Technology A Vacuum Surfaces & Films, 2004, 22(5):2005-2009.

[59] Liao X, Ran J, Gou L. Response of radiation dosimeters based on in situ oxygen plasma post-treated CVD-diamond thin films to X-ray. Journal of Materials Science, 2010, 45(10):2780-2787.

[60] Tuinstra F, Koenig JL. Raman Spectrum of Graphite. Journal of Chemical Physics, 1970, 53(3):1126-1130.

[61] Hirai T, Compan J, Niwase K, et al. Laser Raman microprobe analysis of graphite exposed to edge plasma in the TEXTOR tokamak. Journal of Nuclear Materials, 2008, 373(1-3):119-122.

[62] Castiglioni C, Mapelli C, Negri F, et al. Origin of the D line in the Raman spectrum of graphite: A study based on Raman frequencies and intensities of polycyclic aromatic hydrocarbon molecules. Journal of Chemical Physics, 2001, 114(2):963-974.

[63] Rodrigues AM. Extraction of Schottky diode parameters from current-voltage data for a chemical-vapor-deposited diamond/silicon structure over a wide temperature range. Journal of Applied Physics, 2008, 103(8):251.

[64] Cheung SK, Cheung NW. Extraction of Schottky diode parameters from forward

current-voltage characteristics. Applied Physics Letters, 1986, 49(2):85-0.

[65] Traoré, A, Muret P, Fiori A, et al. Zr/oxidized diamond interface for high power Schottky diodes. Applied Physics Letters, 2014, 104(5):052105.

[66] Kobayashi T, Hou GR, Maki T, et al. Depth Profile Measurement of Activated Boron-Concentration in Diamond Thin Films Utilizing Schottky Diode C-V Curves. Japanese Journal of Applied Physics, 1993, 32(11):L1588-L1591.

[67] Javadi M, Torbatiyan H, Abdi Y. Ultra-low intensity UV detection using partitioned mesoporous TiO_2. Applied Physics Letters, 2017, 111(6):063113.

[68] Huang SH , Li X, Lin Y, et al. Study of ultrafast process in semiconductor. Journal Infrared Millimeter & Waves, 2005, 24(3):179-181.

[69] Kruglyak VV, Hicken RJ, Ali M, et al. Measurement of hot electron momentum relaxation times in metals by femtosecond ellipsometry. Phys.rev.b, 2005, 71(23):233104.

[70] Gabrysch M, Majdi S, Twitchen DJ, et al. Electron and hole drift velocity in chemical vapor deposition diamond. Journal of Applied Physics, 2011, 109(6):073704.

[71] Isberg J, Hammersberg J, Bernhoff H, et al. Charge collection distance measurements in single and polycrystalline CVD diamond. Diamond and Related Materials, 2004, 13(4-8):872-875.

[72] Sajedi Alvar M, Javadi M, Abdi Y, et al. Enhancing the electron lifetime and diffusion coefficient in dye-sensitized solar cells by patterning the layer of TiO_2 nanoparticles. Journal of Applied Physics, 2016, 119(11):114302.

[73] Hong-Fei QI , Liu DB . Effect of Growth Technology of TiO_2 Film on Photoelectronic Properties of TiO_2 UV Detector. Journal of Aeronautical Materials, 2011, 31(5):47-50(4).

[74] Huang H, Hu H, Xie Y, et al. Low-Dark-Current MSM UV Photodetectors With Pt Schottky Contacts. Electron Device Letters IEEE, 2011, 32(4):530-532.

[75] Huang H, Xie Y, Zhang Z, et al. Growth and fabrication of sputtered TiO_2 based ultraviolet detectors. Applied Surface Science, 2014, 293:248-254.

[76] Xue-Ao Z, Hao WU, Hai-Liang Z, et al. Analysis on Spectrum Response of Silicon Photoelectric Diode. Physical Experiment of College, 2011.

[77] Qiang HG, Gang Z, Dong LT, et al. The Dark Current Characteristics of InGaAs PIN Photodetectors. Semiconductor Optoelectronics, 2004, 25(5):341-340.

[78] Tsao BH, Carr SF, Weimer JA. [AIP Proceedings of the 12th symposium on space

nuclear power and propulsion: Conference on alternative power from space; Conference on accelerator-driven transmutation technologies and applications - Albuquerque, New Mexico (USA) (8-12 Jan 1995)] AIP Conference Proceedings - Ultra-thin TiO_2 dielectric film for high capacitance capacitor. 1995, 324:117-122.

[79] Chakraborty S, Bera M , Bhattacharya S, et al. Current conduction mechanism in TiO_2 gate dielectrics. Microelectronic Engineering, 2005, 81(2):188-193.

[80] Umeda T, Mochizuki Y, Okonogi K, et al. Defects related to DRAM leakage current studied by electrically detected magnetic resonance. Physica B Condensed Matter, 2001, 308 (308): 1169-1172.

[81] Hiraiwa A, Kawarada H. Figure of merit of diamond power devices based on accurately estimated impact ionization processes. Journal of Applied Physics, 2013, 114(3):034506 - 034506-9.

[82] Umezawa H, Nagase M, Kato Y, et al. High temperature application of diamond power device. Diamond and Related Materials, 2012, 24:201-205.

[83] Umezawa H, Saito T, Tokuda N, et al. Leakage current analysis of diamond Schottky barrier diode. Applied Physics Letters, 2007, 90(7):073506.

[84] Ikeda K, Umezawa H, Shikata S. Edge termination techniques for p-type diamond Schottky barrier diodes. Diamond and Related Materials, 2008, 17(4-5):809-812.

[85] Syamsul M, Oi N, Okubo S, et al. Heteroepitaxial Diamond Field-Effect Transistor for High Voltage Applications. IEEE Electron Device Letters, 2018, PP(99):1-1.

[86] Nobutaka O, Masafumi I, Satoshi O, et al. Vertical-type two-dimensional hole gas diamond metal oxide semiconductor field-effect transistors. Scientific Reports, 2018, 8(1):10660.

[87] Makino T, Yoshino K, Sakai N, et al. Enhancement in emission efficiency of diamond deep-ultraviolet light emitting diode. Applied Physics Letters, 2011, 99(6):1274.

[88] Takeucni D, Koizumi S, Makino T, et al. A 10kV vacuum switch with negative electron affinity of diamond p-i-n electron emitter[C]. Electron Devices Meeting. IEEE, 2012.

[89] Suzuki M, Sakai T, Makino T, et al. Electrical characterization of diamond PiN diodes for high voltage applications. Physica Status Solidi (a), 2013, 210(10):5.

[90] Kato H, Yamasaki S, Okushi H. n-type doping of (001)-oriented single-crystalline diamond by phosphorus. Applied Physics Letters, 2005, 86(22):1899.

[91] Pinault-Thaury MA, Tillocher T, Habka N, et al. n-Type CVD diamond: Epitaxy and doping. Materials Science & Engineering B, 2011, 176(17):1401-1408.

[92] Butler JE, Mankelevich YA, Cheesman A, et al. Understanding the chemical vapor deposition of diamond: recent progress. Journal of Physics Condensed Matter, 2009, 21(36):364201.

[93] Nakai T, Maida O, Ito T. Characterization of phosphorus-doped homoepitaxial (1 0 0) diamond films grown using high-power-density MWPCVD method with a conventional quartz-tube chamber. Applied Surface Science, 2008, 254(19):6281-6284.

[94] Kato H, Makino T, Ogura M, et al. Maskless Selective Growth Method for p-n Junction Applications on (001)-Oriented Diamond. Japanese Journal of Applied Physics, 2012, 51(9):0118.

PUBLICATION

Article Paper:

(1) **Zhangcheng Liu**, Dan Zhao, Jin-Ping Ao, Wei Wanga, Xiaohui Chang, Yanfeng Wang, Jiao Fu and Hong-Xing Wang, Enhanced ultraviolet photoresponse of diamond photodetector using patterned diamond film and two-step growth process, Materials Science in Semiconductor Processing, 89, 110-115, January, 2019.

(2) **Zhangcheng Liu**, Dan Zhao, Jin-Ping Ao, Wei Wang, Xiaohui Chang, Yanfeng Wang, Jiao Fu, and Hong-Xing Wang, Responsivity improvement of Ti-diamond-Ti structure UV photodetector through photocurrent gain, Optics Express, 26, 17092-17098, June, 2018.

(3) **Zhangcheng Liu**, Jin-Ping Ao, Fengnan Li, Wei Wang, Jingjing Wang, Jingwen Zhang, and Hong-Xing Wang, Photoelectrical characteristics of ultra thin TiO2/diamond photodetector, Materials Letters, 188, 52-54, February, 2017.

(4) **Zhangcheng Liu**, Jin-Ping Ao, Fengnan Li, Wei Wang, Jingjing Wang, Jingwen Zhang, and Hong-Xing Wang, Fabrication of three dimensional diamond ultraviolet photodetector through down-top method, Applied Physics Letters, 109, 153507, October, 2016.

Conference Paper:

(1) **Zhangcheng Liu**, Dan Zhao, Jin-Ping Ao, Xiaohui Chang, Yanfeng Wang, Jiao Fu, Minghui Zhang and Hong-Xing Wang, Responsivity Improvement of Diamond UV Photodetector with Novel Device Design, NDNC 2018 Conference.

(2) **Zhangcheng Liu**, Dan Zhao, Jin-Ping Ao, Wei Wang and Hongxing Wang, Structured TiO_2/Diamond Photodetector with Photon-induced Negative Photoconductive Phenomenon, SCDE 2018 Conference.

(3) **Zhangcheng Liu**, Dan Zhao, Tai Min, Jin-Ping Ao, and Hong-Xing Wang, Structure design for diamond UV photodetector—Three dimensional diamond UV detector and p-i-n photodiode, SCDE 2019 Conference.